
Theses and Dissertations

Fall 2018

Novel MR image recovery using patch-smoothness iterative shrinkage algorithm

Yasir Qasim Mohsin
University of Iowa

Follow this and additional works at: <https://ir.uiowa.edu/etd>

 Part of the [Electrical and Computer Engineering Commons](#)

Copyright © 2018 Yasir Qasim Mohsin

This dissertation is available at Iowa Research Online: <https://ir.uiowa.edu/etd/6538>

Recommended Citation

Mohsin, Yasir Qasim. "Novel MR image recovery using patch-smoothness iterative shrinkage algorithm." PhD (Doctor of Philosophy) thesis, University of Iowa, 2018.
<https://doi.org/10.17077/etd.c1na-99c6>

Follow this and additional works at: <https://ir.uiowa.edu/etd>

 Part of the [Electrical and Computer Engineering Commons](#)

NOVEL MR IMAGE RECOVERY USING PATCH-SMOOTHNESS ITERATIVE
SHRINKAGE ALGORITHM

by

Yasir Qasim Mohsin

A thesis submitted in partial fulfillment of the
requirements for the Doctor of Philosophy degree
in Electrical and Computer Engineering
in the Graduate College of
The University of Iowa

December 2018

Thesis Supervisor: Professor Mathews Jacob

Copyright by
YASIR QASIM MOHSIN
2018
All Rights Reserved

Graduate College
The University of Iowa
Iowa City, Iowa

CERTIFICATE OF APPROVAL

PH.D. THESIS

This is to certify that the Ph.D. thesis of

Yasir Qasim Mohsin

has been approved by the Examining Committee for the thesis requirement for the Doctor of Philosophy degree in Electrical and Computer Engineering at the December 2018 graduation.

Thesis Committee: _____

Mathews Jacob, Thesis Supervisor

Vincent Magnotta

Xiaodong Wu

Weiyu Xu

Daniel Thedens

Dedicated To The Late Senator,

Fulbright

*May You Rest In Peace & May
Your Soul Be Bound For Heaven*

ACKNOWLEDGEMENTS

A lucky person will encounter, sometimes during his life period, one great teacher. A teacher of this sort is measured not only by the lessons delivered but also by the profound influence he has on the philosophy and therefore the life of his student. I have been one of those lucky people who encountered such a great teacher. Mathews was not only a professor, a teacher or thesis advisor but also a friend and a big brother whom you can count on discussing your life ups and downs. Without his guidance and direction, this thesis could not have been written, and I would have not whatever claimed the graduate assistantship I have today. I would like to express my sincere gratitude to him for his contribution and support throughout my Ph.D. study. He has always given me constructive and effective guidance in my research and inspired me with brilliant ideas. I greatly appreciate the efforts he put on me and I highly respect his profound knowledge and great passion for research.

I also appreciate Professors Weiyu Xu, Vincent Magnotta, Xiaodong Wu and Dan Thedens for being my defense committee and their constructive feedback to improve the thesis. Special thanks go to all my labmates in the Computational Biomedical Imaging Group (CBIG): Dr. Sajan Goud, Dr. Abdul Haseeb Ahmed, Dr. Hemant Aggarwal, Dr. Chen Cui, Dr. Merry Mani, Dr. Greg Ongie, Dr. Zhili Yang, Dr. Sampada Bhave, Dr. Ipshita Bhattacharya, Dr. Arvind Balachandrasekaran, Dr. Sunrita Poddar, Dr. Sampurna Biswas. Thanks for all the great ideas and advice from them. I cherish the memory of academic discussion and wonderful work life with them.

Last but not least, I would like to thank my parents and family members. Without their love, support, prayers, and encouragement, I could not get through this period. Again, millions of thanks to all Iraqi family and my close friends here in Iowa City who helped me in the past few years to be part of the great Hawkeye family.

ABSTRACT

Obtaining high spatial or spatiotemporal resolution along with good slice coverage is challenging in dynamic magnetic resonance imaging, MRI, due to the slow nature of the acquisition process. In recent years, there has been a rapid growth of MRI techniques that allow faster scan speed by exploiting spatial or spatiotemporal redundancy of the images. These techniques can improve the performance of imaging significantly across multiple clinical applications, including cardiac functional examinations, perfusion imaging, blood flow assessment, contrast-enhanced angiography, functional MRI, and interventional imaging, among others.

The ultimate goal of this thesis is to develop novel algorithms to reconstruct heavily undersampled sparse imaging. The designed schemes aim to achieve a shorter scan duration, higher spatial resolution, increased temporal resolution, signal-to-noise ratio and coverage in multidimensional multichannel MRI. In addition to improving patients comfort and compliance while imaging under the MRI device, the newly developed schemes will allow patients with arrhythmia problems, pediatric and obese subjects to breath freely without the need for any breath-hold scans. Shortening examination periods also reduces patient's stress, lowers the entire visit to the clinic and finally decreases the associated economic costs. Rapid imaging acquisitions will also allow for efficient extraction of quantitative information needed for the patients' diagnosis eg. tumor characterization and veins blockages through myocardial perfusion MRI. Current applications of interests include real-time CINE MRI and contrast changing perfusion MRI.

PUBLIC ABSTRACT

Magnetic resonance imaging enables excellent visualization of both anatomical structure and physiological function. Although it is used to diagnose numerous medical conditions, current technology has several practical limitations, one of which is slow imaging speed. Imaging speed in MRI is limited by physical and physiological constraints associated with rapidly switching magnetically held gradients. Lack of speed poses particular challenges for applications in dynamic cardiac MRI.

To reduce artifacts related to respiratory motion, most routine cardiac MRI techniques acquire images during a patient's breath-holds. The patient's ability to sustain breath-holds along with imaging speed determine the duration of the examination, which in turn, determines the spatial and temporal resolution of the images. However, since many patients are unable to sustain breath-holds, the acquisition process must be accelerated to reduce scan time.

In this thesis, we apply iterative algorithms of patch-smoothness regularization to speed up medical imaging acquisitions. We employ our frameworks to solve problems arising in various MRI applications. The utility of the proposed schemes is demonstrated in the context of in-vivo static MR imaging, breath-held and free-breathing cardiac CINE MRI with multichannel acquisitions as well as simulated phantoms, myocardial perfusion MRI, gated and ungated acquisitions using both retrospective and prospective experiments. The prospective datasets are challenging cases since they are acquired in the ungated mode, accelerated by a high undersampling factor and considerable cardiorespiratory motion is present due to the free-breathing scan. We compare the algorithms against state-of-the-art finite difference, motion-compensated and motion-resolved methods.

TABLE OF CONTENTS

| | |
|--|------|
| LIST OF TABLES | viii |
| LIST OF FIGURES | ix |
| CHAPTER | |
| 1 INTRODUCTION | 1 |
| 1.1 BACKGROUND | 1 |
| 1.2 COMPRESSED SENSING | 2 |
| 1.3 THESIS CONTRIBUTION | 2 |
| 1.3.1 2-D IMAGE RECONSTRUCTION | 3 |
| 1.3.2 MOTION-COMPENSATED DYNAMIC IMAGE RECONSTRUCTION | 4 |
| 1.3.3 MOTION-RESOLVED DYNAMIC IMAGE RECONSTRUCTION | 6 |
| 1.4 ORGANIZATION | 8 |
| 2 FAST NOVEL PATCH-BASED ITERATIVE SHRINKAGE SCHEME | 11 |
| 2.1 ABSTRACT | 11 |
| 2.2 METHOD | 11 |
| 2.2.1 Problem Formulation | 11 |
| 2.2.2 Unified Non-Local Regularization | 12 |
| 2.2.3 Solution Using an Iterative Reweighted Algorithm | 13 |
| 2.3 PROPOSED ALGORITHM | 14 |
| 2.3.1 Majorization of the Penalty Term | 14 |
| 2.3.2 The \mathbf{s} Sub-Problem: solve for $\mathbf{s}_{\mathbf{x},\mathbf{q}}$, assuming \mathbf{f} fixed | 15 |
| 2.3.3 The f Sub-Problem: solve for f , assuming $\mathbf{s}_{\mathbf{x},\mathbf{q}}$ fixed | 15 |
| 2.3.4 Determination of Shrinkage Rules | 17 |
| 2.4 IMPLEMENTATION | 21 |
| 2.4.1 Analytical Solution of equation (2.11) in the Fourier Domain | 22 |
| 2.4.2 Efficient Evaluation of Shrinkage Weights | 23 |
| 2.4.3 Continuation Strategy to Improve Convergence | 24 |
| 2.5 RESULTS | 26 |
| 2.5.1 Convergence Rate | 26 |
| 2.5.2 Impact of the Distance Metric | 27 |
| 2.5.3 Comparisons With State-of-the-Art Algorithms | 28 |
| 2.5.4 Performance With Noise | 30 |
| 2.5.5 Validation using non-Cartesian MRI data | 32 |
| 2.6 DISCUSSION AND CONCLUSION | 35 |
| 2.7 Appendix A: Simplification of Eq (2.11) | 37 |
| 2.8 Appendix B: Shrinkage rules for useful non-local distance functions | 39 |

| | | |
|-------|---|----|
| 3 | ACCELERATED MRI USING PATCH REGULARIZATION FOR IMPLICIT MOTION COMPENSATION | 41 |
| 3.1 | ABSTRACT | 41 |
| 3.2 | THEORY | 41 |
| 3.2.1 | Dynamic MRI: Model Of The Acquisition Scheme | 41 |
| 3.2.2 | Implicit Motion Compensation Using Patch Regularization | 42 |
| 3.2.3 | Iterative Patch Shrinkage Algorithm | 43 |
| 3.3 | METHODS | 47 |
| 3.3.1 | Experiments Involving Cardiac CINE MRI | 47 |
| 3.3.2 | Experiments Involving Myocardial Perfusion Imaging | 48 |
| 3.3.3 | Implementation Details | 49 |
| 3.3.4 | Selection of Parameters | 50 |
| 3.4 | RESULTS | 51 |
| 3.4.1 | Results of Cardiac CINE Datasets | 51 |
| 3.4.2 | Results of Myocardial Perfusion MRI | 51 |
| 3.5 | DISCUSSION AND CONCLUSION | 53 |
| 4 | FREE-BREATHING & UNGATED CARDIAC MRI USING ITERATIVE STORM (I-STORM) | 58 |
| 4.1 | ABSTRACT | 58 |
| 4.2 | METHOD | 58 |
| 4.2.1 | SToRM reconstruction | 58 |
| 4.2.2 | Calibration-free i-SToRM | 59 |
| 4.2.3 | Relationship to SToRM | 61 |
| 4.2.4 | i-STORM with patches | 62 |
| 4.2.5 | Two step iterative algorithm using MM | 63 |
| 4.2.6 | Datasets and sampling pattern | 65 |
| 4.2.7 | Metrics used for quantitative comparison | 66 |
| 4.2.8 | Implementation | 67 |
| 4.3 | RESULTS | 68 |
| 4.4 | DISCUSSION AND CONCLUSION | 71 |
| 5 | SUMMARY & FUTURE DIRECTIONS | 77 |
| 5.1 | SUMMARY | 77 |
| 5.2 | FUTURE DIRECTIONS | 78 |
| 6 | REFERENCES | 80 |

LIST OF TABLES

Table

| | | |
|-----|--|----|
| 2.1 | (SNR in dB) Impact of the distance metric on the reconstructions. We compare the reconstructions obtained using the non-local shrinkage algorithm using ℓ_1 , H_1 , NLTV, thresholded ℓ_1 and thresholded $\ell_p; p = 0.5$ metrics. All the metrics, except the convex ℓ_1 scheme are saturating priors. We observe that saturation is key to good performance of non-local algorithms. Among the different metrics, the thresholded ℓ_p penalty is observed to provide the best results in all the examples. | 28 |
| 2.2 | (SNR in dB) Quantitative comparison of the proposed iterative non-local shrinkage (NLS) algorithm using the saturating $\ell_p; p = 0.5$ penalty with dictionary learning MRI (DLMRI) [1] and local total variation regularization (TV) schemes in the absence of noise. We considered five-fold random undersampling. | 29 |
| 2.3 | Quantitative comparison of the algorithms in the presence of noise. The top part shows the SNR of the reconstructions obtained from 3 fold Cartesian undersampled data. The bottom part shows the SNR of the reconstructions from radial undersampled data with 70 spokes. Both experiments are contaminated by zero mean complex Gaussian noise such that the SNR of the noisy images are reported in the table. The quantitative results show that the proposed iterative NLS scheme provides consistently better reconstructions for the above cases. | 34 |

LIST OF FIGURES

Figure

- 1.1 Illustration of the proposed PRICE and iSTORM schemes. The time profile in the top row is drawn along myocardium such that the cardiorespiratory motions are shown. The chosen frames are depicted in the time profiles with their perspective colors. In the case of PRICE, subfigure (b), the metric penalizes the differences between each patch and other patches in its cube-shaped neighborhood in both spatiotemporal directions. The green squares indicate the location of the patch in the current frame and the ones with the highest similarity in the neighboring frames shown in the blue boxes. The dashed red box represents the neighborhood where the patches move within. In iSTORM, the metric is used to calculate the weights between the frames that have the same cardiac and respiratory phases. PRICE and iSTORM alternate between inter-patch differences estimation and image update step, which involves a computationally efficient conjugate gradients algorithm. The NLS scheme is a simple version of those schemes aimed to recover the static images analytically. 10
- 2.1 Distances functions $\phi(t)$ that are relevant in non-local regularization (first row) and the associated shrinkage rules $t \cdot \nu(|t|)$ (second row); see Appendix B in [2] for the corresponding formulas that relies on a convex hull approximation of the original penalty. Here we illustrate the shrinkage rules in 1-D for the parameter choices $\beta = 2$, $p = 0.5$, $T = 1$, and $\sigma = 0.5$. The approach introduced in the research enables evaluating the shrinkage rules for a much larger class of penalties, generalizing the results in [3] for ℓ_p penalties shown in the first column. 16
- 2.2 Approximation of the potential function: (a) shows the original potential function $\varphi(t)$ in 1-D, which is the truncated ℓ_p ; $p = 0.5$ penalty, $T = 1$. (b) indicates the corresponding $r(t) = t^2/2 - \frac{1}{\beta}\varphi(t)$ function with $\beta = 2$, shown in black. Note that this function is non-convex. Hence, we approximate this function by $\hat{r}(t)$ shown in blue, which is the best convex approximation of $r(t)$. The corresponding modified potential function is shown in blue in (c). (d) indicates the approximations for different values of β . Note that the approximations converge uniformly to φ . (e) shows the corresponding shrinkage rules. The potential functions and shrinkage rules for different penalties are shown in Fig. 2.1. 19

- 2.3 Comparison of the convergence rate of the iterative reweighted (IRW) algorithm and the proposed iterative non-local shrinkage (NLS) algorithm. The plots indicate the evolution of the cost function in [equation (2.2)] as functions of (a) the CPU time and (b) number of inner iterations in NLS and CG steps in IRW. Both NLS and IRW algorithms converged in around 225 inner iterations. However, the IRW scheme needed around 9 CG steps/inner iteration on average, requiring a total of 2200 (see Algorithms IV.1 and IV.2). Since each inner iteration in NLS is considerably faster than the corresponding one in [4], we obtain a speedup of approximately ten fold. 29
- 2.4 Comparison of the algorithms in the absence of noise. We consider the recovery of a 128×128 MR brain image from 5 fold undersampled Fourier samples, acquired using a random sampling pattern shown in (e) using non-local shrinkage scheme (NLS), DLMRI and local TV. The reconstructions are shown in (b)-(d). The corresponding error images, scaled by a factor of 5 for better visualization, are shown in the bottom row. The reconstructions show that the NLS scheme is capable of better preserving the edges and details, resulting in less blurred reconstructions. Note that this example was used as an illustration; the proposed 2-D under sampling pattern on the dataset acquired using a 3-D sequence is not very realistic. We also used a high acceleration factor to demonstrate differences between the methods; thus the resulting images may not be of diagnostic quality. 30
- 2.5 Comparison of the algorithms in the presence of noise. We consider the recovery of a 512×512 MR head complex image from three-fold undersampled k-space data, acquired using a Cartesian sampling pattern contaminated by zero mean complex Gaussian such that the SNR value after adding the noise is 25.0 dB. The top row shows the original and reconstructed images using non-local shrinkage scheme (NLS), DLMRI and local TV. The reconstructions are shown in (b)-(d). The corresponding error images as well as the sampling pattern are shown in the bottom row. This is a challenging case due to the high 1-D undersampling factors and noise. We observe that the NLS scheme provides better reconstructions with minimal aliasing artifacts. Note that this example was used as an illustration; the proposed 2-D under sampling pattern on the dataset acquired using a 3-D spin-echo sequence is not very realistic. Note that we used a high acceleration factor to demonstrate differences between the methods. The resulting images may not be of diagnostic quality. 31
- 2.6 Comparison of three different MR images using NLS scheme in the presence of noise. The Fourier samples are contaminated by zero mean complex Gaussian noise such that the SNR of the data corresponding to the head, brain2 and calf images are 32.3, 24.7 and 27.6 dB, respectively. The top row shows the recovery from 2 fold acceleration using the Cartesian sampling pattern, while the middle one shows the recovery from 100 radial spokes (≈ 3 fold acceleration). The bottom row shows the recovery from 3 fold acceleration using random pattern. We observe that the NLS scheme is capable of preserving the key image details. 33

- 2.7 Comparison of MR brain images using NLS and TV algorithms from undersampled multichannel multi-shot spiral data. The fully sampled data was acquired using a multishot spiral sequence with 22 interleaves acquired using 12 channels. All the interleaves were used to recover the fully sampled datasets, while only 7 randomly chosen interleaves were used to recover the undersampled datasets. The retained interleaves are shown in the first column. We only used the data corresponding to four important coils for the recovery. The two rows corresponds to two slices in the acquisition. The recovery of the lower slice was considerably challenging due to field inhomogeneity losses and subtle physiological motion between interleaves; this explains the poor recovery of the datasets. The two rows show the spiral trajectory, original and reconstructed images. Both the proposed and TV regularized reconstructions are seen to have lower SNR, mainly due to decreased number of measurements. However, we observe that the proposed scheme provides sharper reconstructions. 36
- 3.1 (a) Illustration of the proposed PRICE scheme. The regularization term penalizes the differences between each patch and other patches in its cube shaped neighborhood. The green squares indicate the location of the patch in the current frame and the ones with the highest similarity in the neighboring frames. The dashed red box represents the neighborhood where the patches move within. The ability of the algorithm to exploit the similarity between corresponding patches enables it to provide implicit motion compensated recovery unlike the traditional ME-MC methods which explicitly do that. The distance metric used for the comparison is shown by the dotted black curve in (b). The metric heavily penalizes the distances between similar patches, while it saturates for large inter-patch distances. This saturating behavior enables the algorithm to minimize spatiotemporal blurring, resulting from averaging of dissimilar patches. The colored curves correspond to the different approximations of the distance metric, which enables fast algorithms. (c) The shrinkage rule for the inter-patch differences $t \cdot \nu(|t|)$ using ℓ_p . We rely on continuation schemes as shown in (b) and (c) starting with low values of β and gradually increase it to high values, when the approximation is more accurate. (d) The algorithm alternates between a simple shrinkage step to denoise inter-patch differences and image update step, which involves a computationally efficient conjugate gradients algorithm. . . . 44

- 3.2 Recovery of a retrospectively undersampled CINE dataset using PRICE (second row; b1-b2), explicit motion-compensated algorithms (third and fourth rows), k-t SLR and classical total variation regularization (fifth and sixth rows). The $256 \times 224 \times 16$ dynamic dataset, which is acquired using $\times 5$ coils, is retrospectively undersampled using Cartesian sampling pattern. The cropped cardiac images of the fully sampled data corresponding to peak diastole and systole cardiac phases are shown in (a1) and (a2). These images are cropped versions of the full frame shown in (a3). The sampling pattern for one frame is shown in (a4). The cropped reconstructed images are shown in the first two columns, while their error images scaled by a factor of 7 for better visualization are shown in the last two columns. The reconstructions using the PRICE algorithm is quite comparable to the DC-CS scheme, which explicitly compensates for the motion; the error images show that the errors associated with PRICE and DC-CS are more homogeneously distributed in the entire image, resulting in improved SER. By contrast, the errors with other methods (e.g. TV and MASTeR) are more concentrated in the edge regions, indicating edge blurring. The table shows a quantitative comparison of the entire methods using SER, HFEN and SSIM metrics; all computed on the region of interest as shown in (a3). 54
- 3.3 Recovery of a prospectively undersampled Cartesian CINE dataset using PRICE, DC-CS, k-t SLR and TV algorithms. The $128 \times 128 \times 20$ sized dataset is acquired using 12 coils and 16 Cartesian lines per phase. Two frames corresponding to peak diastole and systole cardiac phases are shown for each scheme along with their zoomed versions around the square box as shown in (b1). The sampling pattern varies from frame to frame; the sampling masks corresponding to two different frames are shown in (a2) and (a3). We observe that TV and k - t SLR reconstructions exhibit temporal blurring while DC-CS had some motion artifacts. PRICE is able to provide better reconstructions with less blurred myocardial borders and papillary muscles. 55
- 3.4 Evaluation of the ME-MC algorithms by retrospectively downsampling ungated & free-breathing myocardial perfusion MRI data. The images (a1-a4) correspond to frames in the time series with different cardiac/respiratory phases and different contrast due to bolus passage. These images are cropped from a $288 \times 108 \times 80$ dataset acquired with 6 coils; one of these images are shown in (a5). We undersampled the Cartesian sampled data along the phase encoding direction to obtain a three-fold acceleration. One of the sampling masks are shown in (a6). The reconstructions and corresponding residuals using PRICE (b1-b4) & (b5-b8), DC-CS (c1-c4)& (c5-c8), MASTeR (d1-d4)& (d5-d8), k-t SLR (e1-e4)& (e5-e8) and TV (f1-f4)& (f5-f8) are shown. The error images are scaled by a factor of three for better visualization. The extensive inter-frame motion and contrast variations due to bolus passage makes this dataset very challenging. We observe that the PRICE scheme provides reconstructions with lower spatial and temporal blurring, compared to the other algorithms. The table above shows a quantitative comparison of the entire methods using SER, HFEN and SSIM metrics computed on the region of interest shown in (a5). 56

3.5 Evaluation of the ME-MC algorithms by radially downsampling $256 \times 256 \times 67$ adenosine free-breathing stress myocardial perfusion MRI data acquired from a normal subject. Three frames of the reference data acquired using 72 spokes/frame are shown in (a1-a3). This data is undersampled by retaining a subset of 24 spokes; the sampling trajectory for one of the frames is shown in (a4). The recovered images and their corresponding residual images using PRICE (b1-b3) & (b4-b6), DC-CS (c1-c3) & (c4-c6), k-t SLR (d1-d3) & (d4-d6), and TV (e1-e3) & (e4-e6) are shown. The three frames correspond to peak right ventricular blood enhancement, a transition between the right ventricle and the left ventricle and peak left ventricular blood enhancement respectively. It is seen from the error images that the motion compensated methods (PRICE and DC-CS) provide reduced edge blurring and better preservation of fine features, including papillary muscles and around the myocardium wall as shown by the red arrows. 57

4.1 Illustration of the proposed i-SToRM scheme (b), in comparison with the SToRM scheme in (a). The regularization term in SToRM involves the sum of weighted ℓ_2 distances between images in the dataset, where the weights are estimated from navigators. By contrast, the regularization scheme in i-SToRM is the sum of unweighted robust distances between image sub-patches in the dataset. Specifically, the patches of size $N \times N$ indicated by the green neighborhood are compared with each other using the distance metric, which saturates with large distances. The center of the patches, specified by \mathbf{r}_k are chosen to span the entire image with a specified stride; the patches are overlapping in space to reduce blocky artifacts in the image and suppress noise. The main difference between these formulations is the distance metric. We use an alternating minimization to solve for the i-SToRM scheme, which alternates between the estimation of the manifold Laplacian and the images; this approach eliminates the need for the use of navigators and allows the extension of the SToRM scheme to exploit the manifold structure of local patches. When the size of the patches is the same as the size of the images, the first iteration of the i-SToRM scheme is equivalent to the SToRM setting. 60

4.2 Comparison of SToRM, PSF, TV +Wavelet, i-SToRM without patches, and i-SToRM with patches: We study the performance of these methods on a free-breathing ungated cardiac CINE setting, acquired in the axial 4-chamber view. The dataset was acquired using the navigated acquisition scheme used in [5], which consists of 4 navigator lines and 6 golden angle spokes per frame. The sampling trajectory for one of the sampling patterns is shown in sub-figure (a1) with colored lines indicating the navigators that are the same for all frames. The time profiles in the fourth column are drawn for all of the recovered frames, along with the line passing through the cardiac region shown in (b1). The time instance of the specific frames are depicted in the time profiles with the color of their bounding boxes. Three frames of each recon dataset are shown. The images are zoomed versions around the square box shown in (a3) while (a2) is the initial guess. Subfigures (b1-b3), (c1-c3) and (d1-d3) show the recovery using navigators-free schemes, patch-based i-SToRM, i-SToRM with patches and TV + Wavelet respectively; while (e1-e3) and (f1-f2) show the recovery using navigators-based schemes SToRM and PSF. The top five rows are recovered using only a subset of 300 frames, while the bottom row shows the data recovered from 1000 frames. SToRM and PSF schemes, shown in the 5th - 7th rows, relied on navigators to estimate the global manifold Laplacian. The comparisons of the reconstructions from 300 frames show that the i-SToRM scheme can provide comparable image quality to the SToRM scheme, even though it did not rely on the navigators. This iterative approach enabled us to exploit the local manifold structure of the patches (i-SToRM with patches), which significantly improved the performance over the global approach. The improved performance of SToRM and iSToRM over PSF and TV +Wavelet methods, seen by a reduced blurring of image features and improved temporal profiles, can be attributed to the improved signal modeling offered by the non-linear manifold model compared to a subspace approach or sparsity regularization. Note that the image quality of the i-SToRM with patches obtained from 300 frames is comparable to that obtained from SToRM with 1000 frames. In the last column, we report the GPC indices for both the entire images, the top value, as well as around a small region of interest containing the heart shown in the bottom. The quantitative metric shows that the reconstruction of the proposed method using 300 frames are comparable to that 1000 dataset recovered using SToRM. 74

4.3 Evaluation of the proposed i-SToRM scheme with patches on free-breathing and ungated dataset with short axis views. The dataset was collected with two acquisition schemes: a navigated acquisition scheme, as well as a golden angle sequence. The sampling trajectories for navigated and golden-angle schemes for one of the frames are shown in (a1) and (a2), respectively where the colored lines indicating the fixed navigators that are the same for all frames. 300 frames of the time series (3000 spokes, which correspond to 14 seconds of acquisition) were considered for recovery. Subfigures (b1-b3) and (c1-c3) show the recovery using navigators-free i-SToRM without patches and TV + Wavelet while (d1-d3) and (e1-e3) show the recovery using navigators-based schemes SToRM and PSF respectively. The bottom two rows show the calibration-free dataset recovered using the proposed i-SToRM method with patches (f1-f3) and TV + Wavelet (g1-g3). Note that there is no one-to-one correspondence between the two acquisitions since they were acquired at two different time points, possibly with different respiratory patterns. (a3) is the initial guess, while (a4) is the corresponding frame recovered using patch-based i-SToRM. The zoomed versions of three frames, out of 300 frames, from different phases in the dataset are shown for the entire cases. The time profiles in the fourth column are drawn for all of the frames, along the line passing through the left ventricle and right ventricle as shown in (b1). While i-SToRM is compared against SToRM and PSF using the calibration-based dataset, the calibrated-free dataset is recovered using only the proposed scheme as well as TV + Wavelet since both SToRM & PSF cannot estimate the manifold structure without navigators. The results show the ability of the proposed i-SToRM scheme in recovering quality images comparable to SToRM without relying on navigator signals. Both TV + Wavelet and PSF exhibit considerable motion artifacts and temporal blurring. The last column shows the GPC indices for both the entire images, the top value, as well as around a small region of interest containing the myocardium shown in the bottom. The quantitative metric shows an improvement of the proposed method compared to other reconstructions. 75

4.4 Recovery of the simulated CINE dataset using i-SToRM with patches (b1-b3), both calibration-based schemes SToRM (c1-c3) and PSF (d1-d3), and classical total variation with wavelet regularization (e1-e3). The simulated dynamic dataset is retrospectively undersampled using radial sampling pattern with 12 spokes, 4 navigator lines and 8 golden angle spokes per frame. One of the sampling masks is shown in (a6) with colored lines indicating the navigators. Three frames of each recon of the data corresponding to peak diastolic and systolic cardiac phases and one in transition phase are shown for each scheme. The images are cropped versions of the full frame shown in (a5) while (a4) is the initial guess. The reconstructed images are shown in the first three columns along with their error images scaled by a factor of 5 for better visualization. The time profiles in the last column are drawn for the entire recovered frames, along with the line passing through the left ventricle and right ventricle shown in (a5). We observe that i-SToRM provides reconstructions with lower spatial and temporal blurring, compared to other algorithms. While SToRM recon is quite comparable to the proposed scheme, PSF and TV + Wavelet reconstructions exhibit motion artifacts and temporal blurring respectively. The residual images show that the errors associated with i-SToRM and SToRM are more homogeneously distributed in the entire image, thus provide reduced edge blurring and better preservation of fine features, including papillary muscles. By contrast, the errors with TV + Wavelet and PSF are more concentrated in the edge regions and around the myocardial wall, indicating edge blurring. The tables at the bottom of the figure show a quantitative comparison of the entire methods using SER, HFEN, SSIM and GPC metrics computed for the entire times series on both global images as well as a square region of interest containing the heart as shown in (f1). . .

76

CHAPTER 1 INTRODUCTION

1.1 BACKGROUND

Magnetic resonance imaging (MRI) is a noninvasive, nonionizing and highly accurate imaging modality. It enables excellent visualization of both anatomical structure and physiological function. Although MRI is used to diagnose numerous medical conditions, current technology has several practical limitations, one of which is slow imaging speed. Imaging speed in MRI is limited by physical and physiological constraints associated with rapidly switching magnetically held gradients. Lack of speed poses particular challenges for applications in dynamic cardiac MRI.

To reduce artifacts related to respiratory motion, most routine cardiac MRI techniques acquire images during a patient's breath-holds. In fact, a complete acquisition takes a few cardiac cycles and may require multiple breath-holds by the patient. Thus, the patient's ability to sustain breath-holds along with imaging speed determine the duration of the examination, which in turn, determines the spatial and temporal resolution of the images. However, since many patients are unable to sustain breath-holds, the acquisition process must be accelerated to reduce scan time.

With the introduction of reduced-data imaging methods, reduction in the scan time does not require an increase in imaging speed (via enhanced gradient performance), but instead, a reduction in the number of phase-encoding lines that results in an undersampled k-space. A fundamental challenge in reduced-data imaging is to recover high-resolution images from undersampled k-space data, a problem that is often underdetermined. One common approach to solving such an underdetermined problem is to utilize the spatial and temporal structures in the images and the redundancies in the acquisition setup.

1.2 COMPRESSED SENSING

Accelerated MRI techniques reduce signal acquisition time by undersampling k-space. A fundamental problem in accelerated MRI is the recovery of quality images from undersampled k-space data. Compressed sensing has recently gained a lot of attention in many applications because it enables acquiring sparse signals from a much smaller number of samples than the ambient dimension of the signal and ensures recovery of (structured) sparse signals from undersampled, incoherent measurements. Compressed sensing takes advantage of the fact that most signals of interest in practice are sparse: there are only a few non-zero or big elements when the signals are represented over a certain dictionary such as wavelet basis. For these types of sparse or compressible signals, compressed sensing theory has established that a small number of non-adaptive measurements are often sufficient to efficiently recover them under methods such as ℓ_1 minimization.

1.3 THESIS CONTRIBUTION

Recent CS methods have employed analytically sparsifying transforms such as wavelets, curvelets, and finite differences. The reconstruction by those methods is usually seen to have many undesirable artifacts and loss of features. Recent studies have shown the promise of patch-based schemes in a variety of applications such as image/video denoising, image/video inpainting, deblurring, and demosaicing. [6–8]. The shift from global image sparsity to patch-based sparsity is appealing since patches create an additional averaging effect which helps capture image features effectively, and can potentially remove noise and motion artifacts in the dynamic images without sacrificing resolution.

In this thesis, we apply iterative algorithms of patch-smoothness regularization in medical imaging applications. These approaches are enabled by the reformulation of current non-local regularization schemes as an alternating algorithm to minimize a global criterion. We employ the ideas presented in the next sections to solve problems

arising in various MRI applications. The utility of the proposed schemes is demonstrated in the context of in-vivo static MR imaging, breath-held and free-breathing cardiac CINE MRI with multichannel acquisitions as well as simulated phantoms, myocardial perfusion MRI, gated and ungated acquisitions using both retrospective and prospective experiments. We compare the algorithms against classical compressed sensing schemes that exploit spatial or spatiotemporal finite difference sparsity, a combination of sparse and low-rank as well as state-of-the-art motion-compensated and motion-resolved methods. The prospective datasets are challenging cases since they are acquired in the ungated mode, accelerated by a high undersampling factor and considerable cardiorespiratory motion is present due to the free-breathing scan.

1.3.1 2-D IMAGE RECONSTRUCTION

Recent studies have shown the promise of patch-based schemes in a variety of applications such as image denoising, inpainting, and demosaicing. [6–8]. Non-local means (NLM) denoising algorithms recover each pixel as a weighted linear combination of all pixels in the noisy image; the inter-pixel weights were estimated as the similarity between patch neighborhoods [9–11]. This algorithm was extended to deblurring problems [12–14] by posing the recovery as an optimization scheme. However, this algorithm is not readily applicable to MRI recovery from undersampled data since the weights estimated from aliased images preserve alias patterns. Some authors have iterated between denoising and weight estimation steps [15]. However, this scheme had limited success in heavily undersampled Fourier inversion problems. This alternating NLM scheme has been recently shown to be a majorize-minimize algorithm to solve for a penalized optimization problem, where the penalty term is the sum of unweighted robust distances between image patches [4, 16, 17]. While convex distance metrics such as ℓ_1 distances may be used, nonconvex metrics that correspond to the classical NLM choices are seen to provide significantly improved image quality [4]. The availability of the global cost function enabled homotopy continuation

strategies to encourage the convergence to global minima, when non-convex metrics are used [4]. The main challenge associated with the implementation in [4] is the high computational complexity of the alternating minimization algorithm.

In this thesis, we introduce an iterative Non-Local Shrinkage (NLS) algorithm, which alternates between **(a)** evaluating the denoised inter-patch differences by shrinkage, and **(b)** computing an image that is consistent (in least-square sense) with the denoised inter-patch differences and measured data. This approach is based on additive half quadratic majorization of the patch based penalty term [18–21]. Unlike the majorization used in our previous work [4], the weights of the quadratic terms are identical for all patch pairs, but now involve new auxiliary variables that may be interpreted as the denoised inter-patch differences. We derive analytical shrinkage expressions for approximate versions of a range of distance functions that are relevant for non-local regularization; this generalizes the shrinkage formulae derived by Chartrand in the context of ℓ_p penalties [3]. The proposed approximations are the same as the Huber-like corner-rounded penalties [22–25]. The direct evaluation of the patch shrinkages are computationally expensive. We propose to exploit the redundancies in the shrinkages at adjacent pixels using separable convolution operations, thereby considerably reducing computational complexity. We validate the proposed scheme in the context of recovering MR images from undersampled measurements. This is an active research area with several applications [26–28].

1.3.2 MOTION-COMPENSATED DYNAMIC IMAGE RECONSTRUCTION

Dynamic magnetic resonance imaging (DMRI) involves imaging physiological processes that are evolving in time. Accelerated imaging involving sparse k - t sampling and constrained reconstruction has demonstrated great potential to improve DMRI [29–36]. Several regularization schemes including sparsity-based penalties [31, 33, 37–40], low-rank penalties [41–48] and combination of sparse and low-rank constraints [44, 48, 49] were introduced to accelerate imaging. These methods provide

superior reconstructions when the inter-frame motion (e.g in breath-held and gated acquisitions) is relatively low. However, the parsimonious assumptions made by these schemes often break down in the presence of large inter-frame motion, which restricts the performance of these methods in free-breathing and/or ungated applications.

To address the above challenge, several motion estimation and compensation (ME-MC) schemes have been developed; these methods alternate between explicit estimation of inter-frame motion, followed by motion-compensated reconstruction [50–54]. For example, the k-t FOCUSS scheme with ME-MC [50], which was introduced for cardiac cine MRI, alternates between motion estimation using block matching and sparsity based regularization of the residuals. Similarly, regional low-rank constraint, coupled with deformation estimation, was introduced in [51] to account for contrast variations in myocardial perfusion MRI. A generalized deformation compensated compressed sensing (DC-CS) scheme capable to include a variety of penalties (e.g. sparse, low-rank) has also been proposed [55, 56]. Other ME-MC schemes include motion-adaptive spatiotemporal regularization (MASTER) [57] differ in the type of the motion model as well as the exact regularization penalties. The main challenge with all of these schemes is the complex motion estimation step, often involving a computationally expensive deformable image registration, block matching, or optical flow algorithms [57–59]. In addition, the lack of a unifying cost function restricts the analysis of the convergence of the joint algorithm to undesirable fixed points. The above mentioned challenges limit the utility of these scheme in applications.

In this thesis, we propose a computationally efficient, patch smoothness regularization framework to overcome the above-mentioned drawbacks. The proposed scheme exploits the similarity of rectangular image sub-patches in a frame with other patches in its spatiotemporal neighborhood (see Fig 3.1). The regularization penalty, which involves the sum of robust inter-patch distances between patches in each others' neighborhood, is similar to standard penalties in compressed sensing. The inter-patch

distance metric is chosen to heavily penalize small differences, while the metric saturates for large differences [60]. By comparing the neighboring patches in both spatial and temporal directions, the proposed framework implicitly compensates for the local motion of the pixels across time, therefore avoiding unnecessary explicit image registration or computation of the motion vectors (see Fig 3.1). We use the majorization of the regularization penalty to simplify the optimization scheme as an alternating minimization strategy; the algorithm alternates between an analytical inter-patch shrinkage step, and a quadratic update step that is efficiently solved by a conjugate gradient (CG) algorithm. The presence of a common cost function for these two steps enables us to derive efficient continuation strategies that encourage the convergence to the global minimum.

The PRICE scheme also has conceptual similarities to patch-based methods that rely on dictionary learning used in several applications including dynamic MRI [61,62]. In contrast to these schemes, we considerably reduce the search space by focusing on a smaller search neighborhood; this results in an algorithm whose computational complexity is comparable to classical total variation regularization. The PRICE scheme also has similarities to [63] that uses a combination of 2-D spatial and 1-D temporal non-local penalties. However, [63] does not compare a patch to shifted patches in the neighboring frames.

1.3.3 MOTION-RESOLVED DYNAMIC IMAGE RECONSTRUCTION

Clinical dynamic imaging schemes often collect k-t space data in a breath-held segmented mode. These approaches make it challenging to acquire data from several patient groups (e.g. claustrophobic, pediatric subjects and obese patients), who have difficulty in holding their breath. In addition, the achievable spatial resolution is often severely limited by the typical breath-hold durations. Another challenge is the long duration of the exam, which makes cardiac MRI expensive and reduces patient comfort.

Respiratory gating methods were introduced to eliminate the need for breath-holding. These methods rely on respiratory bellows, self-gating, or navigator signals [64, 65] to select the k-space data from a specific respiratory phase. The main challenge associated with these methods is low acquisition efficiency. While low-rank methods [43, 44, 49, 66] provide good reconstructions in breath-held mode, the direct application of these methods to the setting with extensive cardiac and respiratory motion is challenging. Motion compensated reconstruction schemes were introduced to improve acquisition efficiency [54, 55, 57–59]. These approaches rely on joint compressed sensing and motion compensation to recover the images from multiple phases simultaneously while estimating the motion between phases using deformable registration. The main downside of these schemes is the considerable computational complexity needed to recover the data from multiple cardiac and respiratory phases.

Recently, several researchers have proposed motion resolved recovery schemes, which estimate the cardiac and respiratory phases from golden angle radial acquisitions. These methods estimate the phase information by filtering the series of central k-space samples acquired at each shot [48, 67]. The binned four-dimensional data (two spatial dimensions, a respiratory dimension, and a cardiac phase dimension) is then recovered using spatiotemporal total variation regularization. While the good performance of these methods has been demonstrated in several subjects, their utility in subjects with irregular respiration and cardiac motion (e.g arrhythmia) is not clear. The use of navigators at every alternate acquisition considerably simplifies the estimation of the phases as shown in [48, 49]. However, this approach comes at the expense of 50% overhead in acquiring the navigator signal.

In this thesis, we build upon our recent SToRM framework [5] and related manifold based approaches [68], which rely on an implicit binning strategy using navigators. SToRM assumes the images in a free-breathing and ungated dataset to be points on a smooth and low-dimensional manifold. The Laplacian matrix that specifies the

structure of the manifold, or equivalently the similarity between image pairs in the dataset, is estimated from navigator signals. The main advantage of this implicit motion-resolved scheme over explicit binning strategies is the recovery of the natural dynamics in a real-time acquisition mode. While this approach offers good reconstructions, SToRM's dependency on radial navigators lowers the scanning acquisition efficiency. Specifically, 2-4 radial lines per frame are usually needed for good recovery and approximately 20-40% of the scan time is devoted to the acquisition of those navigators. This approach also results in reduced incoherence between sampling patterns of different frames, and makes it difficult for the future extension of this scheme to 3-D applications. Another challenge is that SToRM requires a relatively long acquisition duration (≈ 1 minute per slice) to ensure that the complex image manifold is well-sampled. Specifically, since SToRM relies on the similarity between images in the dataset, a large number of images are needed to ensure that all the phases are well represented.

The focus of this work is to overcome the drawbacks associated with SToRM while maintaining the good quality of the recon, by exploiting the manifold structure of localized image patches in the dataset. Separately exploiting the manifold structure of these localized regions is far more effective; since the manifolds are relatively simpler, fewer images (and hence shorter acquisitions) are sufficient to ensure good sampling. In addition to eliminating the dependence on navigators, this approach facilitates the extension of the global SToRM framework to exploit the local manifold structure of image patches.

1.4 ORGANIZATION

Chapter 2, introduces a fast iterative shrinkage algorithm for patch-smoothness regularization in 2-D applications. In Chapter 3, an efficient PRICE scheme, which implicitly compensates for inter-frame motion, is introduced to recover dynamic MRI data from highly undersampled measurements. In Chapter 4, we develop a motion-

resolved manifold regularization scheme for accelerating free breathing ungated dynamic MR imaging. Finally, we summarize our work and possible future extensions in chapter 5.

Figure 1.1 illustrates the proposed PRICE and iSTORM schemes covering 2.8.0.4 and 3.5, while the scheme mentioned in 2 is a simpler version of those schemes introduced to recover the static 2D images. In the case of PRICE, the metric penalizes the differences between each patch and other patches in its cube-shaped neighborhood in both spatiotemporal directions. In iSTORM, the metric is used to calculate the weights between the frames that have the same cardiac and respiratory phases. The formulation of motion compensation or resolution recovery in a unified cost function enables us to come up with effective optimization algorithms that are more computationally efficient than current state-of-the-art methods. The patch regularization metric can either compensate for the motion or can pick the respiratory phases that match each other, which may not be that close on the real sequence. The redundancies between adjacent frames in the presence of motion can be exploited using patch smoothness regularization; while the redundancies between frames in the same cardiac and respiratory phases can be exploited using image manifold smoothness regularization, thus the developed schemes provide either implicit motion-compensated or implicit motion-resolved recovery. These implicit strategies with well-defined energy minimization formulations are more effective and computationally efficient than explicit motion compensation and other gating methods. PRICE and iSTORM alternate between inter-patch differences estimation and image update step, which involves a computationally efficient conjugate gradients algorithm.

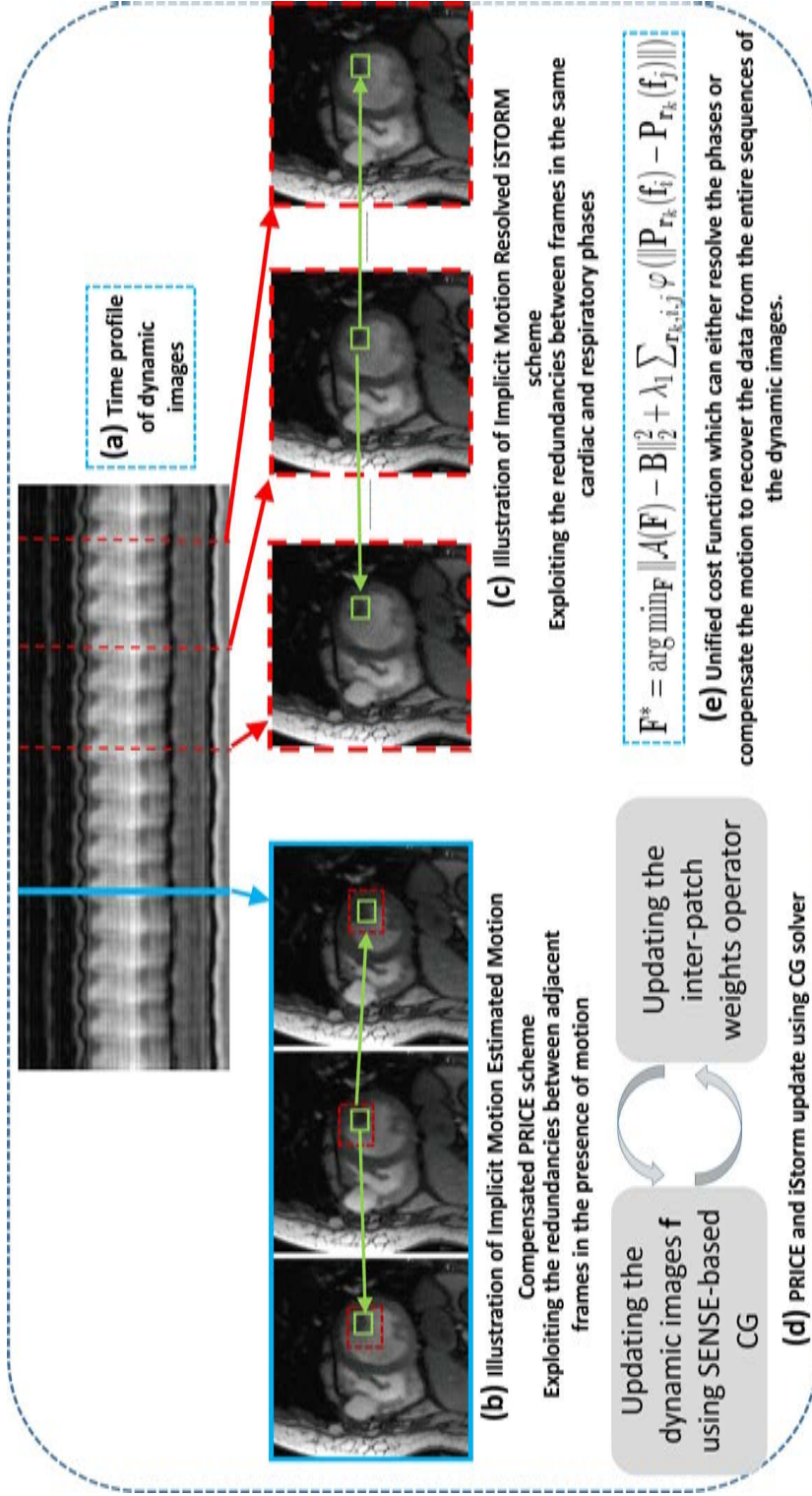


Figure 1.1: Illustration of the proposed PRICE and iSTORM schemes. The time profile in the top row is drawn along myocardium such that the cardiorespiratory motions are shown. The chosen frames are depicted in the time profiles with their perspective colors. In the case of PRICE, subfigure (b), the metric penalizes the differences between each patch and other patches in its cube-shaped neighborhood in both spatiotemporal directions. The green squares indicate the location of the patch in the current frame and the ones with the highest similarity in the neighboring frames shown in the blue boxes. The dashed red box represents the neighborhood where the patches move within. In iSTORM, the metric is used to calculate the weights between the frames that have the same cardiac and respiratory phases. PRICE and iSTORM alternate between inter-patch differences estimation and image update step, which involves a computationally efficient conjugate gradients algorithm. The NLS scheme is a simple version of those schemes aimed to recover the static images analytically.

CHAPTER 2 FAST NOVEL PATCH-BASED ITERATIVE SHRINKAGE SCHEME

2.1 ABSTRACT

In this chapter, we introduce a fast iterative shrinkage algorithm for patch-smoothness regularization of inverse problems in medical imaging. This approach is enabled by the reformulation of current non-local regularization schemes as an alternating algorithm to minimize a global criterion. The proposed algorithm alternates between evaluating the denoised inter-patch differences by shrinkage and computing an image that is consistent with the denoised inter-patch differences and measured data. We derive analytical shrinkage rules for several penalties that are relevant in non-local regularization. The redundancy in patch comparisons used to evaluate the shrinkage steps are exploited using convolution operations. The resulting algorithm is observed to be considerably faster than current alternating non-local algorithms. The proposed scheme is applicable to a large class of inverse problems including deblurring, denoising, and Fourier inversion. The comparisons of the proposed scheme with state-of-the-art regularization schemes in the context of recovering images from undersampled Fourier measurements demonstrate a considerable reduction in alias artifacts and preservation of edges.

2.2 METHOD

2.2.1 Problem Formulation

We consider the recovery of a complex image $f : \Omega \rightarrow \mathbb{C}$ from its measurements \mathbf{b} . Here, $\Omega \subset \mathbb{Z}^2$ is the spatial support of the complex image. We model the acquisition scheme by the linear degradation operator \mathbf{A} :

$$\mathbf{b} = \mathbf{A}\mathbf{f} + \mathbf{n}. \quad (2.1)$$

For example, $\mathbf{A} \in \mathbb{C}^{M \times N}$ corresponds to a convolution in the deconvolution setting, a Fourier matrix in the case of Fourier inversion, or identity matrix in the case of denoising. Here, $\mathbf{f} \in \mathbb{C}^N$ is a vector obtained by the concatenating the rows in a 2-D image $f(\mathbf{x})$ and $\mathbf{b} \in \mathbb{C}^M$ is the vector of measurements. We assume \mathbf{n} to be Gaussian distributed white noise process of a specified standard deviation σ .

2.2.2 Unified Non-Local Regularization

The iterative algorithm that alternates between classical non-local image recovery [69] and the re-estimation of weights was shown in [4] to be a majorize-minimize (MM) algorithm:

$$\hat{\mathbf{f}} = \arg \min_{\mathbf{f}} \underbrace{\|\mathbf{A}\mathbf{f} - \mathbf{b}\|^2 + \lambda \mathcal{G}(\mathbf{f})}_{\mathcal{C}(\mathbf{f})}, \quad (2.2)$$

where $\|\mathbf{A}\mathbf{f} - \mathbf{b}\|^2$ is the data fidelity term, and the regularization functional $\mathcal{G}(\mathbf{f})$ is specified by:

$$\mathcal{G}(\mathbf{f}) = \sum_{\mathbf{x}} \sum_{\mathbf{y} \in \mathbf{x} + \mathcal{N}} \varphi(P_{\mathbf{x}}(\mathbf{f}) - P_{\mathbf{y}}(\mathbf{f})). \quad (2.3)$$

Here φ is an appropriately chosen potential function and $P_{\mathbf{x}}(\mathbf{f})$ is a patch extraction operator which extracts an image patch centered at the spatial location \mathbf{x} from the image \mathbf{f} ; i.e. $P_{\mathbf{x}}(\mathbf{f})$ can be written as $\mathbf{f}(\mathbf{x} + \mathbf{p})$, where $\mathbf{p} \in \mathcal{B}$ denotes the indices in the patch. For example, if we choose a square patch of size $(2N + 1)$, the set $\mathcal{B} = [-N, \dots, N] \times [-N, \dots, N]$. Similarly, \mathcal{N} are the indices of the search neighborhood; the patch $P_{\mathbf{x}}(\mathbf{f})$ is compared to all the patches whose centers are specified by $\mathbf{x} + \mathcal{N}$. For example, if we choose a square shaped neighborhood of size $2M + 1$, the set $\mathcal{N} = [-M, \dots, M] \times [-M, \dots, M]$. The shape of the patches and the search neighborhood may be easily changed by re-defining the sets \mathcal{N} and \mathcal{B} . In this research, we focus on potential functions of the form:

$$\varphi(\mathbf{g}) = \phi(\|\mathbf{g}\|), \quad (2.4)$$

where $\phi : \mathbb{R}^+ \rightarrow \mathbb{R}^+$ is an appropriately chosen distance metric and $\|\mathbf{g}\|^2 = \sum_{\mathbf{p} \in \mathcal{B}} |g(\mathbf{p})|^2$.

2.2.3 Solution Using an Iterative Reweighted Algorithm

It is showed in [4] that equation (2.2) can be solved using a majorize-minimize algorithm, where the regularization term is majorized by the weighted sum of patch differences:

$$\mathcal{G}(\mathbf{f}) \leq \underbrace{\sum_{\mathbf{x}} \sum_{\mathbf{p} \in \mathcal{N}} w_n(\mathbf{x}, \mathbf{x} + \mathbf{p}) \|P_{\mathbf{x}}(\mathbf{f}) - P_{\mathbf{x}+\mathbf{p}}(\mathbf{f})\|^2}_{\mathcal{G}_n(\mathbf{f})}. \quad (2.5)$$

The above relation is essentially the classical multiplicative half-quadratic majorization [19, 20, 70] of the penalty in equation (2.2). The weights $w_n(\mathbf{x}, \mathbf{x} + \mathbf{p})$ in equation (2.5) are specified by:

$$w_n(\mathbf{x}, \mathbf{y}) = \frac{\phi'(\|P_{\mathbf{x}}(\mathbf{f}_n) - P_{\mathbf{y}}(\mathbf{f}_n)\|)}{2\|P_{\mathbf{x}}(\mathbf{f}_n) - P_{\mathbf{y}}(\mathbf{f}_n)\|}. \quad (2.6)$$

Here, \mathbf{f}_n is an image vector at the n^{th} iteration. Each iteration of the MM algorithm involves the minimization of the criterion:

$$\mathbf{f}_{n+1} = \arg \min_{\mathbf{f}} \|\mathbf{A}\mathbf{f} - \mathbf{b}\|^2 + \lambda \mathcal{G}_n(\mathbf{f}). \quad (2.7)$$

Note from equation (2.5) that \mathcal{G}_n is a weighted linear combination of patch differences, where the weights $w_n(\mathbf{x}, \mathbf{x} + \mathbf{p})$ are spatially varying. This makes it difficult to develop a closed form expression to solve equation (2.7). As discussed above, one of the main challenges of the algorithm is its high computational complexity. Specifically, the conjugate gradients algorithm to solve equation (2.7) converges slowly, especially as the weights increase.

2.3 PROPOSED ALGORITHM

2.3.1 Majorization of the Penalty Term

In this research, we will consider the additive half-quadratic majorization [18, 21, 70] of the potential function φ , specified by:

$$\varphi(\mathbf{t}) \triangleq \min_{\mathbf{s}} \left\{ \psi(\mathbf{s}) + \frac{\beta}{2} \|\mathbf{s} - \mathbf{t}\|^2 \right\} \quad (2.8)$$

This additive half-quadratic majorization scheme was originally introduced for edge preserving gradient regularization; using this scheme has not been reported in patch regularization before. With additional simplifications below, using this scheme results in a fast algorithm. The function ψ in equation (2.8) depends on φ and β , while \mathbf{s} is an auxiliary variable. Since φ is the minimum of $\psi(\mathbf{s}) + \frac{\beta}{2} \|\mathbf{s} - \mathbf{t}\|^2$, we will also solve for \mathbf{s} along with \mathbf{t} . Note that unlike equation (2.5), the quadratic term on the right hand side of equation (2.8) is weighted by the scalar $\beta/2$, which is the same for all spatial locations. The spatial invariance of the weights enables us to analytically solve a key subproblem, which is not possible with equation (2.5). Using equation (2.8), we express the original problem in equation (2.2) as:

$$\hat{\mathbf{f}} = \arg \min_{\mathbf{f}} \min_{\{\mathbf{s}_{\mathbf{x},\mathbf{q}}\}} \|\mathbf{A}\mathbf{f} - \mathbf{b}\|^2 + \lambda \sum_{\mathbf{x}} \sum_{\mathbf{q} \in \mathcal{N}} \psi(\mathbf{s}_{\mathbf{x},\mathbf{q}}) + \lambda \frac{\beta}{2} \sum_{\mathbf{x}} \sum_{\mathbf{q} \in \mathcal{N}} \|P_{\mathbf{x}}(\mathbf{f}) - P_{\mathbf{x}+\mathbf{q}}(\mathbf{f}) - \mathbf{s}_{\mathbf{x},\mathbf{q}}\|^2. \quad (2.9)$$

Note that the solution involves the minimization with respect to both \mathbf{f} and the variables $\{\mathbf{s}_{\mathbf{x},\mathbf{q}}\}$. We use an alternating minimization algorithm, where we alternate between two steps. In the first step, we minimize equation (2.9) with respect to $\{\mathbf{s}_{\mathbf{x},\mathbf{q}}\}$, assuming \mathbf{f} to be fixed. In the second step, we solve for \mathbf{f} , assuming $\{\mathbf{s}_{\mathbf{x},\mathbf{q}}\}$ to be fixed, these steps can be solved analytically. The efficient implementation of these subproblems is the main reason why the proposed algorithm is faster than the iterative reweighted implementation. Similar speed-ups were reported with using the

half-quadratic regularization scheme in the context of other regularization penalties [18, 21, 70].

2.3.2 The s Sub-Problem: solve for $\mathbf{s}_{\mathbf{x},\mathbf{q}}$, assuming \mathbf{f} fixed

We focus on minimizing equation (2.9) with respect to the auxiliary variables $\{\mathbf{s}_{\mathbf{x},\mathbf{q}}\}$, assuming \mathbf{f} to be a constant in this subsection. In this case, determining each of the auxiliary variables $\mathbf{s}_{\mathbf{x},\mathbf{q}}$ corresponding to different values of \mathbf{x} and \mathbf{q} can be treated independently:

$$\bar{\mathbf{s}}_{\mathbf{x},\mathbf{q}} = \arg \min_{\mathbf{s}_{\mathbf{x},\mathbf{q}}} \frac{\beta}{2} \|P_{\mathbf{x}}(\mathbf{f}) - P_{\mathbf{x}+\mathbf{q}}(\mathbf{f}) - \mathbf{s}_{\mathbf{x},\mathbf{q}}\|^2 + \psi(\mathbf{s}_{\mathbf{x},\mathbf{q}}).$$

We showed in [2] that with a convex hull approximation of the function $\beta|t|^2/2 - \varphi(t)$, we can analytically determine $\mathbf{s}_{\mathbf{x},\mathbf{q}}$ as a shrinkage for all penalties of interest:

$$\bar{\mathbf{s}}_{\mathbf{x},\mathbf{q}} = [P_{\mathbf{x}}(\mathbf{f}) - P_{\mathbf{x}+\mathbf{q}}(\mathbf{f})] \nu(\|P_{\mathbf{x}}(\mathbf{f}) - P_{\mathbf{x}+\mathbf{q}}(\mathbf{f})\|), \quad (2.10)$$

where $\nu : \mathbb{R}^+ \rightarrow \mathbb{R}^+$ is a function that depends on the distance metric ϕ . We determined the shrinkage rules corresponding to the useful penalties in details in [2].

2.3.3 The f Sub-Problem: solve for f , assuming $\mathbf{s}_{\mathbf{x},\mathbf{q}}$ fixed

In this subsection, we focus on minimizing equation (2.9) with respect to \mathbf{f} , assuming the auxiliary variables $\{\mathbf{s}_{\mathbf{x},\mathbf{q}}\}$ to be fixed. We show that this quadratic sub-problem can be solved analytically in the Fourier domain for several measurement operators. Minimizing equation (2.9) with respect to \mathbf{f} , assuming $\{\mathbf{s}_{\mathbf{x},\mathbf{q}}\}$ fixed, simplifies to:

$$\hat{\mathbf{f}} = \arg \min_{\mathbf{f}} \|\mathbf{A}\mathbf{f} - \mathbf{b}\|^2 + \underbrace{\frac{\lambda\beta}{2} \sum_{\mathbf{x};\mathbf{q} \in \mathcal{N}} \|P_{\mathbf{x}}(\mathbf{f}) - P_{\mathbf{x}+\mathbf{q}}(\mathbf{f}) - \mathbf{s}_{\mathbf{x},\mathbf{q}}\|^2}_{\mathcal{R}(\mathbf{f})} \quad (2.11)$$

The above quadratic penalty may be solved using the conjugate gradients algorithm. However, we will now simplify it to an expression that can be solved analytically,

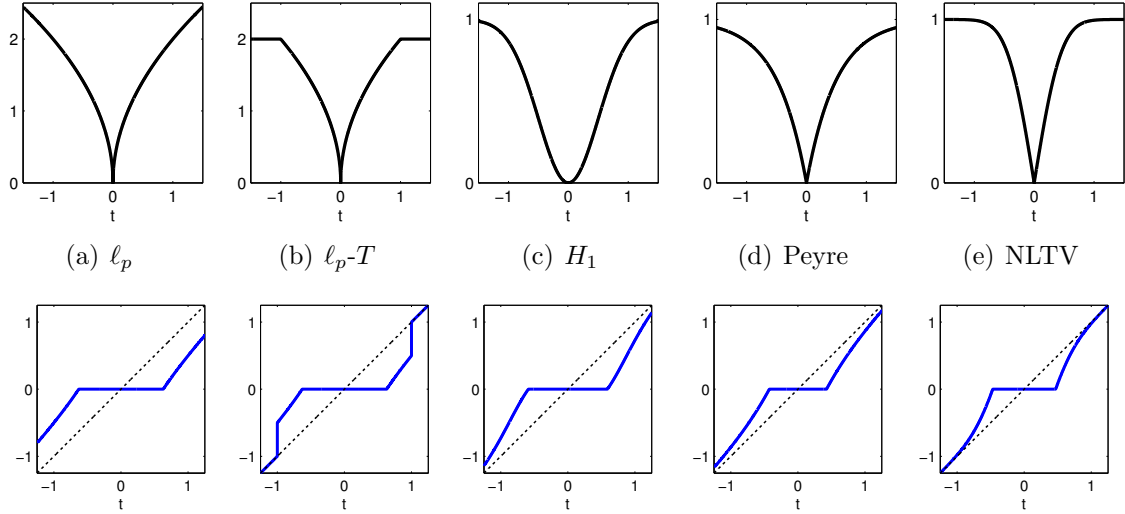


Figure 2.1: Distances functions $\phi(t)$ that are relevant in non-local regularization (first row) and the associated shrinkage rules $t \cdot \nu(|t|)$ (second row); see Appendix B in [2] for the corresponding formulas that relies on a convex hull approximation of the original penalty. Here we illustrate the shrinkage rules in 1-D for the parameter choices $\beta = 2$, $p = 0.5$, $T = 1$, and $\sigma = 0.5$. The approach introduced in the research enables evaluating the shrinkage rules for a much larger class of penalties, generalizing the results in [3] for ℓ_p penalties shown in the first column.

which is considerably more efficient. The quadratic penalty term involves differences between multiple patches in the image, each of which is a linear combination of quadratic differences between image pixels. The differences between two specific pixels are thus involved in different patch differences. We show in Appendix A that the pixel differences from several patches can be combined to obtain the following pixel-based penalty:

$$\hat{\mathbf{f}} = \arg \min_{\mathbf{f}} \|\mathbf{A}\mathbf{f} - \mathbf{b}\|^2 + \lambda \frac{\beta}{2} \sum_{\mathbf{q} \in \mathcal{N}} \|\mathbf{D}_{\mathbf{q}}\mathbf{f} - \mathbf{h}_{\mathbf{q}}\|^2. \quad (2.12)$$

Here, $\mathbf{D}_{\mathbf{q}}$ is the finite difference operator

$$(\mathbf{D}_{\mathbf{q}}\mathbf{f})(\mathbf{x}) = \mathbf{f}(\mathbf{x}) - \mathbf{f}(\mathbf{x} + \mathbf{q}). \quad (2.13)$$

The images $\mathbf{h}_{\mathbf{q}}(\mathbf{x})$, $\mathbf{q} \in \mathcal{N}$, are obtained from the patch shrinkages as:

$$\mathbf{h}_{\mathbf{q}} = (\mathbf{D}_{\mathbf{q}}\mathbf{f}) \bullet \mathbf{v}_{\mathbf{q}}. \quad (2.14)$$

Here, \bullet denotes the entrywise multiplication of the vectors, and $\mathbf{v}_{\mathbf{q}}$ is obtained by summing the shrinkage weights of nearby patch pairs:

$$\mathbf{v}_{\mathbf{q}}(\mathbf{x}) = \sum_{\mathbf{p} \in \mathcal{B}} \underbrace{\nu(\|P_{\mathbf{x}+\mathbf{p}}(\mathbf{f}) - P_{\mathbf{x}+\mathbf{p}+\mathbf{q}}(\mathbf{f})\|)}_{\mathbf{u}_{\mathbf{q}}(\mathbf{x})}. \quad (2.15)$$

We solve equation (2.12) in the Fourier domain for measurement operators \mathbf{A} that are diagonalizable in the Fourier domain.

2.3.4 Determination of Shrinkage Rules

The existence of an analytical solution to (2.7) is key to the fast implementation of the alternating minimization scheme. In this section, we determine analytical shrinkage rules for a larger class of potential functions. The main idea is to use properties of convex conjugate functions to derive the dual function $\psi(\mathbf{s})$ in (2.8), which is required for the solution of (2.7). However, this approach requires certain convexity requirements which are not met by many potential functions of practical interest. Therefore, we propose a procedure for approximating potential functions that yields an analytical shrinkage rule. This quality of this approximation is controlled by a parameter β , becoming exact as $\beta \rightarrow \infty$.

We rewrite (2.8) as:

$$\varphi(\mathbf{t}) = \min_{\mathbf{s}} \left\{ \psi(\mathbf{s}) + \frac{\beta}{2} \left(\|\mathbf{s}\|^2 - 2\Re(\langle \mathbf{s}, \mathbf{t} \rangle) + \|\mathbf{t}\|^2 \right) \right\},$$

where $\Re(x)$ is the real part of x . The above equation is further rearranged as:

$$\underbrace{\frac{\|\mathbf{t}\|^2}{2} - \frac{1}{\beta}\varphi(\mathbf{t})}_{r(\mathbf{t})} = \max_{\mathbf{s}} \left\{ \Re(\langle \mathbf{s}, \mathbf{t} \rangle) - \underbrace{\left(\frac{1}{\beta}\psi(\mathbf{s}) + \frac{\|\mathbf{s}\|^2}{2} \right)}_{g(\mathbf{s})} \right\} \quad (2.16)$$

From the theory in [71], the above relation is satisfied when $r(\mathbf{t})$ is a convex function, in which case $g = r^*$, the Legendre-Fenchel dual (or convex conjugate) of r :

$$r^*(\mathbf{s}) = \max_{\mathbf{t}} \{ \Re(\langle \mathbf{s}, \mathbf{t} \rangle) - r(\mathbf{t}) \}. \quad (2.17)$$

However, the function r is not convex for most penalties φ that we are interested in, especially for small values of β . When r is not convex, we propose to approximate r by a convex function \hat{r} so that relation equation (3.9) is satisfied. We choose \hat{r} such that the epigraph of \hat{r} is the convex hull of the epigraph of r ; \hat{r} is thus the closest convex function to r (see Fig. 2.2.b). For φ functions of the form (2.4), we have $r(\mathbf{t}) = q(\|\mathbf{t}\|)$, where the function $q : \mathbb{R}^+ \rightarrow \mathbb{R}^+$ is specified by $q(t) = t^2/2 - \phi(t)/\beta$. In all the cases we consider in this paper (see Appendix B), we can obtain the convex hull approximation of r as

$$\hat{r}(\mathbf{t}) = \begin{cases} q(\|\mathbf{t}\|) & \text{if } q'(\|\mathbf{t}\|) > 0 \\ c & \text{else} \end{cases}, \quad (2.18)$$

where c is an appropriately chosen constant to ensure continuity of \hat{r} ; see Fig. (2.2 b) for an example. The convex hull approximation of $r(\mathbf{t})$ is equivalent to approximating the original penalty $\varphi(\mathbf{t})$ as:

$$\hat{\varphi}(\mathbf{t}) := \beta \left(\frac{\|\mathbf{t}\|^2}{2} - \hat{r}(\mathbf{t}) \right);$$

see Fig. (2.2c). For the potentials considered in this paper, this ‘‘Huber-like’’ approx-

imation:

$$\hat{\varphi}(\mathbf{t}) = \begin{cases} \frac{\beta \|\mathbf{t}\|^2}{2} - c & \text{if } \|\mathbf{t}\| < L \\ \phi(\|\mathbf{t}\|) & \text{else} \end{cases}, \quad (2.19)$$

amounts to approximating the cusp of the original potential function at the origin by a quadratic function. Note that $L = L(\beta) \rightarrow 0$ as $\beta \rightarrow \infty$, when the approximation of φ by $\hat{\varphi}$ is exact. In particular we have $\hat{\varphi} \rightarrow \varphi$ uniformly as $\beta \rightarrow \infty$; see Fig. (2.2 d). This approximation enables us to derive the analytical solution for (2.7), which is termed as a shrinkage rule. The shrinkage rule in (2.7) involves computing $\bar{\mathbf{s}}$ specified

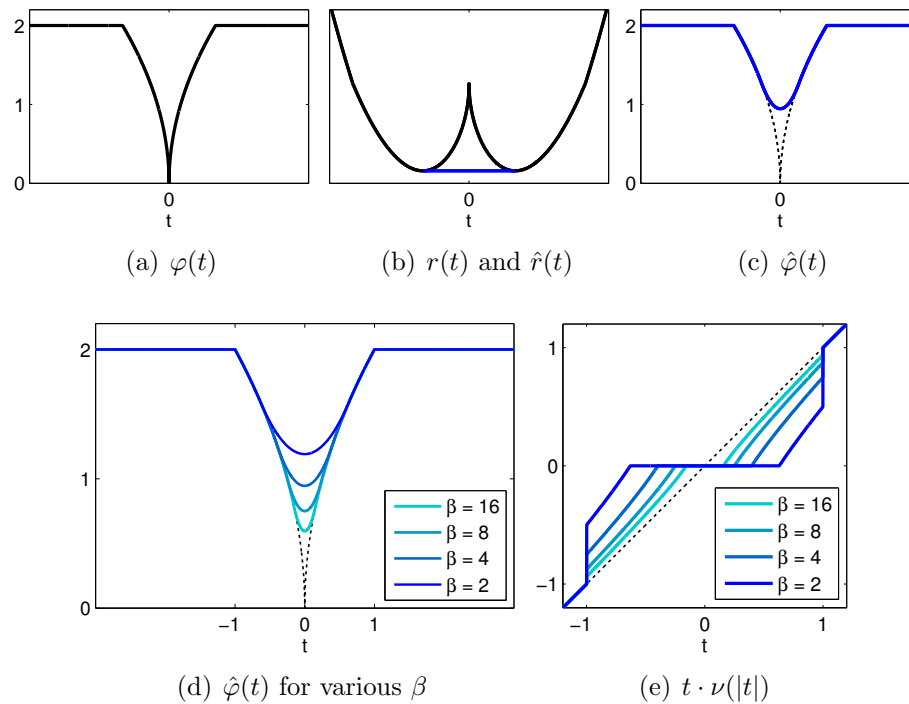


Figure 2.2: Approximation of the potential function: (a) shows the original potential function $\varphi(t)$ in 1-D, which is the truncated ℓ_p ; $p = 0.5$ penalty, $T = 1$. (b) indicates the corresponding $r(t) = t^2/2 - \frac{1}{\beta}\varphi(t)$ function with $\beta = 2$, shown in black. Note that this function is non-convex. Hence, we approximate this function by $\hat{r}(t)$ shown in blue, which is the best convex approximation of $r(t)$. The corresponding modified potential function is shown in blue in (c). (d) indicates the approximations for different values of β . Note that the approximations converge uniformly to φ . (e) shows the corresponding shrinkage rules. The potential functions and shrinkage rules for different penalties are shown in Fig. 2.1.

by:

$$\bar{\mathbf{s}}(\mathbf{t}) = \arg \min_{\mathbf{s}} \left\{ \psi(\mathbf{s}) + \frac{\beta}{2} \|\mathbf{s} - \mathbf{t}\|^2 \right\}$$

which is often called the proximal mapping of ψ . The above equation can be simplified as

$$\begin{aligned} \bar{\mathbf{s}}(\mathbf{t}) &= \arg \min_{\mathbf{s}} \left\{ \beta \left(\frac{1}{\beta} \psi(\mathbf{s}) + \frac{\|\mathbf{s}\|^2}{2} + \frac{\|\mathbf{t}\|^2}{2} - \langle \mathbf{s}, \mathbf{t} \rangle \right) \right\} \\ &= \arg \max_{\mathbf{s}} \left\{ \langle \mathbf{s}, \mathbf{t} \rangle - \underbrace{\left(\frac{\|\mathbf{s}\|^2}{2} + \frac{1}{\beta} \psi(\mathbf{s}) \right)}_{\hat{r}^*(\mathbf{s})} \right\} \end{aligned} \quad (2.20)$$

Differentiating the right hand side of equation (2.20) with respect to \mathbf{s} and setting it to zero, we obtain $\mathbf{t} - \partial \hat{r}^*(\bar{\mathbf{s}}) \ni 0$, or equivalently,

$$\bar{\mathbf{s}}(\mathbf{t}) \in (\partial \hat{r}^*)^{-1}(\mathbf{t}).$$

Since the subgradients of Legendre-Fenchel duals satisfy $(\partial \hat{r}^*)^{-1}(\mathbf{t}) = (\partial \hat{r})(\mathbf{t})$, we have

$$\bar{\mathbf{s}}(\mathbf{t}) \in \partial \hat{r}(\mathbf{t}). \quad (2.21)$$

Considering the expression for the convex hull approximation of \hat{r} in equation (2.18), we have:

$$\bar{\mathbf{s}}(\mathbf{t}) = \begin{cases} q'(\|\mathbf{t}\|) \frac{\mathbf{t}}{\|\mathbf{t}\|} & \text{if } q'(\|\mathbf{t}\|) > 0 \\ 0 & \text{else.} \end{cases}$$

Setting $q(t) = t^2/2 - \phi(t)/\beta$ in the above equation, we obtain the shrinkage rule as:

$$\begin{aligned}\bar{\mathbf{s}}(\mathbf{t}) &= \frac{\mathbf{t}}{\|\mathbf{t}\|} \left(\|\mathbf{t}\| - \frac{1}{\beta} \phi'(\|\mathbf{t}\|) \right)_+ \\ &= \mathbf{t} \underbrace{\left(1 - \frac{\phi'(\|\mathbf{t}\|)}{\beta \|\mathbf{t}\|} \right)_+}_{\nu(\|\mathbf{t}\|)},\end{aligned}\tag{2.22}$$

where $(\cdot)_+ := \max\{\cdot, 0\}$. Here, $\nu(\|\mathbf{t}\|)$ is a scalar between 0 and 1, which when multiplied by \mathbf{t} will yield the shrinkage of \mathbf{t} . Setting $\mathbf{t} = P_{\mathbf{x}}(\mathbf{f}) - P_{\mathbf{x}+\mathbf{q}}(\mathbf{f})$ in the above equation, we obtain the shrinkage rules to be used in (3.10). Note that the above approach can be adapted to most penalties. We determine the shrinkage rules and the associated ν functions for common penalty functions φ in non-local regularization in Appendix B. Figure (2.1) shows the penalty functions for different metrics and the corresponding shrinkage weights. We observe that the derived shrinkage rule for the $\mathbf{s}_{\mathbf{x},\mathbf{q}}$ sub-problem is only exact for the convex hull approximation \hat{r} in (2.18). However, note the Huber-like approximations of the penalties corresponding to \hat{r} specified by (2.19) approach the original penalty as $\beta \rightarrow \infty$.

2.4 IMPLEMENTATION

We now focus on the implementation of the sub-problems. Specifically, we show that all of the above steps can be solved analytically for many penalties and measurement operators \mathbf{A} that are diagonalizable by the Fourier domain (e.g. Fourier sampling, deblurring). This enables us to realize a computationally efficient algorithm. We also introduce a continuation scheme to improve the convergence of the algorithm.

2.4.1 Analytical Solution of equation (2.11) in the Fourier Domain

The Euler-Lagrange equation for equation (2.12) is given by:

$$\left(2\mathbf{A}^H \mathbf{A} + \lambda\beta \sum_{\mathbf{q} \in \mathcal{N}} \mathbf{D}_{\mathbf{q}}^H \mathbf{D}_{\mathbf{q}} \right) \mathbf{f} = 2\mathbf{A}^H \mathbf{b} + \lambda\beta \sum_{\mathbf{q} \in \mathcal{N}} \mathbf{D}_{\mathbf{q}}^H \mathbf{h}_{\mathbf{q}} \quad (2.23)$$

Here \mathbf{B}^H denotes the Hermitian transpose of matrix \mathbf{B} . We now aim to solve for \mathbf{f} , assuming $\mathbf{h}_{\mathbf{q}}; \mathbf{q} \in \mathcal{N}$ in the left hand side of equation (2.23) to be pre-determined from the previous iterate \mathbf{f}_{n-1} . Thus, this step involves the solution to a linear system of equations. Motivated by analytical solutions to similar problems in the context of total variation minimization [72], we propose to solve for equation (2.23) in the Fourier domain. Specifically, the measurement operator \mathbf{A} is diagonalizable in the Fourier domain in many inverse problems of interest (e.g. Fourier sampling, deblurring). In these cases, we may write $\mathbf{A}^H \mathbf{A}$ as a pointwise multiplication in the Fourier domain. For instance, in the particular case when \mathbf{A} is a Cartesian Fourier undersampling operator, we may write

$$\mathbf{A}^H \mathbf{A} \mathbf{f} = \mathcal{F}^{-1}(\mathbf{a} \bullet \mathcal{F}(\mathbf{f})) \quad (2.24)$$

where \mathcal{F} discrete Fourier transform and \mathbf{a} is a vector of ones and zeros corresponding to the Fourier sample locations. It is well-known that the operators $\mathbf{D}_{\mathbf{q}}^H \mathbf{D}_{\mathbf{q}}$ are circulant under periodic boundary conditions on \mathbf{f} (see [72] for example) and hence are diagonalizable in the Fourier domain as

$$\mathbf{D}_{\mathbf{q}}^H \mathbf{D}_{\mathbf{q}} \mathbf{f} = \mathcal{F}^{-1}(|\mathbf{d}_{\mathbf{q}}|^2 \bullet \mathcal{F}(\mathbf{f})), \quad (2.25)$$

where $|\mathbf{d}_{\mathbf{q}}|^2$ is the pointwise modulus squared of the Fourier multiplier $\mathbf{d}_{\mathbf{q}}$ corresponding to $\mathbf{D}_{\mathbf{q}}$. Hence, taking the DFT of both sides of equation (2.23) we have:

$$\left(2\mathbf{a} + \lambda\beta \sum_{\mathbf{q} \in \mathcal{N}} |\mathbf{d}_{\mathbf{q}}|^2 \right) \bullet \mathcal{F}(\mathbf{f}) = 2\mathbf{b}_0 + \lambda\beta \mathcal{F} \left(\sum_{\mathbf{q} \in \mathcal{N}} \mathbf{D}_{\mathbf{q}}^H \mathbf{h}_{\mathbf{q}} \right)$$

where $\mathbf{b}_0 = \mathcal{F}(\mathbf{A}^H \mathbf{b}) \in \mathbb{C}^M$ is a zero-padded version of the Fourier samples $\mathbf{b} \in \mathbb{C}^N$. Solving for \mathbf{f} gives

$$\hat{\mathbf{f}} = \mathcal{F}^{-1} \left[\frac{2\mathbf{b}_0 + \lambda\beta\mathcal{F} \left(\sum_{\mathbf{q} \in \mathcal{N}} \mathbf{D}_{\mathbf{q}}^H \mathbf{h}_{\mathbf{q}} \right)}{2\mathbf{a} + \lambda\beta \sum_{\mathbf{q} \in \mathcal{N}} |\mathbf{d}_{\mathbf{q}}|^2} \right] \quad (2.26)$$

where the division occurs entrywise. Note that we have omitted the iteration step n from the above equation. Strictly speaking, it is an update for $\hat{\mathbf{f}}$, assuming $\mathbf{h}_{\mathbf{q}}$ to be determined from \mathbf{f}_{n-1} . In inverse problems such as non-Cartesian MRI and parallel MRI, where the measurement operator \mathbf{A} is not diagonalizable in the Fourier domain, we solve equation (2.23) efficiently using conjugate gradient (CG) algorithm, as will be shown in the second and third aim. A few CG steps at each iteration are often sufficient for good convergence since the algorithm is initialized by the previous iterate.

2.4.2 Efficient Evaluation of Shrinkage Weights

We now focus on the efficient evaluation of $\mathbf{v}_{\mathbf{q}}(\mathbf{x})$; $\forall \mathbf{q} \in \mathcal{N}$ in (2.15). Note that $\mathbf{u}_{\mathbf{q}}(\mathbf{x})$ involves the comparison of the patches $P_{\mathbf{x}}(\mathbf{f})$ and $P_{\mathbf{x}+\mathbf{q}}(\mathbf{f})$; since these quantities have to be computed for all spatial locations \mathbf{x} and different shifts \mathbf{q} , the direct evaluation of (2.15) is computationally expensive. We propose to exploit the redundancies between $\mathbf{v}_{\mathbf{q}}(\mathbf{x})$ to considerably accelerate their computation. From (2.15), we have

$$\mathbf{u}_{\mathbf{q}}(\mathbf{x}) = \nu \left(\sqrt{\underbrace{\sum_{\mathbf{p} \in \mathcal{B}} \|\mathbf{f}(\mathbf{x} - \mathbf{p}) - \mathbf{f}(\mathbf{x} - \mathbf{p} + \mathbf{q})\|^2}_{(|\mathbf{D}_{\mathbf{q}}\mathbf{f}|^2 * \eta)(\mathbf{x})}} \right). \quad (2.27)$$

Here η is a moving average filter with the size of the patch. The above equation implies that computing $\mathbf{u}_q(\mathbf{x}); \forall \mathbf{x}$ can be obtained efficiently by simple pointwise operations and a computationally efficient convolution operation. Combining the above result with (2.15), we obtain

$$\mathbf{v}_q = \underbrace{\left[\nu \left(\sqrt{|\mathbf{D}_q \mathbf{f}|^2 * \eta} \right) \right]}_{\mathbf{u}_q} * \eta \quad (2.28)$$

We realize the convolutions $|\mathbf{D}_q \mathbf{f}|^2 * \eta$ and $\mathbf{u}_q * \eta$ using separable moving average convolution operations. This approach has some similarities to [73], where moving average filters were used to speed up the non-local means algorithm.

2.4.3 Continuation Strategy to Improve Convergence

The quality of the majorization in equation (2.8) depends on the parameter β . It is known that high values of β results in poor convergence. However, since we require the convex-hull approximation of the original penalty for the majorization, the solution of the proposed scheme corresponds to that of the original problem only when $\beta \rightarrow \infty$. Hence we use a continuation strategy to improve the convergence rate, where β is initialized with a small value and is increased gradually to a high value [4]. As discussed in [4], we use homotopy continuation on the penalties to encourage convergence to global minima. For example, with truncated penalties we start with a large threshold T and gradually decrease it until it attains a small value. In all the experiments, we initialize β to 1e-2 and set $\beta_{\text{incfactor}} = 2$ while we set $T_{\text{defactor}} = 1.1$. The pseudo-code of the algorithm is shown below.

Algorithm 2.4.1: NONLOCAL SHRINKAGE($\mathbf{A}, \mathbf{b}, \lambda$)**Input :** \mathbf{b} = k-space measurements $\beta = \beta_{\text{init}}; T = T_{\text{init}};$ **while** $i < \#$ Outer Iterations
$$\text{do} \left\{ \begin{array}{l} \text{while } j < \# \text{ Inner Iterations} \\ \text{do} \left\{ \begin{array}{l} \text{Shrinkage: Compute } \mathbf{v}_{\mathbf{q}} \text{ using equation (2.15)} \\ \text{Compute } \mathbf{h}_{\mathbf{q}} \text{ using equation (2.14)} \\ \text{Update } \mathbf{f} \text{ using equation (2.26)} \end{array} \right. \\ \beta \leftarrow \beta * \beta_{\text{incfactor}} \\ T \leftarrow T * T_{\text{decfactor}} \end{array} \right.$$
return (\mathbf{f})

We observe that the proposed algorithm is similar in structure to our previous algorithm [4], shown below.

Algorithm 2.4.2: REWEIGHTED MM ($\mathbf{A}, \mathbf{b}, \lambda, \sigma$)**Input :** \mathbf{b} = k-space measurements $T = T_{\text{init}};$ **while** $i < \#$ Outer Iterations
$$\text{do} \left\{ \begin{array}{l} \text{while } j < \# \text{ Inner Iterations} \\ \text{do} \left\{ \begin{array}{l} \text{Update } \mathbf{w}_{\mathbf{x},\mathbf{y}} \text{ using (16) in [4]} \\ \text{Compute } \gamma_{\mathbf{x},\mathbf{y}} \text{ using (20) in [4]} \\ \text{Update } \mathbf{f} \text{ by solving (26) in [4]} \end{array} \right. \\ T \leftarrow T * T_{\text{decfactor}} \end{array} \right.$$
return (\mathbf{f})

Evaluating \mathbf{f} according to [equation (2.26)] requires one FFT and one IFFT. We typically need 10 - 20 inner iterations and about 30 - 40 outer iterations for the best convergence and recovery. All the experiments were performed in MATLAB 2012 on

a Linux Intel Xeon workstation machine with four cores, 3.2 GHz CPU and 32 GB RAM.

2.5 RESULTS

We focus on the application of this scheme for the recovery of MR images from undersampled measurements. All the datasets used in this aim research were acquired on the Siemens 3T Tim Trio scanner at the University of Iowa. The datasets were collected under a protocol approved by the Institutional Review Board (IRB) at the University of Iowa and an informed consent was obtained from the subjects prior to the scan.

2.5.1 Convergence Rate

We first compare the proposed scheme with our previous iterative reweighted non-local algorithm [4]. We considered the recovery of an MR brain image used in Fig. 2.4 from its retrospectively undersampled Fourier measurements using a variable density random sampling pattern (see Fig. 2.4.(e) for an example). The regularization parameters of both algorithms were set to $\lambda = 10^{-4}$; this parameter was chosen to obtain the best possible reconstructions. The number of inner iterations and outer iterations in both the algorithms were set to 5 and 45, respectively. The maximum number of CG iterations to solve each quadratic subproblem in IRW scheme was set to 10. The tolerance values for all loops in both algorithms were set to $1e-8$.

The convergence plots of the two algorithms as functions of computation time and number of iterations are shown in Fig. 2.3. We observe that both algorithms converge to almost the same final cost. However, the non-local shrinkage (NLS) algorithm is around ten times faster than the iterative reweighted (IRW) scheme in terms of computation time; the NLS scheme took around 17 seconds, while the IRW required 172 seconds to converge. All the weight updates in IRW together took a total of 9.4 seconds, while the shrinkage steps in NLS took a total of 12.0 seconds.

The main difference in complexity between the algorithms can be attributed to the analytical solution of f in the NLS scheme, which took only 0.4 seconds for all 225 inner iterations. At the same time, solving the quadratic subproblems in IRW using CG took around 163 seconds for all 225 inner iterations. We observe that the condition number of the quadratic subproblem in iterative reweighting [4] grows with iterations, resulting in slow convergence of the CG algorithms especially in later iterations. The speedup offered by using an additive half-quadratic majorization specified by equation (2.8) is consistent with using this method in non-patch regularization schemes [70].

2.5.2 Impact of the Distance Metric

The proposed scheme can be adapted to most non-local distance metrics by simply changing the shrinkage rule. The shrinkage rules for different non-local penalties are shown in Fig. 2.1. In Table 2.1 we compare the different metrics in the context of recovering three MR images from five fold randomly undersampled data. Here we quantify the reconstruction quality by the signal-to-noise ratio (SNR), defined as

$$\text{SNR} = 20 \log_{10} \left(\frac{\|\mathbf{\Gamma}_{\text{orig}}\|_F}{\|\mathbf{\Gamma}_{\text{rec}} - \mathbf{\Gamma}_{\text{orig}}\|_F} \right),$$

where $\mathbf{\Gamma}_{\text{orig}}$ is the original image, $\mathbf{\Gamma}_{\text{rec}}$ is the recovered image, and $\|\cdot\|_F$ is the Frobenius norm. The parameters of all the algorithms are optimized to provide the best possible SNR. The first column corresponds to the convex ℓ_1 differences between patches. The second and third columns correspond to alternating H1 and NLTV penalties [4], respectively.

All of the penalties saturate with inter-patch distances except the ℓ_1 distance function. This explains the poor performance of the convex ℓ_1 penalty compared to the non-convex counterparts. Unlike local total variation, which only compares a particular pixel with a few other pixels, several pixel comparisons are involved in non-

Table 2.1: (SNR in dB) Impact of the distance metric on the reconstructions. We compare the reconstructions obtained using the non-local shrinkage algorithm using ℓ_1 , H_1 , NLTV, thresholded ℓ_1 and thresholded $\ell_p; p = 0.5$ metrics. All the metrics, except the convex ℓ_1 scheme are saturating priors. We observe that saturation is key to good performance of non-local algorithms. Among the different metrics, the thresholded ℓ_p penalty is observed to provide the best results in all the examples.

| Image | ℓ_1 | H_1 | NLTV | ℓ_1 -T | ℓ_p -T |
|--------|----------|-------|------|-------------|-------------|
| Brain1 | 19.8 | 22.8 | 23.0 | 21.4 | 23.4 |
| Brain2 | 18.0 | 20.2 | 21.1 | 19.5 | 22.9 |
| Head | 19.1 | 19.2 | 19.5 | 19.3 | 19.9 |

local regularization. Saturating priors are needed to avoid the averaging of dissimilar patches, which may result in blurring. Since the saturating ℓ_p metric provides the best overall reconstructions, we use this prior for remaining comparisons.

2.5.3 Comparisons With State-of-the-Art Algorithms

We compare the proposed scheme with local total variation regularization (TV) and the dictionary learning MRI (DLMRI) scheme [1] using retrospectively under-sampled MRI data. Specifically, the Fourier samples of the images on the specified sampling mask are used for reconstruction using different algorithms. These reconstructions are compared to the original image. We relied on the MATLAB implementation of DLMRI available from the authors webpage, which was adapted to account for complex MR images. The regularization parameters of all the algorithms have been optimized to yield the best SNR. The comparison of the above methods in the context of random sampling with 5 fold undersampled data in the absence of noise is shown in Fig. 2.4. This fully sampled 128×128 MR brain image was acquired using a Turbo spin echo (TSE) sequence, FOV= 22×22 cm², slice thickness=5.0 mm. The under sampling pattern in (e) was generated using a Monte-Carlo algorithm [74], which may be realized in 3D imaging by choosing the readout to be orthogonal to the image plane. We observe that the proposed non-local algorithm provides better

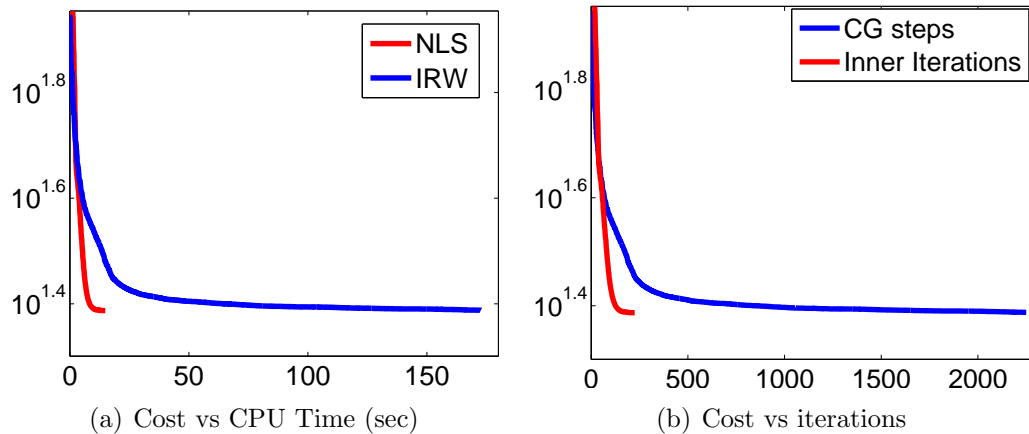


Figure 2.3: Comparison of the convergence rate of the iterative reweighted (IRW) algorithm and the proposed iterative non-local shrinkage (NLS) algorithm. The plots indicate the evolution of the cost function in [equation (2.2)] as functions of (a) the CPU time and (b) number of inner iterations in NLS and CG steps in IRW. Both NLS and IRW algorithms converged in around 225 inner iterations. However, the IRW scheme needed around 9 CG steps/inner iteration on average, requiring a total of 2200 (see Algorithms IV.1 and IV.2). Since each inner iteration in NLS is considerably faster than the corresponding one in [4], we obtain a speedup of approximately ten fold.

preservation of edge details. The quantitative comparisons of different methods on the retrospective under sampling of more MR images in the absence of noise and five fold random undersampling are reported in Table 2.2. We observe that NLS provides a consistent 1-4 dB improvement over other state-of-the-art methods.

Table 2.2: (SNR in dB) Quantitative comparison of the proposed iterative non-local shrinkage (NLS) algorithm using the saturating $\ell_p; p = 0.5$ penalty with dictionary learning MRI (DLMRI) [1] and local total variation regularization (TV) schemes in the absence of noise. We considered five-fold random undersampling.

| Image | DLMRI | TV | NLS |
|--------|-------|------|-------------|
| Brain | 16.6 | 19.3 | 23.4 |
| Brain2 | 17.5 | 21.0 | 22.9 |
| Thigh | 16.3 | 22.0 | 24.0 |
| Calf | 19.1 | 21.2 | 22.5 |
| Head | 18.6 | 19.6 | 19.9 |

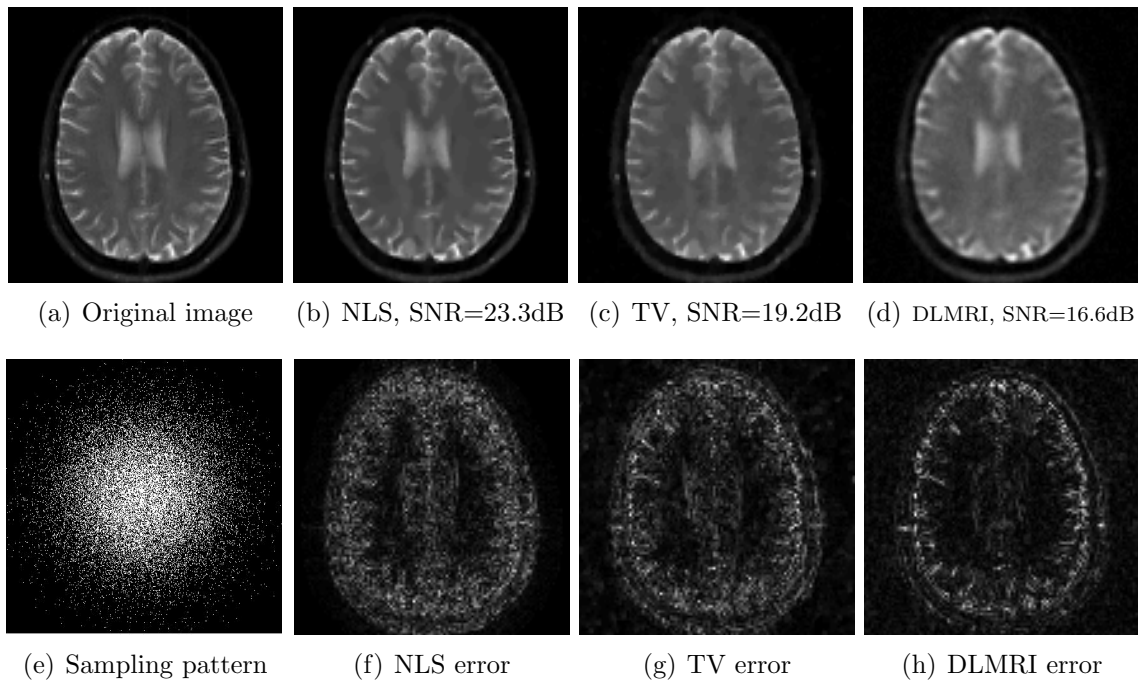


Figure 2.4: Comparison of the algorithms in the absence of noise. We consider the recovery of a 128×128 MR brain image from 5 fold undersampled Fourier samples, acquired using a random sampling pattern shown in (e) using non-local shrinkage scheme (NLS), DLMRI and local TV. The reconstructions are shown in (b)-(d). The corresponding error images, scaled by a factor of 5 for better visualization, are shown in the bottom row. The reconstructions show that the NLS scheme is capable of better preserving the edges and details, resulting in less blurred reconstructions. Note that this example was used as an illustration; the proposed 2-D under sampling pattern on the dataset acquired using a 3-D sequence is not very realistic. We also used a high acceleration factor to demonstrate differences between the methods; thus the resulting images may not be of diagnostic quality.

2.5.4 Performance With Noise

We study the performance of the proposed algorithm in the context of recovering MR images from their retrospectively undersampled measurements using different sampling trajectories in the presence of noise. The reconstructions of 512×512 MR head complex image from its three-fold Cartesian retrospectively undersampled Fourier data, corrupted with zero mean complex Gaussian noise are shown in Fig. 2.5. The SNR of the noisy measurements was 25.0 dB. This is a really challenging case since the 1-D downsampling pattern is considerably less efficient than 2-D random sampling. We observe that the non-local algorithm provides better reconstructions

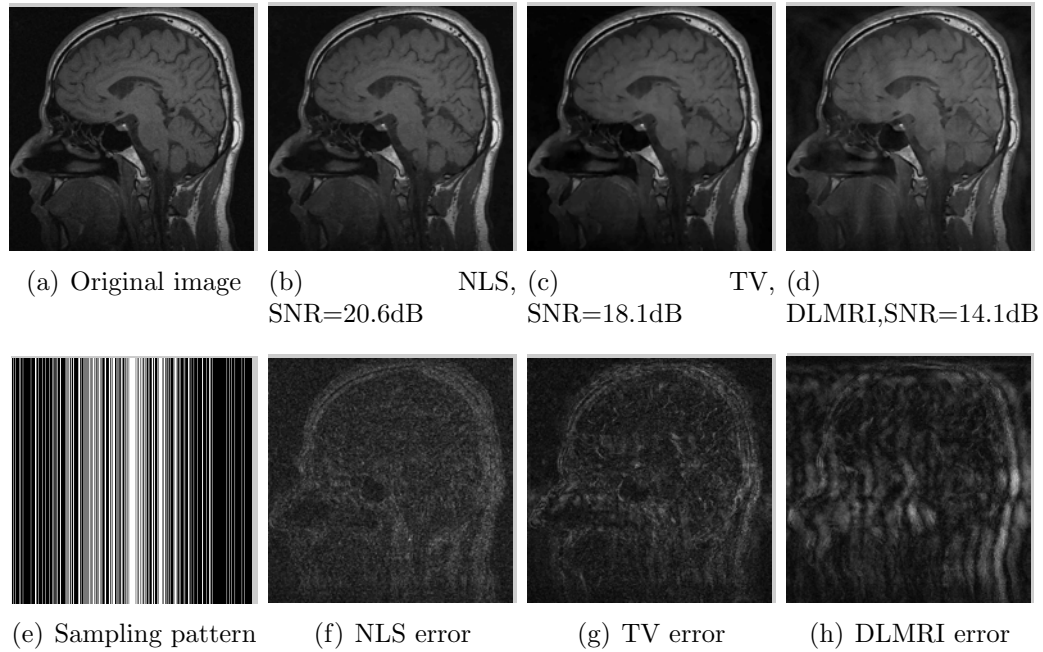


Figure 2.5: Comparison of the algorithms in the presence of noise. We consider the recovery of a 512×512 MR head complex image from three-fold undersampled k-space data, acquired using a Cartesian sampling pattern contaminated by zero mean complex Gaussian such that the SNR value after adding the noise is 25.0 dB. The top row shows the original and reconstructed images using non-local shrinkage scheme (NLS), DLMRI and local TV. The reconstructions are shown in (b)-(d). The corresponding error images as well as the sampling pattern are shown in the bottom row. This is a challenging case due to the high 1-D undersampling factors and noise. We observe that the NLS scheme provides better reconstructions with minimal aliasing artifacts. Note that this example was used as an illustration; the proposed 2-D under sampling pattern on the dataset acquired using a 3-D spin-echo sequence is not very realistic. Note that we used a high acceleration factor to demonstrate differences between the methods. The resulting images may not be of diagnostic quality.

than the other schemes. Specifically, the TV scheme results in patchy artifacts and are over-smoothed. The DLMRI results in blurring and loss of details. By contrast to the classical algorithms, the degradation in performance of the non-local algorithm is comparatively small. The quantitative comparisons of the algorithms on this setting using different MR images are shown in the top section of Table 2.3.

We also consider the recovery of five various MR images from their pseudo-radial samples acquired with 70 spokes/frame, which approximately corresponds to an acceleration factor of 4.2. The radial samples are approximated by the nearest Cartesian samples. The quantitative results in this setting for those MR images are shown in the bottom section of Table 2.3. The Fourier measurements are corrupted with zero mean complex Gaussian noise of a specific variance. The SNR of the corresponding k-space measurements is reported in the second column. All methods are observed to result in loss of subtle image features since the acceleration factor and the noise level are high. But we also observe that the NLS scheme provides better recovery than the competing methods. The SNR improvement offered by NLS over the other methods in this experiment is not as high as in the previous cases, mainly due to the considerable noise in the data and the high acceleration. All of the above experiments were conducted at high acceleration factors to demonstrate the performance improvement offered by the proposed scheme. We show in Fig. 2.6 the recovery of three MR images from Fourier samples corresponding to low accelerations, contaminated with zero mean complex Gaussian noise. These experiments show that the NLS scheme can be used to obtain good quality reconstructions at moderate acceleration factors and noise levels.

2.5.5 Validation using non-Cartesian MRI data

We consider the recovery of multichannel multi-shot spiral MRI data using the proposed scheme and TV regularization in this subsection. These datasets were acquired using a spin-echo variable density multi shot spiral acquisition with 22 interleaves,

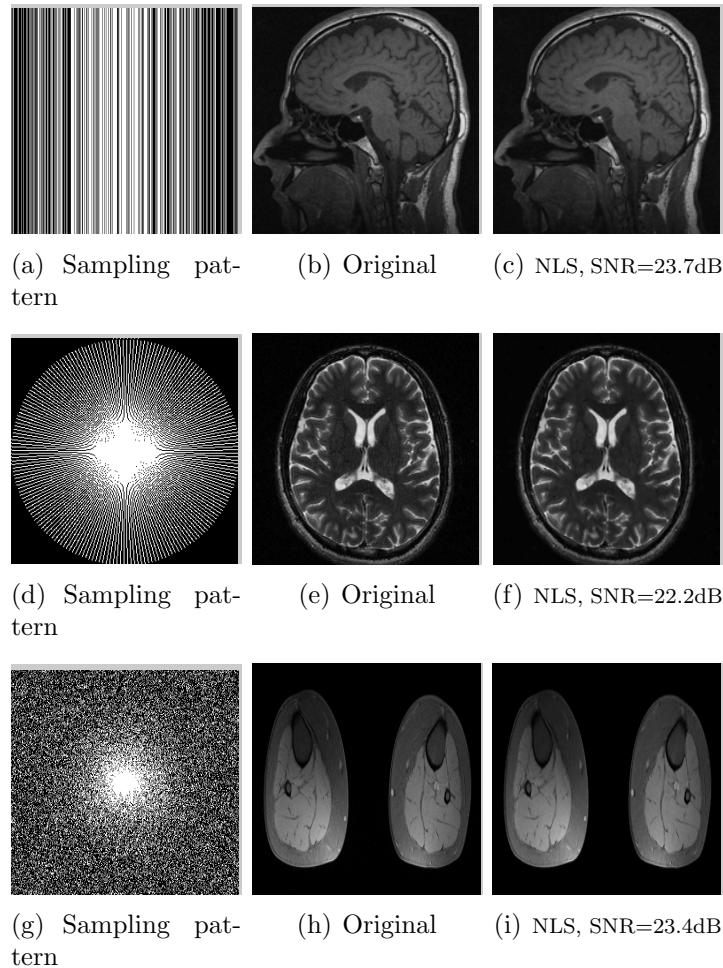


Figure 2.6: Comparison of three different MR images using NLS scheme in the presence of noise. The Fourier samples are contaminated by zero mean complex Gaussian noise such that the SNR of the data corresponding to the head, brain2 and calf images are 32.3, 24.7 and 27.6 dB, respectively. The top row shows the recovery from 2 fold acceleration using the Cartesian sampling pattern, while the middle one shows the recovery from 100 radial spokes (≈ 3 fold acceleration). The bottom row shows the recovery from 3 fold acceleration using random pattern. We observe that the NLS scheme is capable of preserving the key image details.

192×192 matrix and a 12 channel head array. The fully sampled dataset is recovered from all 22 interleaves and four of the important coils using total variation regularization. Specifically, each of the channels were reconstructed independently from the measured k-space data and the coil sensitivities were estimated from them. These coil sensitivities were used to recover the images from undersampled data. The forward and backward models are implemented using the non-uniform fast Fourier transform (NUFFT) [75, 76]. Since the forward model is a non-Cartesian Fourier transform, we are no longer able to use the analytical solution (2.26). We instead use the conjugate gradient algorithm (CG) to solve (2.23). We set the maximum number of CG iterations to 20 and the the previous iterate was set as the the initial guess. We observe that very few CG iterations (average of 3-4) are needed in each inner iteration, thanks to the good conditioning of (2.23), especially at later iterations.

The undersampled data was recovered from the measured k-space data corresponding to a random subset of 7 interleaves of the above four channels. We re-

Table 2.3: Quantitative comparison of the algorithms in the presence of noise. The top part shows the SNR of the reconstructions obtained from 3 fold Cartesian undersampled data. The bottom part shows the SNR of the reconstructions from radial undersampled data with 70 spokes. Both experiments are contaminated by zero mean complex Gaussian noise such that the SNR of the noisy images are reported in the table. The quantitative results show that the proposed iterative NLS scheme provides consistently better reconstructions for the above cases.

| Image | k-space SNR | DLMRI | TV | NLS |
|---------------|-------------|-------|-------------|-------------|
| Brain | 12.9 | 13.9 | 15.0 | 16.8 |
| Brain2 | 11.7 | 15.9 | 16.1 | 18.5 |
| Thigh | 10.7 | 12.6 | 18.7 | 21.7 |
| Calf | 12.6 | 15.9 | 18.5 | 20.6 |
| Head | 11.0 | 14.1 | 18.1 | 20.3 |
| Brain | 11.6 | 14.6 | 17.6 | 17.3 |
| Brain2 | 15.4 | 17.0 | 17.7 | 18.0 |
| Thigh | 12.4 | 13.8 | 17.2 | 20.0 |
| Calf | 8.3 | 9.3 | 16.7 | 19.0 |
| Head | 13.4 | 17.9 | 18.1 | 18.2 |

covered the images using the different algorithms. The forward model in this case is the non-Cartesian Fourier transform of the coil sensitivity weighted images, using the coil sensitivities estimated from fully sampled data¹. We use the CG algorithm with the same settings as above to solve (2.23). We did not use any pre-conditioners in the present study; we expect to further reduce the computational complexity in the future using efficient preconditioners. We only compare our recovery against TV as it was difficult to modify the DLMRI scheme to the non-Cartesian setting. We show the acquisition from two subjects in Fig. 2.7. The trajectories corresponding to the datasets are shown in the first column. The data from the second subject (bottom slice) had considerable off-resonance losses since the slice was close to the frontal sinuses and the ear regions. In addition, it also suffered from inter-shot motion that resulted in inconsistencies between the interleaves. The comparisons clearly show the benefit of the proposed scheme in a practical setting. Specifically, the NLS reconstructions preserve fine details better than TV regularization.

2.6 DISCUSSION AND CONCLUSION

In this chapter we introduced a fast iterative non-local shrinkage algorithm to recover MR image data from undersampled Fourier measurements. This approach is enabled by the reformulation of current non-local schemes as an iterative re-weighting algorithm to minimize a global criterion [4]. The proposed algorithm alternates between a non-local shrinkage step and a quadratic subproblem, which can be solved analytically and efficiently. We derived analytical shrinkage rules for several penalties that are relevant in non-local regularization. We accelerated the non-local shrinkage step, whose direct evaluation involves expensive non-local patch comparisons, by exploiting the redundancy between the terms at adjacent pixels. The resulting algorithm is observed to be considerably faster than our previous implementation. The com-

¹This is justified since many methods such as fMRI can acquire fully sampled anatomical images, while the functional data needs to be acquired rapidly.

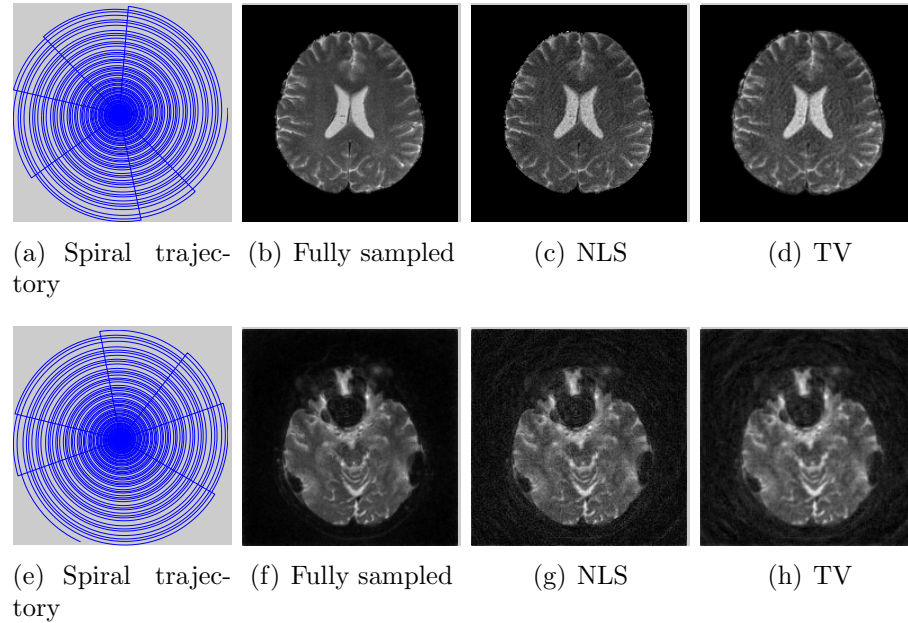


Figure 2.7: Comparison of MR brain images using NLS and TV algorithms from undersampled multichannel multi-shot spiral data. The fully sampled data was acquired using a multishot spiral sequence with 22 interleaves acquired using 12 channels. All the interleaves were used to recover the fully sampled datasets, while only 7 randomly chosen interleaves were used to recover the undersampled datasets. The retained interleaves are shown in the first column. We only used the data corresponding to four important coils for the recovery. The two rows corresponds to two slices in the acquisition. The recovery of the lower slice was considerably challenging due to field inhomogeneity losses and subtle physiological motion between interleaves; this explains the poor recovery of the datasets. The two rows show the spiral trajectory, original and reconstructed images. Both the proposed and TV regularized reconstructions are seen to have lower SNR, mainly due to decreased number of measurements. However, we observe that the proposed scheme provides sharper reconstructions.

parison of different penalties demonstrated the benefit in using distance functions that saturate with distant patches. The comparisons of the proposed scheme with state-of-the-art algorithms show a considerable reduction in alias artifacts and better preservation of edges.

2.7 Appendix A: Simplification of Eq (2.11)

Using the formula for the shrinkage from (3.10), specified by

$$\mathbf{s}_{\mathbf{x},\mathbf{q}} = (P_{\mathbf{x}}(\mathbf{f}) - P_{\mathbf{x}+\mathbf{q}}(\mathbf{f})) \nu (\|P_{\mathbf{x}}(\mathbf{f}) - P_{\mathbf{x}+\mathbf{q}}(\mathbf{f})\|),$$

we obtain

$$\mathcal{R}(\mathbf{f}) = \sum_{\mathbf{x};\mathbf{q}\in\mathcal{N}} \|P_{\mathbf{x}}(\mathbf{f}) - P_{\mathbf{x}+\mathbf{q}}(\mathbf{f}) - \mathbf{s}_{\mathbf{x},\mathbf{q}}\|^2. \quad (2.29)$$

Expanding the above expression:

$$\mathcal{R}(\mathbf{f}) = \sum_{\mathbf{x};\mathbf{q}\in\mathcal{N}} \sum_{\mathbf{p}\in\mathcal{B}} |f(\mathbf{x} + \mathbf{p}) - f(\mathbf{x} + \mathbf{q} + \mathbf{p}) - \mathbf{s}_{\mathbf{x},\mathbf{q}}(\mathbf{p})|^2 \quad (2.30)$$

We use a change of variables $\mathbf{x} = \mathbf{x} + \mathbf{p}$ to obtain:

$$\begin{aligned} \mathcal{R}(\mathbf{f}) &= \sum_{\mathbf{x};\mathbf{q}\in\mathcal{N}} \sum_{\mathbf{p}\in\mathcal{B}} \overbrace{|f(\mathbf{x}) - f(\mathbf{x} + \mathbf{q}) - \mathbf{s}_{\mathbf{x}-\mathbf{p},\mathbf{q}}(\mathbf{p})|^2}^{e(\mathbf{x},\mathbf{q})} \\ &= \sum_{\mathbf{x};\mathbf{q}\in\mathcal{N}} |e(\mathbf{x}, \mathbf{q})|^2 - 2 \sum_{\mathbf{x};\mathbf{q}\in\mathcal{N}} e(\mathbf{x}, \mathbf{q}) \underbrace{\sum_{\mathbf{p}\in\mathcal{B}} \mathbf{s}_{\mathbf{x}-\mathbf{p},\mathbf{q}}(\mathbf{p})}_ {h_{\mathbf{q}}(\mathbf{x})} + c \\ &= \sum_{\mathbf{x};\mathbf{q}\in\mathcal{N}} |f(\mathbf{x}) - f(\mathbf{x} + \mathbf{q}) - h_{\mathbf{q}}(\mathbf{x})|^2 + c - d. \end{aligned} \quad (2.31)$$

In the above equations, $c = \sum_{\mathbf{x};\mathbf{q}\in\mathcal{N};\mathbf{p}\in\mathcal{B}} |\mathbf{s}_{\mathbf{x}-\mathbf{p},\mathbf{q}}(\mathbf{p})|^2$ and $d = \sum_{\mathbf{x};\mathbf{q}\in\mathcal{N}} |h_{\mathbf{q}}(\mathbf{x})|^2$. Since the solution to (2.11) does not depend on the constants, we ignore these terms. Thus,

(2.30) can be rewritten using (2.31) as

$$\mathcal{R}(f) = \sum_{\mathbf{x}; \mathbf{q} \in \mathcal{N}} \left\| \underbrace{f(\mathbf{x}) - f(\mathbf{x} + \mathbf{q})}_{\mathcal{D}_{\mathbf{q}}f} - h_{\mathbf{q}}(\mathbf{x}) \right\|^2$$

Here, $\mathcal{D}_{\mathbf{q}}f(\mathbf{x}) = f(\mathbf{x} + \mathbf{q}) - f(\mathbf{x})$ is the finite difference operator. We observe that the expression for $h_{\mathbf{q}}(\mathbf{x})$

$$h_{\mathbf{q}}(\mathbf{x}) = \sum_{\mathbf{p} \in \mathcal{B}} \mathbf{s}_{\mathbf{x}-\mathbf{p}, \mathbf{q}}(\mathbf{p}), \quad (2.32)$$

can be further simplified. From (3.10), we have the patch \mathbf{s} specified as

$$\mathbf{s}_{\mathbf{x}, \mathbf{q}} = (P_{\mathbf{x}}f - P_{\mathbf{x}+\mathbf{q}}f) \underbrace{\nu(\|P_{\mathbf{x}}f - P_{\mathbf{x}+\mathbf{q}}f\|)}_{u_{\mathbf{q}}(\mathbf{x})}$$

Here, $u_{\mathbf{q}}(\mathbf{x}) = \nu(\|P_{\mathbf{x}}f - P_{\mathbf{x}+\mathbf{q}}f\|)$ is the factor between 0 and 1, which is multiplied by the patch to get the shrunk patch. Hence,

$$\mathbf{s}_{\mathbf{x}, \mathbf{q}}(\mathbf{r}) = [f(\mathbf{x} + \mathbf{r}) - f(\mathbf{x} + \mathbf{q} + \mathbf{r})] \cdot u_{\mathbf{q}}(\mathbf{x}); \quad \mathbf{r} \in \mathcal{B}.$$

Thus, we have

$$\mathbf{s}_{\mathbf{x}-\mathbf{p}, \mathbf{q}}(\mathbf{p}) = [f(\mathbf{x}) - f(\mathbf{x} + \mathbf{q})] u_{\mathbf{q}}(\mathbf{x} - \mathbf{p}). \quad (2.33)$$

Substituting in (3.13), we get

$$h_{\mathbf{q}}(\mathbf{x}) = (f(\mathbf{x}) - f(\mathbf{x} + \mathbf{q})) \underbrace{\sum_{\mathbf{p} \in \mathcal{B}} u_{\mathbf{q}}(\mathbf{x} - \mathbf{p})}_{v_{\mathbf{q}}(\mathbf{x})}. \quad (2.34)$$

2.8 Appendix B: Shrinkage rules for useful non-local distance functions

2.8.0.1 Thresholded $\ell_p; p \leq 1$ metric

We now consider the saturating ℓ_p metric, specified by

$$\phi(t) = \begin{cases} |t|^p/p & \text{if } |t| < T \\ T^p/p & \text{else} \end{cases} \quad (2.35)$$

Computing the shrinkage rule for this mapping according to (2.22), we obtain

$$\nu(t) = \begin{cases} 0 & \text{if } |t| < \beta^{1/(p-2)} \\ 1 - \frac{1}{\beta}|t|^{p-2} & \text{if } \beta^{1/(p-2)} \leq |t| < T \\ 1 & \text{else} \end{cases} \quad (2.36)$$

Setting $T = \infty$ we get the shrinkage rule for the unthresholded ℓ_p metric as

$$\nu(t) = \begin{cases} 0 & \text{if } |t| < \beta^{1/(p-2)} \\ 1 - \frac{1}{\beta}|t|^{p-2} & \text{else} \end{cases}, \quad (2.37)$$

which is consistent with [3].

2.8.0.2 Penalty corresponding to alternating H_1 non-local scheme

We now consider the H_1 metric, specified by

$$\varphi(t) = 1 - \exp\left(-\frac{t^2}{2\sigma^2}\right). \quad (2.38)$$

From (2.22) we obtain

$$\nu(t) = \begin{cases} 0 & \text{if } \exp\left(-\frac{t^2}{2\sigma^2}\right) > \beta\sigma^2 \\ 1 - \frac{\exp\left(-\frac{t^2}{2\sigma^2}\right)}{\beta\sigma^2} & \text{else} \end{cases} \quad (2.39)$$

2.8.0.3 Penalty corresponding to Peyre's non-local scheme

We now consider the penalty corresponding to Peyre's alternating scheme [4,77]:

$$\phi(t) = 1 - \exp\left(-\frac{t}{\sigma}\right). \quad (2.40)$$

From (2.22) we obtain

$$\nu(t) = \begin{cases} 0 & \text{if } \exp\left(-\frac{t}{\sigma}\right) > \beta\sigma t \\ 1 - \frac{\exp\left(-\frac{t}{\sigma}\right)}{\beta\sigma t} & \text{else} \end{cases} \quad (2.41)$$

2.8.0.4 Penalty corresponding to alternating non-local TV scheme

The penalty function for the alternating non-local TV scheme is specified by [4,78]:

$$\phi(t) = \operatorname{erf}\left(\frac{t}{\sigma}\right). \quad (2.42)$$

From (2.22) we obtain

$$\nu(t) = \begin{cases} 0 & \text{if } \frac{2}{\sqrt{\pi}} \exp\left(-\frac{t^2}{\sigma^2}\right) > \beta\sigma t \\ 1 - \frac{2}{\sqrt{\pi}} \frac{\exp\left(-\frac{t^2}{\sigma^2}\right)}{\beta\sigma t} & \text{else} \end{cases} \quad (2.43)$$

CHAPTER 3

ACCELERATED MRI USING PATCH REGULARIZATION FOR IMPLICIT MOTION COMPENSATION

3.1 ABSTRACT

An efficient patch smoothness regularization scheme, which implicitly compensates for inter-frame motion, is introduced to recover dynamic MRI data from highly undersampled measurements. The regularization prior is a sum of distances between each rectangular patch in the dataset with other patches in the dataset using a saturating distance metric. Unlike current motion estimation and motion compensation (ME-MC) methods, the proposed scheme does not require reference frames or complex motion models. The proposed algorithm, which alternates between inter-patch shrinkage step and conjugate gradient algorithm, is considerably more computationally efficient than ME-MC methods. The reconstructions obtained using the proposed algorithm is compared against state-of-the-art methods. The proposed method is observed to yield reconstructions with minimal spatiotemporal blurring and motion artifacts. In comparison to the existing state-of-the-art ME-MC methods, PRICE provides comparable or even better image quality with faster reconstruction times (approximately nine times faster). The presented scheme enables computationally efficient and effective motion-compensated reconstruction in a variety of applications with large inter-frame motion and contrast changes. This algorithm could be seen as an alternative over the current state-of-the-art ME-MC schemes that are computationally expensive.

3.2 THEORY

3.2.1 Dynamic MRI: Model Of The Acquisition Scheme

The multi-coil undersampled acquisition of the dynamic MRI dataset $\mathbf{f}(x, y, t) : \mathbb{Z}^3 \rightarrow \mathbb{C}$ can be modeled as:

$$\mathbf{b}_i(k_x, k_y, t) = \int_{x,y} \mathbf{f}(x, y, t) s_i(x, y) e^{j(k_x x + k_y y)} dx dy + \mathbf{n}(k_x, k_y, t). \quad (3.1)$$

Here, $\mathbf{b}(k_x, k_y, t)$ represents the k-space measurements from all the coils, while $\mathbf{f}(x, y, t)$ is the dynamic dataset, and $s_i(x, y)$ denotes the i^{th} coil sensitivity pattern. We assume \mathbf{n} to be a complex zero mean Gaussian distributed white noise process of a specified standard deviation σ . The above relations can be compactly expressed in the vector form as

$$\mathbf{b} = \mathbf{A}\mathbf{f} + \mathbf{n}, \quad (3.2)$$

where \mathbf{A} is the forward model. From now on, we will consider the dynamic dataset \mathbf{f} as a 3-D volume indexed by the variable $\mathbf{r} = (x, y, t)$.

3.2.2 Implicit Motion Compensation Using Patch Regularization

Unlike the cost function in equation (2.2) mentioned in chapter 2 where \mathbf{f} is a 2D matrix, and \mathbf{A} is single channel undersampling operator, here we propose to recover the dynamic dataset \mathbf{f} from its undersampled measurements as the patch regularized optimization problem as:

$$\hat{\mathbf{f}} = \arg \min_{\mathbf{f}} \underbrace{\|\mathbf{A}\mathbf{f} - \mathbf{b}\|^2}_{\mathcal{C}(\mathbf{f})} + \lambda \mathcal{G}(\mathbf{f}), \quad (3.3)$$

The regularization penalty $\mathcal{G}(\mathbf{f})$ is the sum of robust distances between patches:

$$\mathcal{G}(\mathbf{f}) = \sum_{\mathbf{r}} \sum_{\mathbf{q} \in \mathcal{N}} \varphi(\|P_{\mathbf{r}}(\mathbf{f}) - P_{\mathbf{r}+\mathbf{q}}(\mathbf{f})\|_{\ell_2}). \quad (3.4)$$

Like the patches extracted in chapter 2, here $P_{\mathbf{r}}(\mathbf{f})$ is a patch extraction operator, which extracts a square shaped 2-D image patch of dimension $(N+1) \times (N+1) \times 1$, centered at the spatial location \mathbf{r} from the dynamic dataset $\mathbf{f}(\mathbf{r})$:

$$P_{\mathbf{r}}(\mathbf{f}) = \mathbf{f}(\mathbf{r} + \mathbf{p}), \quad \mathbf{p} \in \mathcal{B}. \quad (3.5)$$

Here, $\mathcal{B} = [-N/2, ..N/2] \times [-N/2, ..N/2] \times 1$ is the set of indices of the patch. Note from equation (3.3) that we compare each patch $P_{\mathbf{r}}(\mathbf{f})$ in the dataset with other patches $P_{\mathbf{r}+\mathbf{q}}(\mathbf{f})$ in a cube-shaped neighborhood $\mathcal{N} \in [-M/2, ..M/2] \times [-M/2, ..M/2] \times [-M/2, ..M/2]$ around

\mathbf{r} (see Fig 3.1.a). Even though it is fixed in our study, the size of the neighborhood may be chosen depending on the severity of inter-frame motion. Specifically, the size of the search neighborhood (M) may need to be increased in high-resolution datasets or datasets with high inter-frame motion such as dynamic free-breathing lung MRI where there is a considerably large amount of cardiorespiratory motion. While the formulation equation (3.3) has similarities to block matching used in k-t FOCUSS with ME-MC [50], the distinguishing aspect is a unifying cost function that captures both motion estimation and compensation.

The comparisons of each patch with its neighbors are performed using the distance metric φ . While convex ℓ_1 metrics could be chosen, our comparisons in the first aim show that the thresholded ℓ_p , $0 < p < 1$, metric

$$\varphi(t) = \begin{cases} |t|^p/p & \text{if } t < T \\ T^p/p & \text{if } t \geq T. \end{cases} \quad (3.6)$$

provides the best reconstruction with 2-4 db gain over $p = 1$ without thresholding [2]. Compared to convex penalties, the proposed saturating priors (see dotted curve in Fig 3.1.b) minimizes the averaging of dissimilar patches, thus resulting in less blurred reconstructions. For example, while a patch pair with difference greater than T will still contribute to a constant term of T^p/p in the cost, a small shrinkage of these inter-patch distances will not reduce the cost. This behavior translates to patch differences above T not being shrunk at each iteration as seen from equation (3.10) (see also Fig 3.1.c). By contrast, a non-saturating ℓ_1 penalty shrinks all patch differences, irrespective of the size of differences, resulting in blurring.

3.2.3 Iterative Patch Shrinkage Algorithm

We use the majorization of the patch regularization penalty $\mathcal{G}(\mathbf{f})$ to develop an iterative patch shrinkage algorithm to solve equation (3.3). Approximating the distance metric in equation (3.6) (dotted line in Fig 3.1.b) by its smoothed Huber-like versions, we rewrite the

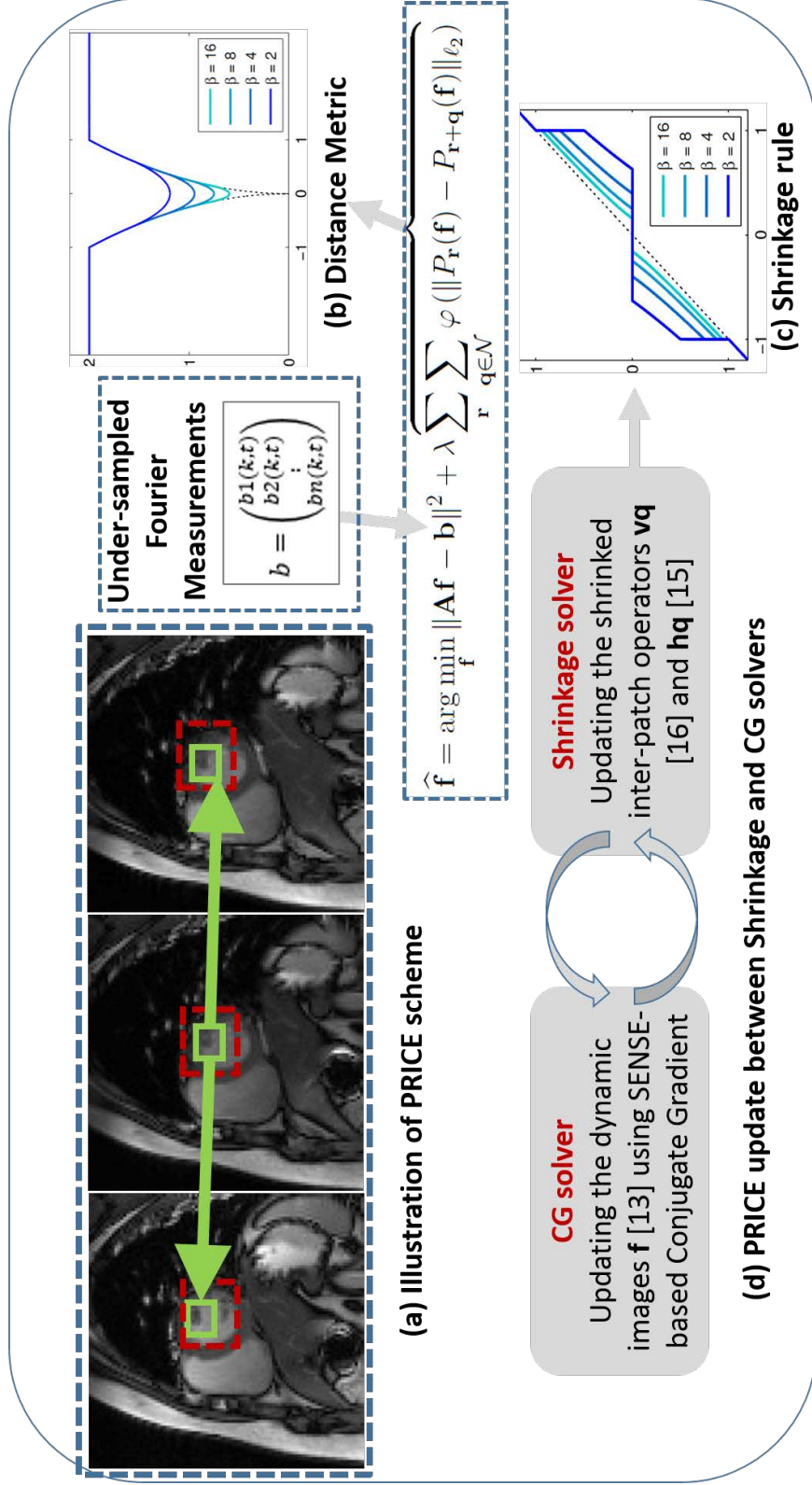


Figure 3.1: (a) Illustration of the proposed PRICE scheme. The regularization term penalizes the differences between each patch and other patches in its cube shaped neighborhood. The green squares indicate the location of the patch in the current frame and the ones with the highest similarity in the neighboring frames. The dashed red box represents the neighborhood where the patches move within. The ability of the algorithm to exploit the similarity between corresponding patches enables it to provide implicit motion compensated recovery unlike the traditional ME-MC methods which explicitly do that. The distance metric used for the comparison is shown by the dotted black curve in (b). The metric heavily penalizes the distances between similar patches, while it saturates for large inter-patch distances. This saturating behavior enables the algorithm to minimize spatiotemporal blurring, resulting from averaging of dissimilar patches. The colored curves correspond to the different approximations of the distance metric, which enables fast algorithms. (c) The shrinkage rule for the inter-patch differences $t \cdot \nu(t)$ using ℓ_p . We rely on continuation schemes as shown in (b) and (c) starting with low values of β and gradually increase it to high values, when the approximation is more accurate. (d) The algorithm alternates between a simple shrinkage step to denoise inter-patch differences and image update step, which involves a computationally efficient conjugate gradients algorithm.

cost function with the approximated penalties as:

$$\mathcal{C}_\beta(\mathbf{f}) = \min_{\{\mathbf{s}_{\mathbf{r},\mathbf{q}}\}} \|\mathbf{A}\mathbf{f} - \mathbf{b}\|^2 + \lambda \sum_{\mathbf{r}} \sum_{\mathbf{q} \in \mathcal{N}} \psi_\beta(\|\mathbf{s}_{\mathbf{r},\mathbf{q}}\|) + \frac{\lambda\beta}{2} \sum_{\mathbf{r},\mathbf{q}} \|P_{\mathbf{r}}(\mathbf{f}) - P_{\mathbf{r}+\mathbf{q}}(\mathbf{f}) - \mathbf{s}_{\mathbf{r},\mathbf{q}}\|^2. \quad (3.7)$$

Here, $\mathbf{s}_{\mathbf{r},\mathbf{q}}$ is an auxiliary variable, which can be interpreted as a denoised version of the inter-patch difference $(P_{\mathbf{r}}(\mathbf{f}) - P_{\mathbf{r}+\mathbf{q}}(\mathbf{f}))$. The above simplification is enabled by the half quadratic majorization of φ [19, 20, 70, 79]:

$$\varphi(t) = \min_s \left\{ \psi_\beta(s) + \frac{\beta}{2}(s-t)^2 \right\}. \quad (3.8)$$

The above majorization rule can be rewritten as:

$$\underbrace{\frac{t^2}{2} - \frac{1}{\beta} \varphi(t)}_{r(t)} = \max_s \left\{ s t - \underbrace{\left(\frac{1}{\beta} \psi_\beta(s) + \frac{s^2}{2} \right)}_{g(s)} \right\} \quad (3.9)$$

From the theory in [71], the above relation is satisfied when $g = r^*$, the Legendre-Fenchel dual of r , specified by $r^*(s) = \max_t \{s t - r(t)\}$. Thus, we obtain $\psi_\beta(s) = \beta (r^*(s) - s^2/2)$. When r is not convex, we approximate it by the closest convex function of r ; see [2] for details.

We use an alternating minimization algorithm to recover \mathbf{f} as well as the denoised inter-patch differences $\mathbf{s}_{\mathbf{r},\mathbf{q}}$ from multi-coil undersampled $k-t$ measurements. We observe that the reformulation in equation (3.7) is remarkably similar to variable splitting; the only difference is that $\psi_\beta = \varphi$ in the variable splitting formulation. If variable splitting strategy were used, one would be able to speed up the algorithm using alternating direction method of multipliers (ADMM). However, a challenge with ADMM schemes is the lack of monotonic convergence. While it is acceptable with convex cost functions, it may result in issues of convergence to local minima when non-convex distance metrics such as equation (3.6) are used. The monotonic convergence guaranteed by majorize-minimize framework is desirable in this setting. We also introduce continuation strategies to minimize the risk of local minima.

Step 1: Determination of denoised inter-patch differences $\mathbf{s}_{\mathbf{r},\mathbf{q}}$: When the variable \mathbf{f} is a constant, the determination of the auxiliary variables $\mathbf{s}_{\mathbf{r},\mathbf{q}}$ corresponding to different values of \mathbf{r} and \mathbf{q} can be decoupled. Specifically, the recovery of a specific patch $\hat{\mathbf{s}}_{\mathbf{r},\mathbf{q}}$ simplifies to a shrinkage step similar to soft thresholding:

$$\hat{\mathbf{s}}_{\mathbf{r},\mathbf{q}} = [P_{\mathbf{r}}(\mathbf{f}) - P_{\mathbf{r}+\mathbf{q}}(\mathbf{f})] \nu(\|P_{\mathbf{r}}(\mathbf{f}) - P_{\mathbf{r}+\mathbf{q}}(\mathbf{f})\|). \quad (3.10)$$

The shrinkage rules for a variety of distance metrics are specified in [2]. For example, when φ is the thresholded ℓ^p metric equation (3.6), we have

$$\nu(t) = \begin{cases} 0 & \text{if } |t| < \beta^{1/(p-2)} \\ 1 - \frac{1}{\beta}|t|^{p-2} & \text{if } \beta^{1/(p-2)} \leq |t| < T \\ 1 & \text{else.} \end{cases} \quad (3.11)$$

Note from equation (3.10) and equation (3.11) that the smaller inter-patch differences are set to zero or shrunk, while the large inter-patch differences are preserved. The shrinkage rule is illustrated in Fig 3.1.c.

Step 2: Determination of the dataset f : If we assume the auxiliary variables $\mathbf{s}_{\mathbf{r},\mathbf{q}}$ to be fixed, the minimization of equation (3.7) with respect to f simplifies to a quadratic subproblem. Combining the terms from adjacent patches for computational efficiency (see Appendix of [2] for details), we simplify this subproblem as:

$$\hat{\mathbf{f}} = \arg \min_{\mathbf{f}} \|\mathbf{A}\mathbf{f} - \mathbf{b}\|^2 + \lambda \frac{\beta}{2} \sum_{\mathbf{q} \in \mathcal{N}} \|\mathbf{D}_{\mathbf{q}}\mathbf{f} - \mathbf{h}_{\mathbf{q}}\|^2. \quad (3.12)$$

Here, $h_{\mathbf{q}}(\mathbf{x})$ is specified by the sum of $\hat{\mathbf{s}}_{\mathbf{r},\mathbf{q}}$ terms from the adjacent patches:

$$h_{\mathbf{q}}(\mathbf{x}) = \sum_{\mathbf{p} \in \mathcal{B}} \hat{\mathbf{s}}_{\mathbf{x}-\mathbf{p},\mathbf{q}}(\mathbf{p}), \quad (3.13)$$

The operator $\mathbf{D}_{\mathbf{q}}$ in equation (3.12) is the finite difference operator

$$(\mathbf{D}_{\mathbf{q}}\mathbf{f})(\mathbf{x}) = \mathbf{f}(\mathbf{x}) - \mathbf{f}(\mathbf{x} + \mathbf{q}). \quad (3.14)$$

For example, $(\mathbf{D}_{(1,0)}\mathbf{f})(\mathbf{r}) = f(\mathbf{r}) - f(\mathbf{r} + (1, 0, 0))$ is the standard horizontal finite difference operator. Note that by using equation (3.10) in equation (3.12), the terms with inter-patch differences greater than T will still contribute to a constant term of T^p/p in the cost. This behavior translates to patch differences above T not being shrunk at each iteration as seen from equation (3.11) (see also Fig 3.1.c) while the terms with smaller inter-patch differences are penalized. We solve equation (3.12) efficiently using conjugate gradient (CG) algorithm.

3.3 METHODS

The breath-held CINE dataset considered in this study is distributed as part of the MASTeR software package [57], while the free breathing Cartesian dataset was acquired at New York University [80]. The perfusion datasets were both acquired at the University of Utah. All the datasets used in this note were acquired under protocols approved by the Institutional Review Board (IRB) of the respective institutions.

3.3.1 Experiments Involving Cardiac CINE MRI

We first consider the retrospective undersampling of a fully sampled ECG-gated Cartesian breath-held dataset, acquired using a steady-state free precession (SSFP) sequence using a five channel cardiac array. The scan parameters were TE/TR= 2.0/4.1 ms, flip angle=45°, FOV=350 mm², slice thickness=12 mm, 8 views per segment, 224 phase-encoding lines, 256 read-out samples and 16 temporal frames. This dataset was undersampled by keeping a subset of the 224 phase-encoding lines consisting of a fully sampled low-frequency region (eight low-frequency lines) and a pseudo-randomly sampled high-frequency region chosen according to a Gaussian density; the specific pseudo random subsets varied from frame to frame.

In the second experiment, we consider the recovery of a prospectively undersampled free-breathing and prospectively ECG-gated cardiac CINE dataset. The data was acquired using a steady state free precession (SSFP) sequence on Siemens 3T scanner with 12 coil elements total (body and spine coil arrays). The acquisition parameters were FOV: 320 mm², matrix 128×128, TE/TR = 1.37/2.7 ms, BW: 1184 Hz/pixel, and flip angle = 40°.

The acquisition lasted for two heart beats, while the subject was freely breathing, resulting in 16 lines/frame. The sampling pattern varies from frame to frame; some of the frames are sampled with dense low-frequency region, while the lines in other frames are sampled randomly in the low and high-frequency region. See [80] for more details about this dataset.

3.3.2 Experiments Involving Myocardial Perfusion Imaging

In the first experiment involving perfusion data, we retrospectively undersampled a fully-sampled Cartesian *in-vivo* myocardial perfusion dataset. The dataset was acquired without ECG-gating and the subject breathed heavily during the scan. The data was acquired using a saturation recovery FLASH sequence (with TR/TE =2.5/1 ms, saturation recovery time = 100 ms, 1 slices, 32 coil elements total, phase encodes x frequency encodes: 108×288 , temporal resolution: ≈ 4 frames/beat, spatial resolution: $2.5 \times 2.5 \times 8$ mm³); the reader is referred to [34, 81] for more details about this dataset. The dataset was retrospectively undersampled using a Cartesian sampling pattern with a fully sampled low-frequency region and a randomly sampled high-frequency region. To make the computational complexity manageable, we have only considered 80 temporal frames out of 200. We only used the data corresponding to six of the 32 channels, which best cover the heart; we did not resort to any coil compression.

In the second perfusion experiment, we consider the retrospective undersampling of radially sampled free-breathing stress ECG-gated myocardial perfusion data, acquired with a saturation recovery FLASH sequence with TR/TE =2.6/1.2 ms, phase encodes x frequency encodes: 256×256 , 3 slices/beat, flip angle=14°, voxel size = $2.3 \times 2.3 \times 8$ mm³, FOV: 280 mm², bandwidth 1002 Hz/pixel. This dataset has 67 temporal frames which are all considered for recovery. Seventy two radial spokes per frame, equally spaced over π radians with 256 samples per spoke were acquired. The radial pattern in successive frames were rotated by a uniform angle of $\pi/288$ radians across frames, which corresponds to a period of 4 across time. The details of this dataset are available at [82]. We subsampled the dataset by retaining a subset of 24 spokes per frame. To obtain incoherent sampling, the spokes that are the closest in angles to a golden angle trajectory were retained; a similar

subsampling strategy was used in [44]. The 72 spoke data, acquired with a four coil cardiac array, was reconstructed using SENSE-based spatiotemporal TV regularization; simpler gridding based reconstructions exhibited considerable streaking artifacts and were found unacceptable for comparisons.

For all the radial acquisitions considered in this aim, we first gridded the radial data to a Cartesian grid to avoid the use of non-uniform Fourier transform computations within the reconstruction algorithms. Our previous experiments [44] show that the loss in image quality resulting from this approximation is minimal.

3.3.3 Implementation Details

All the algorithms were implemented in MATLAB 2012 on a Linux Intel Xeon workstation machine with four cores, 3.2 GHz CPU, and 32 GB RAM.

Metrics used for quantitative comparison: The retrospective reconstructions were quantitatively compared to reference data using the following metrics. We evaluate these metrics in a square region of interest containing the heart.

- Signal to Error Ratio (SER): This metric gives a measure of overall accuracy in reproducing the spatiotemporal dynamics in the heart regions and defined as:

$$\mathbf{SER} = 20 \log_{10} \left(\frac{\|\mathbf{\Gamma}_{\mathbf{orig}}\|_2}{\|\mathbf{\Gamma}_{\mathbf{orig}} - \mathbf{\Gamma}_{\mathbf{rec}}\|_2} \right),$$

where $\|\cdot\|_2$ donates the ℓ_2 norm, and $\mathbf{\Gamma}_{\mathbf{orig}}$, $\mathbf{\Gamma}_{\mathbf{rec}}$ denote the original and the reconstructed images respectively.

- Normalized High Frequency Error (HFEN): It measures the quality of fine features, edges, and spatial blurring in the images and defined as:

$$\mathbf{HFEN} = 20 \log_{10} \left(\frac{\|\text{LoG}(\mathbf{\Gamma}_{\mathbf{orig}})\|_2}{\|\text{LoG}(\mathbf{\Gamma}_{\mathbf{orig}}) - \text{LoG}(\mathbf{\Gamma}_{\mathbf{rec}})\|_2} \right),$$

where LoG is a Laplacian of Gaussian filter that capture edges. We use the same filter specifications as [61]: kernel size of 15×15 pixels, with a standard deviation of

1.5.

- The Structural SIMilarity index (SSIM): We used the toolbox introduced by [83], with default contrast values [0.01 0.03], Gaussian kernel size of 11×11 pixels with a standard deviation of 1.5 pixels to compare the reconstructions.

3.3.4 Selection of Parameters

To ensure fair comparisons in retrospective undersampling experiments, all algorithms were run with a range of parameter values, and the parameter set that resulted in the best SER was chosen. In the prospective experiment involving free breathing cardiac CINE data, the parameters of all the methods were tuned manually to get the best performance. Considering that we compare algorithms of very different flavors on datasets acquired at different conditions, we believe that this is a reasonable strategy to ensure fair comparisons. We used the reconstruction of the total variation regularization as an initial guess for the DC-CS scheme [55].

We set the neighborhood and patch sizes in PRICE to $5 \times 5 \times 5$ and $3 \times 3 \times 1$ ($N=2$; $M=4$), respectively for all the experiments. Our experiments (not shown here) shows that these settings were sufficient to capture the inter-frame motion in all the applications considered in this research; larger neighborhood sizes did not significantly improve the performance, while they resulted in slower reconstructions. The continuation parameter β was initialized by 0.01 and was incremented by a factor of 1.5 in each outer iteration. Similarly, T was set to be about a half of the image maximum intensity value and divided by a small fraction in each outer iteration. Our experiments show that $p = 0.5$ in equation (3.6) gave the best tradeoff between computational complexity and quality of the reconstructions. We used 5 inner-iterations and 20 outer-iterations for all the experiments considered in this research. These continuation strategies minimized the risk of convergence to local minimum and also provided fast convergence; see [2] for more details. The algorithm is terminated when the relative change in cost falls below small value ε ; we have set ε as $1e-6$ in our scheme.

3.4 RESULTS

3.4.1 Results of Cardiac CINE Datasets

The reconstruction of the retrospectively undersampled cardiac CINE dataset using PRICE, spatiotemporal total variation based algorithm (TV), k-t SLR [44], and the state-of-the-art ME-MC methods [55, 57] are shown in Fig 3.2, along with their error images. The Cartesian sampling pattern corresponding to an undersampling factor of 6, was used to subsample the datasets. Two frames corresponding to peak diastole and systole cardiac phases are shown for each scheme; the error images are scaled by a factor of 7 for better visualization. We observe that the quality of the PRICE reconstructions is quite comparable to the DC-CS recovery, which explicitly compensates for the motion; the error images show that the errors associated with PRICE and DC-CS are more homogeneously distributed in the entire image, resulting in improved SER. By contrast, the errors associated with TV and MASTeR methods are more concentrated in the edge regions, indicating edge blurring. The table shows a quantitative comparison of the entire methods using SER, HFEN and SSIM metrics; all computed on the region of interest shown in first row. The run time of PRICE, DC-CS and MASTeR were 24.4 minutes, 3.8 hours, 3.3 hours respectively. The run time for k-t SLR was 25 minutes while TV took approximately 19 minutes.

The experiments involving prospective Cartesian undersampled free breathing CINE data is shown in Fig 3.3. The comparisons show that the proposed scheme provides reconstructions with lower motion artifacts and less blurring compared to DC-CS, k - t SLR, and TV regularized reconstructions, especially near the myocardial borders and papillary muscles. The inter-frame motion in this dataset is relatively high, making it a challenging example. We found it difficult to optimize the parameters of MASTeR in the prospective experiments when the ground truth are not available and hence we have excluded them from the comparisons.

3.4.2 Results of Myocardial Perfusion MRI

The results of the retrospectively undersampled ungated and free-breathing *in-vivo* myocardial perfusion experiment are shown in Fig 3.4. We consider the recovery from three

fold undersampled Cartesian trajectory. The proposed algorithm is compared against DC-CS [55], k - t SLR, MASTeR [57], and spatiotemporal total variation regularization algorithm. Four frames corresponding to peak right ventricular blood enhancement, transition between right ventricle and left ventricle, peak left ventricular blood enhancement and the case when the enhanced blood leaves the heart are shown. The ungated acquisition enables us to acquire diastolic and systolic frames. This dataset is quite challenging due to quite significant cardiac and respiratory motion as well as contrast variations resulting from bolus passage. We observe that the PRICE scheme is able to provide reconstructions with lower spatial and temporal blurring compared to the other schemes. The quantitative metrics show about 1- 2.5 dB improvement compared to other reconstructions. Even though DC-CS results in crisp images, it exhibits pixelated interpolation artifacts in some frames due to inaccuracies during correction of the highly non-rigid cardiac motion between consecutive systole and diastole phases. Other authors have also reported similar artifacts when compensating for large motion with explicit motion compensation algorithms [54]. The run time of MATLAB CPU versions of PRICE, DC-CS and MASTeR were 18.5 minutes, 1.4 hour, 1.2 hour respectively. The run time for k-t SLR was 38 minutes while TV took approximately 24 minutes.

The experiments on the free-breathing ECG-gated radial stress perfusion MRI datasets, acquired from a normal subject and recovered from 24 rays are shown in Fig Fig 3.5. The motion in this dataset is not as challenging as in the previous case since the acquisition was ECG-gated and the subject was instructed to breath shallowly. We observe that most of the motion compensated algorithms provide good reconstructions in this case. However, PRICE is considerably more computationally efficient than those explicit ME-MC methods. It is also seen from the error images that the motion compensated methods (PRICE and DC-CS) provide reduced edge blurring and better preservation of fine features, including papillary muscles and around the myocardium wall as shown in the red arrows. The run time of PRICE and DC-CS were 20.6 minutes and 1.6 hours respectively while k-t SLR took 50 minutes and TV approximately 33 minutes.

3.5 DISCUSSION AND CONCLUSION

We introduced an iterative patch-based shrinkage algorithm to recover dynamic MRI from highly undersampled Fourier measurements. The proposed framework alternates between a patch shrinkage step and a quadratic subproblem that is solved efficiently using conjugate gradients algorithm. The proposed method utilizes the redundancy between patches in nearby frames to achieve implicit motion-compensated recovery. This makes it a computationally efficient alternative to ME-MC methods, which often require detailed motion models, reference frames, and careful initialization to minimize the convergence to local minimum. More importantly, the computational complexity of these methods are rather high. By contrast, the PRICE scheme formulates the motion-estimation and motion compensation steps into a simple cost-function, which is similar to classical total variation regularization. The comparison of PRICE against classical TV and k - t SLR schemes demonstrates the benefits of this framework in reducing motion-induced blurring and streaking artifacts. The algorithm is also seen to provide comparable or improved reconstructions over state-of-the-art ME-MC schemes, while being considerably more computationally efficient. The experiments also show that PRICE can provide improved reconstruction of perfusion MRI data, which indicates that it is not very sensitive to the contrast changes between the frames. Specifically, the robust nature of the distance function minimizes the averaging of the patches that differ considerably in contrast/intensity, thus reduces blurring in these regions. Note that the contrast changes are highly localized in space; the similarity of the patches in other regions can still be exploited effectively using the proposed PRICE algorithm. The existence of a common cost function for both motion-estimation and motion compensation steps enable efficient continuation strategies that encourage the convergence to the global minimum. The proposed scheme may be thought of as an implicit motion-compensated compressed sensing scheme with computational complexity that is comparable to classical TV methods.

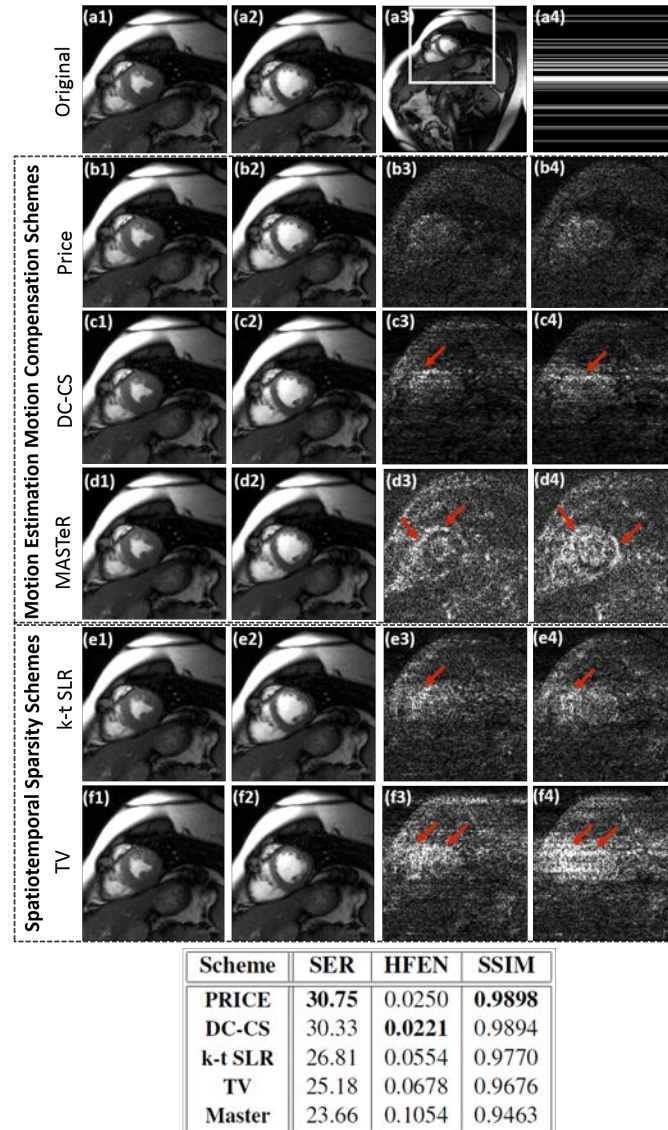


Figure 3.2: Recovery of a retrospectively undersampled CINE dataset using PRICE (second row; b1-b2), explicit motion-compensated algorithms (third and fourth rows), k-t SLR and classical total variation regularization (fifth and sixth rows). The $256 \times 224 \times 16$ dynamic dataset, which is acquired using $\times 5$ coils, is retrospectively undersampled using Cartesian sampling pattern. The cropped cardiac images of the fully sampled data corresponding to peak diastole and systole cardiac phases are shown in (a1) and (a2). These images are cropped versions of the full frame shown in (a3). The sampling pattern for one frame is shown in (a4). The cropped reconstructed images are shown in the first two columns, while their error images scaled by a factor of 7 for better visualization are shown in the last two columns. The reconstructions using the PRICE algorithm is quite comparable to the DC-CS scheme, which explicitly compensates for the motion; the error images show that the errors associated with PRICE and DC-CS are more homogeneously distributed in the entire image, resulting in improved SER. By contrast, the errors with other methods (e.g. TV and MASTeR) are more concentrated in the edge regions, indicating edge blurring. The table shows a quantitative comparison of the entire methods using SER, HFEN and SSIM metrics; all computed on the region of interest as shown in (a3).

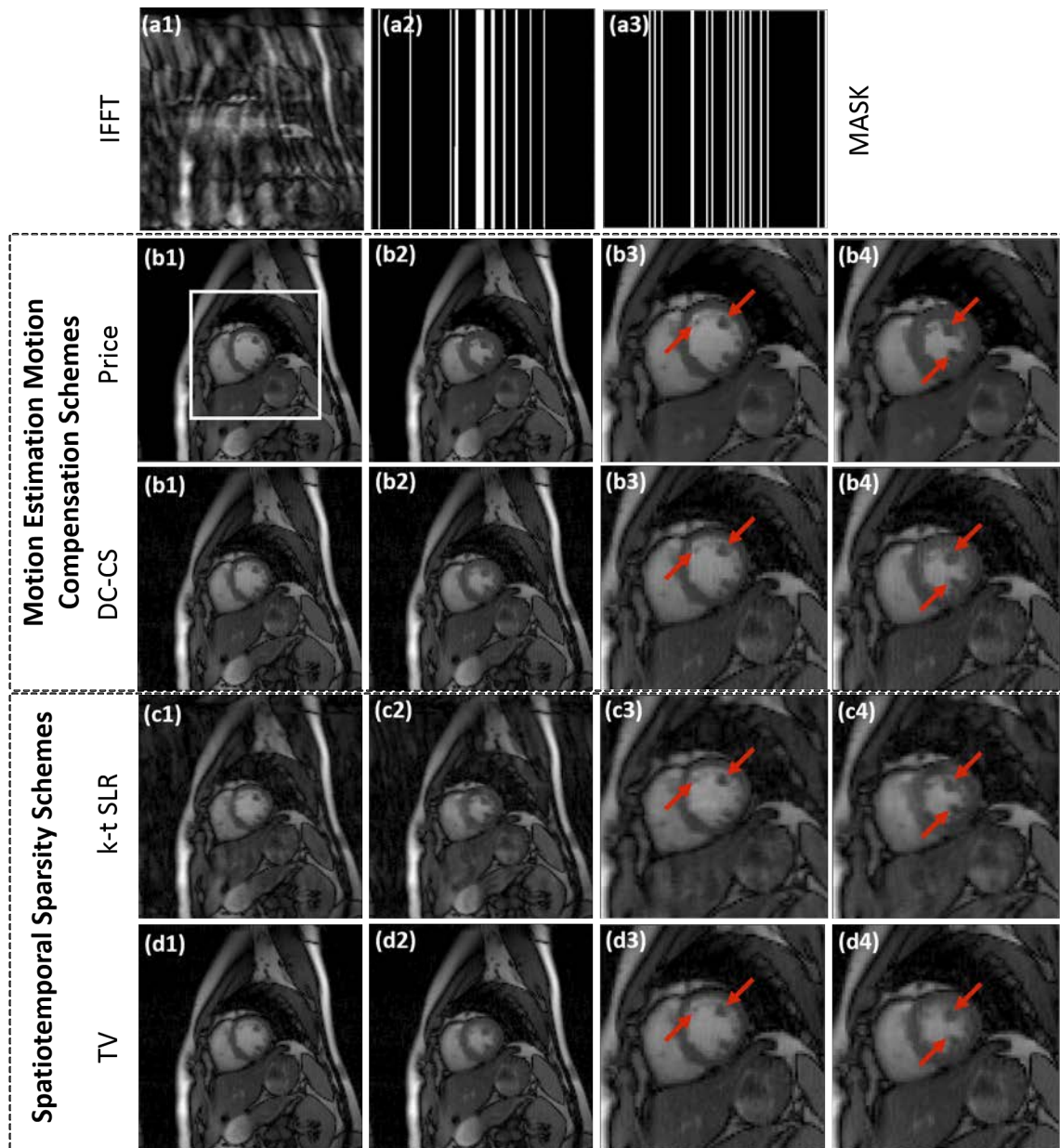


Figure 3.3: Recovery of a prospectively undersampled Cartesian CINE dataset using PRICE, DC-CS, k-t SLR and TV algorithms. The $128 \times 128 \times 20$ sized dataset is acquired using 12 coils and 16 Cartesian lines per phase. Two frames corresponding to peak diastole and systole cardiac phases are shown for each scheme along with their zoomed versions around the square box as shown in (b1). The sampling pattern varies from frame to frame; the sampling masks corresponding to two different frames are shown in (a2) and (a3). We observe that TV and k - t SLR reconstructions exhibit temporal blurring while DC-CS had some motion artifacts. PRICE is able to provide better reconstructions with less blurred myocardial borders and papillary muscles.

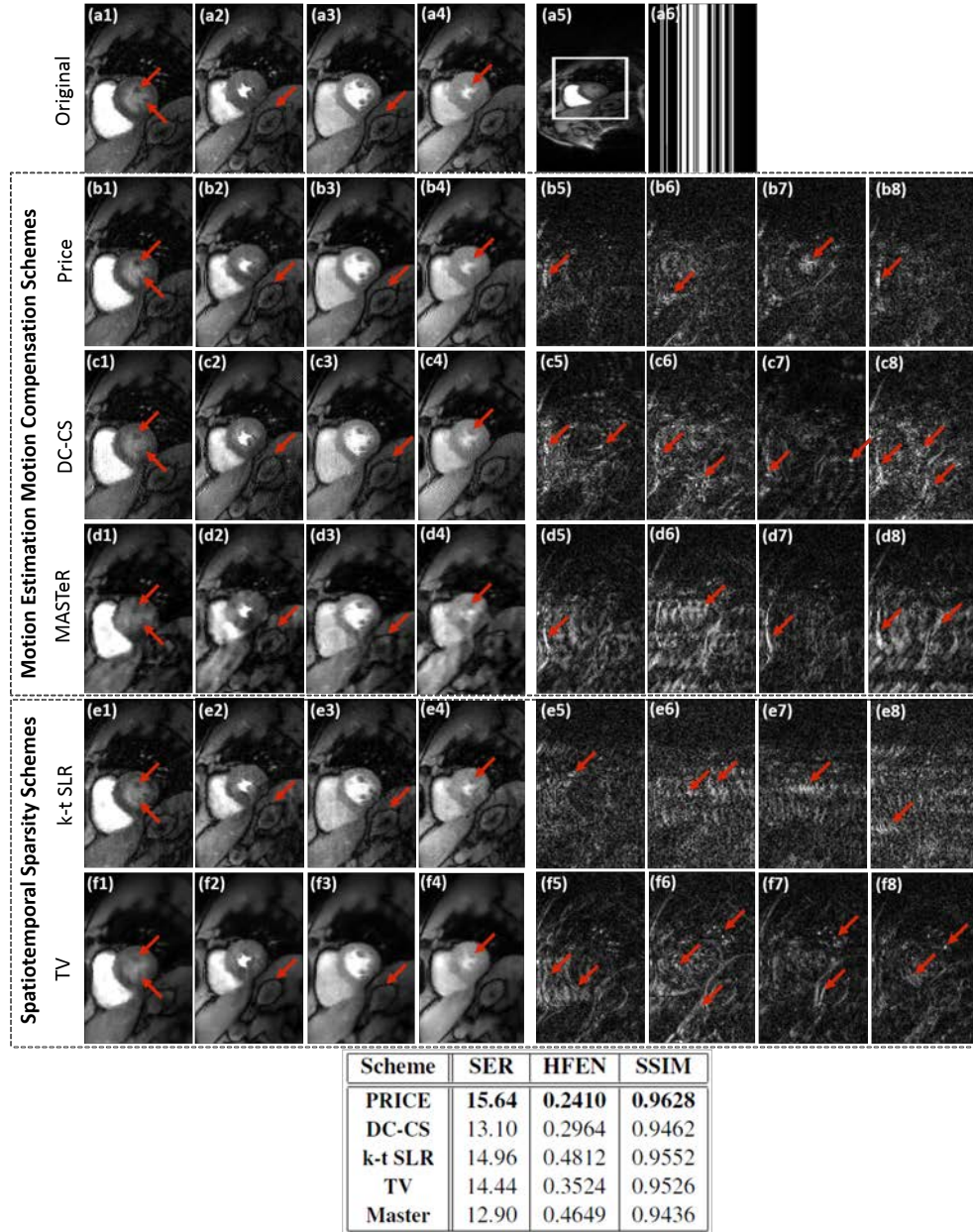


Figure 3.4: Evaluation of the ME-MC algorithms by retrospectively downsampling ungated & free-breathing myocardial perfusion MRI data. The images (a1-a4) correspond to frames in the time series with different cardiac/respiratory phases and different contrast due to bolus passage. These images are cropped from a $288 \times 108 \times 80$ dataset acquired with 6 coils; one of these images are shown in (a5). We undersampled the Cartesian sampled data along the phase encoding direction to obtain a three-fold acceleration. One of the sampling masks are shown in (a6). The reconstructions and corresponding residuals using PRICE (b1-b4) & (b5-b8), DC-CS (c1-c4) & (c5-c8), MASTeR (d1-d4) & (d5-d8), k-t SLR (e1-e4) & (e5-e8) and TV (f1-f4) & (f5-f8) are shown. The error images are scaled by a factor of three for better visualization. The extensive inter-frame motion and contrast variations due to bolus passage makes this dataset very challenging. We observe that the PRICE scheme provides reconstructions with lower spatial and temporal blurring, compared to the other algorithms. The table above shows a quantitative comparison of the entire methods using SER, HFEN and SSIM metrics computed on the region of interest shown in (a5).

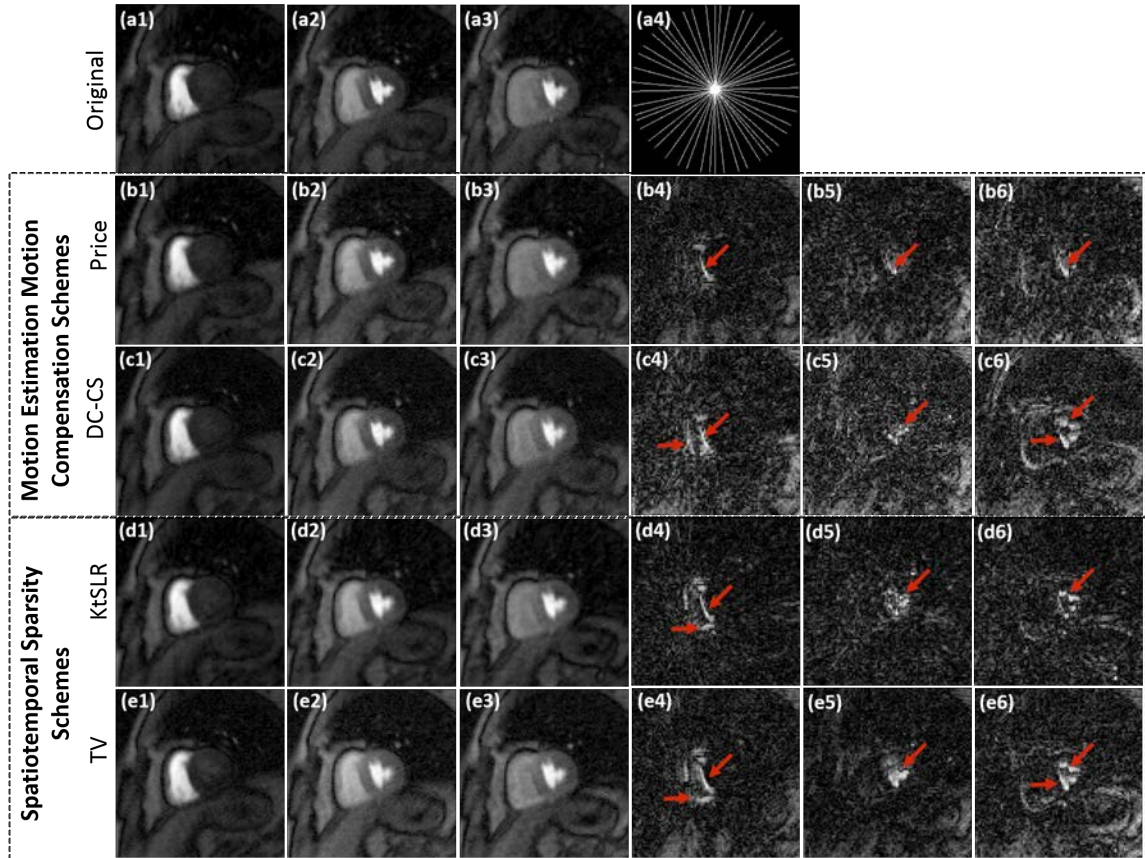


Figure 3.5: Evaluation of the ME-MC algorithms by radially downsampling $256 \times 256 \times 67$ adenosine free-breathing stress myocardial perfusion MRI data acquired from a normal subject. Three frames of the reference data acquired using 72 spokes/frame are shown in (a1-a3). This data is undersampled by retaining a subset of 24 spokes; the sampling trajectory for one of the frames is shown in (a4). The recovered images and their corresponding residual images using PRICE (b1-b3) & (b4-b6), DC-CS (c1-c3) & (c4-c6), k-t SLR (d1-d3) & (d4-d6), and TV (e1-e3) & (e4-e6) are shown. The three frames correspond to peak right ventricular blood enhancement, a transition between the right ventricle and the left ventricle and peak left ventricular blood enhancement respectively. It is seen from the error images that the motion compensated methods (PRICE and DC-CS) provide reduced edge blurring and better preservation of fine features, including papillary muscles and around the myocardium wall as shown by the red arrows.

CHAPTER 4 FREE-BREATHING & UNGATED CARDIAC MRI USING ITERATIVE STORM (I-STORM)

4.1 ABSTRACT

We introduce a local manifold regularization approach to recover dynamic MRI data from highly undersampled measurements. The proposed scheme relies on the manifold structure of local image patches at the same spatial location in a free-breathing cardiac MRI dataset; this approach is a generalization of the SToRM (SmooThness Regularization on Manifolds) scheme that exploits the global manifold structure of images in the dataset [5]. Since the manifold structure of the patches varies depending on the spatial location and is often considerably simpler than the global one, this approach significantly reduces the data demand, facilitating the recovery from shorter scans. Since the navigator-based estimation of manifold structure pursued in SToRM is not feasible in this setting, a reformulation of SToRM is introduced. Specifically, the regularization term of the cost function involves the sum of robust distances between images sub-patches in the dataset. The optimization algorithm alternates between updating the images and estimating the manifold structure of the image patches. The utility of the proposed scheme is demonstrated in the context of *in-vivo* prospective free-breathing cardiac CINE MRI imaging with multichannel acquisitions as well as simulated phantoms. The new framework facilitates a reduction in scan time, as compared to the SToRM strategy.

4.2 METHOD

4.2.1 SToRM reconstruction

The SToRM recovery of the dynamic MRI dataset \mathbf{F} from its undersampled Fourier measurements \mathbf{B} is posed as [5]:

$$\mathbf{F}^* = \arg \min_{\mathbf{F}} \|\mathcal{A}(\mathbf{F}) - \mathbf{B}\|_2^2 + \lambda \sum_{i=1}^N \sum_{j=1}^N w_{i,j} \|\mathbf{f}_i - \mathbf{f}_j\|^2 \quad (4.1)$$

where \mathbf{f}_i is the i^{th} frame in the dynamic dataset, and hence is the i^{th} column of the Casorati matrix \mathbf{F} and N is the total number of frames in the time series. A navigated acquisition

strategy was used to estimate the matrix \mathbf{W} with entries $w_{i,j}$, which captures the manifold structure. The measurement operator at the i^{th} frame is chosen as:

$$\mathbf{b}_i = \underbrace{\begin{bmatrix} \Phi \\ \mathbf{B}_i \end{bmatrix}}_{\mathbf{A}_i} \mathbf{f}_i \quad (4.2)$$

Here, \mathbf{A}_i is multichannel sampling operator for the i^{th} frame. It is the concatenation of the navigator sampling operator Φ , which is fixed across all frames, and \mathbf{B}_i which varies from frame to frame. The structure of the manifold specified by the weights $w_{i,j}$, are estimated from navigators as below:

$$w_{i,j} = \exp - \frac{\|\Phi \mathbf{x}_i - \Phi \mathbf{x}_j\|^2}{\sigma^2} \quad (4.3)$$

It was shown that equation (4.1) can also be expressed as:

$$\mathbf{F}^* = \arg \min_{\mathbf{F}} \|\mathcal{A}(\mathbf{F}) - \mathbf{B}\|_2^2 + \lambda \text{trace}(\mathbf{F}\mathbf{L}\mathbf{F}^H), \quad (4.4)$$

where:

$$\mathbf{L} = \mathbf{D} - \mathbf{W} \quad (4.5)$$

and \mathbf{D} is a diagonal matrix with entries $d_{i,i} = \sum_j \mathbf{w}_{i,j}$. \mathbf{L} is often termed as the graph Laplacian operator, which can be viewed as the discrete approximation of the Laplace Beltrami operator on the manifold. The trace of a square matrix is defined as the sum of the elements on the main diagonal, and \mathbf{F}^H denotes the conjugate transpose of \mathbf{F} .

4.2.2 Calibration-free i-SToRM

We formulate the reconstruction of the images from their highly undersampled measurements as the following unconstrained optimization problem:

$$\mathbf{F}^* = \arg \min_{\mathbf{F}} \|\mathcal{A}(\mathbf{F}) - \mathbf{B}\|_2^2 + \lambda \underbrace{\sum_{i=1}^N \sum_{j=1}^N \varphi(\|\mathbf{f}_i - \mathbf{f}_j\|)}_{\mathcal{C}} \quad (4.6)$$

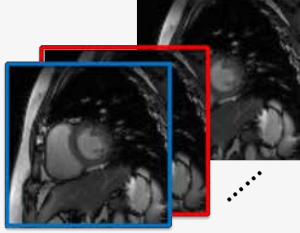
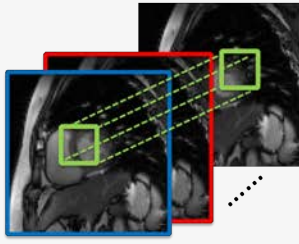
| | |
|--|--|
| $\mathbf{F}^* = \arg \min_{\mathbf{F}} \ \mathcal{A}(\mathbf{F}) - \mathbf{B}\ _2^2 +$ $\lambda \sum_{i=1}^{N_f} \sum_{j=1}^{N_f} w_{i,j} \ \mathbf{f}_i - \mathbf{f}_j\ ^2$  <p style="text-align: center;">(a) SToRM</p> | $\mathbf{F}^* = \arg \min_{\mathbf{F}} \ \mathcal{A}(\mathbf{F}) - \mathbf{B}\ _2^2 +$ $\lambda \sum_{\mathbf{r}_k} \sum_{i=1}^{N_f} \sum_{j=1}^{N_f} \varphi(\ \mathcal{P}_{\mathbf{r}_k}(\mathbf{f}_i - \mathbf{f}_j)\)$  <p style="text-align: center;">(b) i-SToRM</p> |
|--|--|

Figure 4.1: Illustration of the proposed i-SToRM scheme (b), in comparison with the SToRM scheme in (a). The regularization term in SToRM involves the sum of weighted ℓ_2 distances between images in the dataset, where the weights are estimated from navigators. By contrast, the regularization scheme in i-SToRM is the sum of unweighted robust distances between image sub-patches in the dataset. Specifically, the patches of size $N \times N$ indicated by the green neighborhood are compared with each other using the distance metric, which saturates with large distances. The center of the patches, specified by \mathbf{r}_k are chosen to span the entire image with a specified stride; the patches are overlapping in space to reduce blocky artifacts in the image and suppress noise. The main difference between these formulations is the distance metric. We use an alternating minimization to solve for the i-SToRM scheme, which alternates between the estimation of the manifold Laplacian and the images; this approach eliminates the need for the use of navigators and allows the extension of the SToRM scheme to exploit the manifold structure of local patches. When the size of the patches is the same as the size of the images, the first iteration of the i-SToRM scheme is equivalent to the SToRM setting.

The regularization penalty \mathcal{C} involves the sum of unweighted robust distances between images in the dataset. This is in contrast to equation (4.1) that uses weighted quadratic distances between frames, which requires the knowledge of the manifold or equivalently the weights $w_{i,j}$. We choose the regularization prior φ as a saturating distance metric that penalizes small distances heavily, while it saturates with large distances. In this work, we use the H_1 metric [84], specified by:

$$\varphi(t) = 1 - \exp(-t^2/2\sigma^2) \quad (4.7)$$

The Taylor series expansion of $\varphi(t)$ shows that $\varphi(t) \approx \frac{t^2}{\sigma^2} + \mathcal{O}(t^4)$, which implies that φ can be safely assumed to be a quadratic/Euclidean distance metric for small values of t . Note that the geodesic distances (distances on the manifold) between neighboring points on the manifold can be safely approximated by their Euclidean distances. By contrast, Euclidean distances between points that are distant on the manifold are not good approximations for the geodesic distance. The use of the saturating prior eliminates such terms from the cost function. In particular, pairs of frames that have a large inter-frame Euclidean distance do not contribute to the gradient of the cost function, even though they amount to constant terms in the regularization prior. The proposed scheme exploits the non-local redundancy between frames that may be well separated in time. In particular, equation (4.6) facilitates the implicit sharing of data between similar frames. This implicit approach can be seen as an alternative to explicitly binning the dynamic data from different respiratory and cardiac phases, followed by the recovery of the bins [67]. Since the regularization term is non-convex, we use homotopy continuation strategies to encourage the convergence of the algorithm to the global minimum. While this approach is not guaranteed to converge to a global minimum, it is widely used in non-convex compressive sensing and usually results in good solutions [85].

4.2.3 Relationship to STORM

Inspired by [84], we use a majorize minimize algorithm to solve equation (4.6). This majorization strategy has been introduced in [18] and has been widely used in convex and non-convex image recovery with iterative reweighted algorithms. The non-convex prior (second term in equation (4.6)) can be majorized as the sum of quadratic distances between images in the dynamic dataset:

$$\varphi(\|\mathbf{f}_i - \mathbf{f}_j\|) \leq w_{i,j} \|\mathbf{f}_i - \mathbf{f}_j\|^2 \quad (4.8)$$

where the new interframe weights are specified by $w_{i,j} = \psi(\|\mathbf{f}_i - \mathbf{f}_j\|)$. Here,

$$\psi(t) = \begin{cases} \exp\left(-\frac{t^2}{2\sigma^2}\right) & \text{if } t^2 < T \\ 0 & \text{else.} \end{cases} \quad (4.9)$$

Note that the function $\psi(0) = 1$, while it decays with increasing value of t . The use of the majorization in equation (4.8) ensures that similar images are averaged together, while dissimilar images are excluded from the averaging process. This majorization provides a two-step approach, which alternates between the estimation of the weights from the current images using equation (4.9) and solving for the images using equation (4.6). Thus, this approach can be viewed as an iterative version of STORM, where the weights are estimated from the current image iterate rather than the k-space navigators as in equation (4.3).

While more efficient optimization strategies such as alternating direction method of multipliers do exist, the use of these methods along with non-convex priors may suffer from local minima issues. By contrast, the monotonic convergence offered by the majorize minimize framework, along with efficient continuation strategies, can be combined to encourage the convergence of the algorithm to the global minimum of equation (4.6).

4.2.4 i-STORM with patches

The formulation in equation (4.6) facilitates the exploitation of the manifold structure of images in the dataset without explicit navigators. We note that different spatial regions in the dataset will experience different types of motion. For example, the cardiac regions are expected to experience cardiac and respiratory motion, while the lung regions far away from the heart are expected to be independent of cardiac motion. To exploit the spatial variation in manifold structure, we generalize equation (4.6) to account for the manifold structure of image sub-patches. Specifically, we formulate the recovery as:

$$\mathbf{F}^* = \arg \min_{\mathbf{F}} \|\mathcal{A}(\mathbf{F}) - \mathbf{B}\|_2^2 + \lambda \underbrace{\sum_{\mathbf{r}_k} \sum_{i=1}^{N_f} \sum_{j=1}^{N_f} \varphi(\|\mathcal{P}_{\mathbf{r}_k}(\mathbf{f}_i - \mathbf{f}_j)\|)}_{\mathcal{C}_{\mathbf{r}_k}} \quad (4.10)$$

Here, $\mathcal{P}_{\mathbf{r}}(\mathbf{f})$ is a patch extraction operator, which extracts a square shaped 2-D image patch centered at the spatial location \mathbf{r} from the dynamic dataset \mathbf{f} :

$$\mathcal{P}_{\mathbf{r}}(\mathbf{f}) = f(\mathbf{r} + \mathbf{p}), \mathbf{p} \in \mathcal{K} \quad (4.11)$$

Here, \mathcal{K} denotes the square shape neighborhood of size of dimension $(N + 1) \times (N + 1)$, centered at \mathbf{r} . The set of spatial locations \mathbf{r}_k , or equivalently the patches, are chosen to span the entire image. For example, the set can be chosen as a set of overlapping or non-overlapping patches. Note that the penalty term $\mathcal{C}(\mathbf{r}_k)$ is essentially the same as the penalty term \mathcal{C} in equation (4.6), restricted the smaller set of images $\mathcal{P}_{\mathbf{r}}(f_i); i = 1, \dots, N$. See Figure 4.1, where the comparisons are restricted to a cube, centered at the spatial location \mathbf{r}_k . The motion parameters within different spatial regions/cubes are expected to be very different in cardiac MRI. This restriction results in a considerably simpler manifold in regions with no motion or regions with only respiratory motion, which is essentially most of the field of view (FOV). Thus, the generalization is expected to be a more adaptive version of STORM. Note that equation (4.6) is a special case of equation (4.10), when the size of the patch is the same size of each image, and only one \mathbf{r}_k is considered. We observe that the STORM approach of calibration-based estimation of the manifold structure is not feasible in the patch-based setting. Specifically, k-space navigators only provide global information about the whole FOV, which can only be used to estimate the image manifold structure. The localized manifold structure estimation is facilitated by the reformulation of equation (4.6).

4.2.5 Two step iterative algorithm using MM

We use the majorize minimize (MM) framework to solve for equation (4.10). The non-convex patch-based prior (second term in equation (4.10)) can be majorized as the sum of quadratic distances between image sub-patches in the dynamic dataset:

$$\varphi(\|\mathcal{P}_{\mathbf{r}_k}(\mathbf{f}_i - \mathbf{f}_j)\|) \leq w_{i,j,\mathbf{r}_k} \|\mathcal{P}_{\mathbf{r}_k}(\mathbf{f}_i - \mathbf{f}_j)\|^2 \quad (4.12)$$

where the new interframe weights can be self-estimated from the undersampled dataset, as opposed to the navigators used in SToRM.

Using the majorization in equation (4.10), we obtain an alternating minimization strategy, which alternates between updating the images and the weights/Laplacian operators.

Image update: Once the weights are available, the image can be estimated as:

$$\mathbf{F}^* = \arg \min_{\mathbf{F}} \|\mathcal{A}(\mathbf{F}) - \mathbf{B}\|_2^2 + \lambda \sum_{\mathbf{r}_k} \text{trace}(\mathbf{F}_k \mathbf{L}_k \mathbf{F}_k^H) \quad (4.13)$$

where \mathbf{F}_k is the Casorati matrix:

$$\mathbf{F}_k = \left[\mathcal{P}_{\mathbf{r}_k}(f_1), \dots, \mathcal{P}_{\mathbf{r}_k}(f_{N_f}) \right] \quad (4.14)$$

of the patch time series $\mathcal{P}_{\mathbf{r}_k}(f_i), i = 1, \dots, N_f$. We can think of $\mathbf{F}_k = \mathcal{Q}_k(\mathbf{F})$, where \mathcal{Q}_k is an operator that extracts the cube of data centered at the spatial location \mathbf{r}_k and constructs a Casorati matrix out of it. The matrices $\mathbf{L}_k = \mathbf{D}_k - \mathbf{W}_k$ are the Laplacians of the patch time series \mathbf{F}_k . We observe that equation (4.13) is the extension of equation (4.4) to the patch setting.

The Euler-Lagrange equation for the above quadratic equation is given by:

$$\mathcal{A}^* \mathcal{A}(\mathbf{F}) + 2 \lambda \sum_{\mathbf{r}_k} \mathcal{Q}_k^* \left(\underbrace{\mathcal{Q}_k(\mathbf{F})}_{\mathbf{F}_k} \mathbf{L}_k \right) = \mathcal{A}^* \mathbf{B} \quad (4.15)$$

Here, \mathcal{A}^* denotes the adjoint of the operator \mathcal{A} . The second term on the l.h.s involves the extraction of the Casorati matrix \mathbf{F} , multiplication by \mathbf{L}_k , followed by putting the entries of the Casorati matrix back at the appropriate location. The optimization problem equation (4.15) can be efficiently solved using conjugate gradients.

Weight update: The Laplacian matrices, or equivalently the weights, are estimated from the current image series \mathbf{F} as:

$$(\mathbf{W}_k)_{i,j} = \psi(\|\mathcal{P}_{\mathbf{r}_k}(\mathbf{f}_i - \mathbf{f}_j)\|) \quad (4.16)$$

where ψ is specified by equation (4.9). Note that the inter-patch distance metric in equation (4.7) was chosen to heavily penalize small differences between the patches, while the metric saturates for large sub-patch differences. The patch operator extracts a cube of data in the temporal direction and constructs a Casorati matrix, equation equation (4.14). The saturating distance metric ensures that the penalty for highly dissimilar patch pairs are considerably smaller than what it would be if ℓ_1 or ℓ_2 priors are used. In STORM, the neighborhood of each frame was set to be a fixed number of nearest neighbors, the elements of \mathbf{W} in equation (4.5), where the weights are estimated from spatially fixed navigators. Unlike STORM, where the weight matrix was sparsified to retain only 3 nearest neighbors for each frame, the weight matrix in the new framework, is thresholded in order to prevents over-smoothing of the recovered images. Note that this approach is consistent with the assumed metric equation (4.7).

Algorithm 4.2.1: i-STORM(\mathcal{A}, \mathbf{B})

Input : $\mathbf{B} =$ k-space measurements
 $\mathbf{F}_{\text{init}} = \mathbf{B};$
while $i < \#$ Outer Iterations
 do $\left\{ \begin{array}{l} \text{Update } \mathbf{F} \text{ by solving equation (4.15) using CG;} \\ \text{Update weight matrices } \mathbf{W}_k \text{ using equation (4.16);} \\ \text{Derive the Laplacians } \mathbf{L}_k \text{ from } \mathbf{W}_k \text{ using equation (4.5);} \end{array} \right.$
return (\mathbf{F})

4.2.6 Datasets and sampling pattern

We validate the new algorithm using a human phantom, used to simulate free-breathing cardiac imaging experiments with variable heartbeat periods [86]. The data has been created by realistically image warping a breath held cine dataset, not necessarily having regular breathing patterns. It has a reasonable amount of inter-frame motion due to respiratory dynamics and its a good fit to apply quantitative metrics and compare the proposed scheme with state-of-the-art methods. The dataset has 200 phase encodings, 256 samples per readout and 256 temporal frames.

We also validate the proposed algorithm using experiments on two *in-vivo* free-breathing and ungated cardiac CINE datasets with radial undersampling settings. They were acquired using protocols approved by the Institutional Review Board (IRB) at the University of Iowa. The prospectively undersampled MR imaging was acquired using radial FLASH sequence on a Siemens Skyra 3T scanner with 24 coil elements total (body and spine coil arrays). The datasets were acquired from congenital heart patients, who were instructed to breathe freely in all of the studies. The images were acquired in short axis and 4-chamber view to test the sensitivity of the algorithm to geometry. The short axis data was acquired using the calibration-based scheme in [5] as well as a golden angle acquisition scheme. By using the equiangular spacing within each frame, we ensure that the entire k-space is covered uniformly.

The sequence parameters were: TR/TE 4.68/2.1 ms, FOV 300mm, base resolution 256, slice thickness = 5 mm, phase encodes \times frequency encodes: 512×512 . A temporal resolution of 46.8 ms was achieved by sampling 10 lines of k-space per frame. 1000 radial lines of k-space were acquired per slice which resulted in an acquisition time of around 46.8 s. The scan parameters were kept the same across all views for the entire prospective datasets.

4.2.7 Metrics used for quantitative comparison

The retrospective reconstructions were quantitatively compared to the reference data using SER, HFEN and SSIM metrics, described in the earlier chapter. We also use Global Phase Coherence, GPC, for both retrospective and prospective experiments. We evaluated these metrics in both the entire images and a square region of interest containing the heart.

GPC index is used to measure image sharpness by defining the Fourier phase spectrum of an image and estimating the volume of all possible phase functions associated with the measured modulus. The likelihood is measured with the total variation (Rudin-Osher-Fatemi implicit prior), and the numerical estimation is realized by a Monte-Carlo simulation:

$$\mathbf{GPC}(\mathbf{u}) = -\log_{10} \Phi \left(\frac{\mu - \mathbf{TV}(u)}{\sigma} \right), \quad (4.17)$$

where μ and σ are the mean and variance of the samples $(\mathbf{TV}(u_i))_{1 \leq i \leq N}$, N is the total number of images and Φ is the tail of the Normal Distribution, that is $\Phi(x) = (2\pi)^{-(1/2)} \int_x^{+\infty} e^{-t^2/2} dt$. GPC index decreases with blur, noise, and ringing, and thus provides a new interesting sharpness indicator, that can be used for parametric blind deconvolution and prospective studies when ground truth is not available. We used the toolbox introduced by Blanchet et al [87].

4.2.8 Implementation

The algorithms were implemented using a single node of a high-performance Argon Cluster at the University of Iowa, equipped with Intel Xeon CPU with 28 Cores at 2.40GHz with 128 GB of memory running on Red Hat Linux MATLAB R2016b.

The prospective datasets were acquired using 10,000 radial spokes, which corresponded to an acquisition time of around 50 seconds per slice. We binned the data to 10 spokes/frame, which translates to 1000 frames. Our earlier SToRM scheme needed 1000 frames to obtain good reconstructions. By contrast, we only rely on the first 300 time frames in this work. The raw k-space of the radially acquired datasets are interpolated into a Cartesian grid before processing to avoid the use of non-uniform Fourier transform computations within the reconstruction algorithms. Our previous experiments [44] show that the loss in image quality resulting from this approximation is minimal. We reconstructed low temporal resolution images for the original coils by binning k-space data from a large number of frames. Since more than half of the coil images were contaminated with noise, we threw away the noisy ones and we kept the best 10 coils. The data from the selected coils was coil-combined using SVD to form 5-6 virtual coils with most significant singular vectors. The coil sensitivity maps were estimated from this compressed data using the method designed by Walsh et al [88] and assumed to be constant over time. Not only excluding the noisy coils helped get better results for the entire schemes, but also reduced the computational complexity of the reconstruction procedure and made the memory demand of the SENSE-based method manageable.

Since the prospective datasets used in this work have no ground truth available, the

quantitative metrics, except for GPC, can't be used for these experiments. To allow for a systematic comparison, one standardized way of choosing the model parameters is to rely on the data consistency term. Since all of these methods share a quadratic data fit term $\|\mathcal{A}(\mathbf{F}) - \mathbf{B}\|_2^2$, the model regularization parameter for each method was chosen so that the different methods produce matching data fit terms (to within a small tolerance). In i-SToRM experiments, the optimal parameters determined for one dataset work well for other datasets acquired in the same setting. The filter size parameter σ was initialized by 10^{-4} and was decreased by a factor of 10^{-1} in each outer iteration. This continuation strategy helped provide fast convergence and minimize the oversmoothing resulted from averaging multiple neighbors. Our results show that 3-4 iterations are sufficient to get the best recovery. Adding more iterations did not further improve the weight matrix, and hence the reconstruction. We set the patch sizes in the proposed scheme to 12×12 with a step size of 4 to ensure the patches are overlapped for better recovery. Smaller neighborhood and step sizes did not significantly improve the performance, while they resulted in slower reconstructions. Our experiments show that the above choice provided the best tradeoff between the computational complexity and the quality of reconstructions. The algorithm is terminated when the relative change in the cost function falls below small value ϵ ; we have set ϵ to 10^{-6} in our scheme. The thresholding parameter T in (4.9) and regularization factor λ in both (4.6,4.10) were set to 10^{-2} and 10^{-6} respectively. We have kept the default value of PSF subspace dimension to 32.

4.3 RESULTS

We compare our results with prior SToRM and low-rank based partially separable functions, PSF, method [86]. PSF exploits the linear dependencies between the intensity profiles by modeling them as a linear combination of basis functions, which are estimated from navigator signals. For the PSF method, we use the Frobenius norm of the basis images as a regularizer, which is similar to [86]. We also compare the proposed scheme with compressed sensing temporal Total Variation plus Wavelet method using Berkeley Advanced Reconstruction Toolbox (BART) [89].

In Figure 4.2 we compare the proposed patch-based i-SToRM with both i-SToRM without patches and classical Total Variation with Wavelet regularization methods. The navigator spokes were not used for estimating the manifold structure in both i-SToRM schemes. The i-SToRM with patches scheme exploits the local manifold structure, while i-SToRM without patches exploits the global image manifold structure, similar to SToRM. We also compare the results against SToRM and PSF, both of which rely on navigators to estimate the manifold structure and subspace, respectively. Row 2 corresponds to the proposed scheme, which is i-SToRM with patches (b1-b3). The i-SToRM without patches is shown in row 3 (c1-c3), and TV + WV in row 4 (d1-d3). The SToRM and PSF schemes that rely on navigators are shown in rows 5-7, (e1-e3) (f1-f3) and (g1-g3). Rows 2-6 correspond to reconstructions from 300 frames (≈ 14 seconds of acquisition), while the bottom row corresponds to SToRM reconstruction from 1000 frames (≈ 50 seconds of acquisition). The images are zoomed versions around the square box shown in (a3) while (a2) is the initial guess. The time profiles in the last column are drawn for the entire reconstructed frames along the line passing through the cardiac region shown in (b1). The chosen frames are depicted in the time profiles with their respective colors. Three frames of different phases are shown for each recon case. The sampling trajectory for one of the sampling patterns is shown in (a1), with colored lines indicating the fixed navigators. We will suffice to compare the proposed patch-based i-SToRM version for the rest of the datasets. In the last column, the GPC indices computed for the entire time series are reported. The top value was calculated for the global images while the one shown in the bottom was computed around a small region of interest containing the heart. The quantitative metric shows the reconstruction of the proposed method using 300 frames are comparable to that 1000 dataset recovered using SToRM.

In Figure 4.3 we show the reconstruction from a calibration-based acquisition in rows 2-5, while row 6 corresponds to a golden angle acquisition. Rows 2 and 6 were recovered using patch-based i-SToRM. The calibrated-free dataset is recovered using the proposed scheme and TV + WV since both SToRM and PSF cannot estimate the manifold structure without navigators. The sampling trajectories for navigated and golden-angle schemes for

one of the frames are shown in (a1) and (a2). Only a subset of 300 frames was used for all the reconstructions. This example shows that the i-SToRM with patches can facilitate the recovery of the data without navigators and can shorten the scan time compared to SToRM, with less significant artifacts exhibited in PSF and TV + WV schemes. Note that the above two datasets studied in this research are quite challenging, considering the ungated setting, the high undersampling factor, as well as the large respiratory motion due to free-breathing mode. The last column shows the GPC indices for both the entire images, the top value, as well as around a small region of interest containing the myocardium shown in the bottom. The quantitative metric shows an improvement of the proposed method compared to other reconstructions. In the last column, the GPC indices computed for the entire time series are reported. The top value was calculated for the global images while the one shown in the bottom was computed around the myocardium. The quantitative metric shows an improvement of the proposed method compared to other reconstructions.

Figure 4.4 shows the recovery of the simulated CINE dataset using navigators-free schemes i-SToRM with patches and TV + Wavelet, and navigator-based schemes SToRM and PSF. The simulated dynamic dataset is retrospectively undersampled using radial sampling pattern with 12 spokes, 4 navigator lines and 8 golden angle spokes per frame. One of the sampling masks is shown in (a6) with colored lines indicating the navigators. Three frames of each recon of the data corresponding to peak diastolic and systolic cardiac phases and one in transition phase are shown for each scheme. The images are cropped versions of the full frame shown in (a5) while (a4) is the initial guess. The reconstructed images are shown in the first three columns along with their error images scaled by a factor of 5 for better visualization. The time profiles in the last column are drawn for the entire recovered frames, along with the line passing through the left ventricle and right ventricle shown in (a5). The tables at the bottom of the figure show a quantitative comparison of the entire methods using SER, HFEN, SSIM and GPC metrics computed on the entire times series on both global images as well as a square region of interest containing the heart as shown in (f1).

4.4 DISCUSSION AND CONCLUSION

We introduced a novel regularization approach to exploit the manifold structure of local image patches to recover dynamic MRI data from highly undersampled measurements. The proposed scheme is a generalization of the SToRM scheme, which exploits the global manifold structure of images in the dataset. Since the manifold structure of the patches are simpler and vary depending on the spatial location, this approach reduces the data demand, facilitating the recovery from shorter scans. Since the direct extension of SToRM to the patch setting is not possible, we relied on a regularization term that involves the sum of robust distances between images sub-patches in the dataset. We used an alternating minimization scheme that alternates between the estimation of the manifold Laplacian and the recovery of the patches; this approach generalizes SToRM and eliminates the need for navigators to estimate the Laplacian. The utility of the proposed scheme is demonstrated in the context of *in-vivo* prospective free-breathing cardiac CINE MRI imaging with multichannel acquisitions. The new framework facilitates the reduction in the scan time by a factor of three, compared to the SToRM strategy.

In Figure 4.2, we observe that the i-SToRM with patches is almost comparable in performance to SToRM, which shows that the Laplacian can be estimated without the use of explicit navigators, which also facilitates the extension of SToRM to the patch setting. The main difference of i-SToRM scheme with SToRM is the way in which the manifold Laplacian is estimated. We observe a significant reduction in alias artifacts in i-SToRM with patches, resulting from the exploitation of the local manifold structure, compared to i-SToRM without patches. We observe that the performance of both PSF and TV + Wavelet schemes is worse than the SToRM scheme, especially in terms of the temporal profile and the noise amplification. This can be explained by the improved modeling of data by the non-linear manifold model, as opposed to the subspace model used in PSF or combination of sparse TV and Wavelet. As expected the SToRM with 300 frames result in increased noise, compared to the SToRM reconstructions shown in the bottom row, where the reconstruction relied on 1000 frames (≈ 50 seconds of acquisition). By contrast, the patch-based i-SToRM shown in the second row is comparable in performance to the SToRM reconstructions with

1000 frames shown in the bottom row. Since SToRM and i-SToRM without patches rely on the similarity between images in the dataset, a large number of images are needed to ensure that all the phases are well represented. Hence, these methods require relatively long acquisition duration to ensure that the image manifold is well-sampled. By contrast, local patch manifolds are relatively simpler; fewer images (and hence shorter acquisitions) are sufficient to ensure good sampling of the corresponding patch manifolds. This translates to improved performance over TV + Wavelet and PSF. Also, we observe i-SToRM without patches results in lower quality, indicating the need for local manifold modeling, especially when the Laplacian is estimated from the images themselves. We considered the entire dataset recovery using SToRM prior in the bottom row for the sake of comparison.

The results in Figure 4.3 show the ability of the proposed i-SToRM scheme in recovering quality images comparable to SToRM without relying on navigator signals. Comparing the time profiles of the i-SToRM scheme between the navigated and non-navigated setting, we observe that the time profiles are smoother in the calibration-free dataset. This can be explained by the improved incoherence of sampling offered by the golden angle sequence. Note that the navigated sequence resulted in a 40% loss in efficiency due to the need for navigators. We can also see both TV + Wavelet and PSF exhibit considerable temporal motion artifacts or blurring. While i-SToRM is compared against SToRM and PSF using the calibration-based dataset, the calibrated-free dataset is recovered using only the proposed scheme as well as TV + Wavelet since both SToRM & PSF cannot estimate the manifold structure without navigators.

In Figure 4.4, we observe that i-SToRM provides reconstructions with lower spatial and temporal blurring, compared to other algorithms. While SToRM recon is quite comparable to the proposed scheme, PSF and TV + Wavelet reconstructions exhibit motion artifacts and temporal blurring respectively. The residual images show that the errors associated with i-SToRM and SToRM are more homogeneously distributed in the entire image, thus provide reduced edge blurring and better preservation of fine features, including papillary muscles. By contrast, the errors with TV+ Wavelet and PSF are more concentrated in the edge regions and around the myocardial wall, indicating edge blurring. The quantita-

tive comparisons of the algorithms on this setting are shown in the bottom tables where we quantified the reconstruction by the signal-to-error ratio (SER), High Frequency Error (HFEN), Structural SIMilarity index (SSIM) and Global Phase Coherence (GPC) metrics computed on the entire images as well as a square region of interest containing the heart as shown in (f1). The quantitative metrics show about 1- 4 dB SER improvement using i-SToRM compared to other reconstructions. The improvement behavior is consistent using HFEN, SSIM and GPC quantitative metrics.

Our results demonstrate that using the local manifold structure of image patches is superior to global manifold recovery. This approach is related to PRICE prior introduced in the earlier chapter 3. The main difference is the neighborhood to which each patch is compared. Specifically, PRICE compares each patch with its immediate neighbors, facilitating implicit motion compensated reconstruction. Since this comparison has to be repeated for all the patches in the 3-D dataset, the computational complexity of the extension of PRICE scheme to this setting is challenging; it had been previously demonstrated on breath-held CINE and myocardial perfusion MRI applications, where the undersampling factor was considerably lower, when recovery from fewer image frames was sufficient. The number of inter-patch comparisons in the proposed scheme is lower by an order of magnitude. Specifically, we only compare each patch with patches in all the frames at the same location, which keeps the computational complexity manageable. The proposed implicit motion resolved reconstruction can be viewed as an alternative to binning strategies, which exploits the repetitive respiratory and cardiac motion. The benefit of the proposed scheme is that it does not require sophisticated approaches to estimate the motion phases, and is applicable to non-periodic motion applications such as speech and imaging of the digestive tract, where phase information is difficult to obtain; see [5] for examples of an application of SToRM framework to speech imaging.

The utility of the proposed scheme is demonstrated in the context of simulated human phantoms as well as prospective free-breathing and ungated cardiac CINE MRI imaging with multichannel acquisitions. Future efforts will be directed towards an extension of the proposed scheme to a 3D multi-slice multi-channel acquisition.

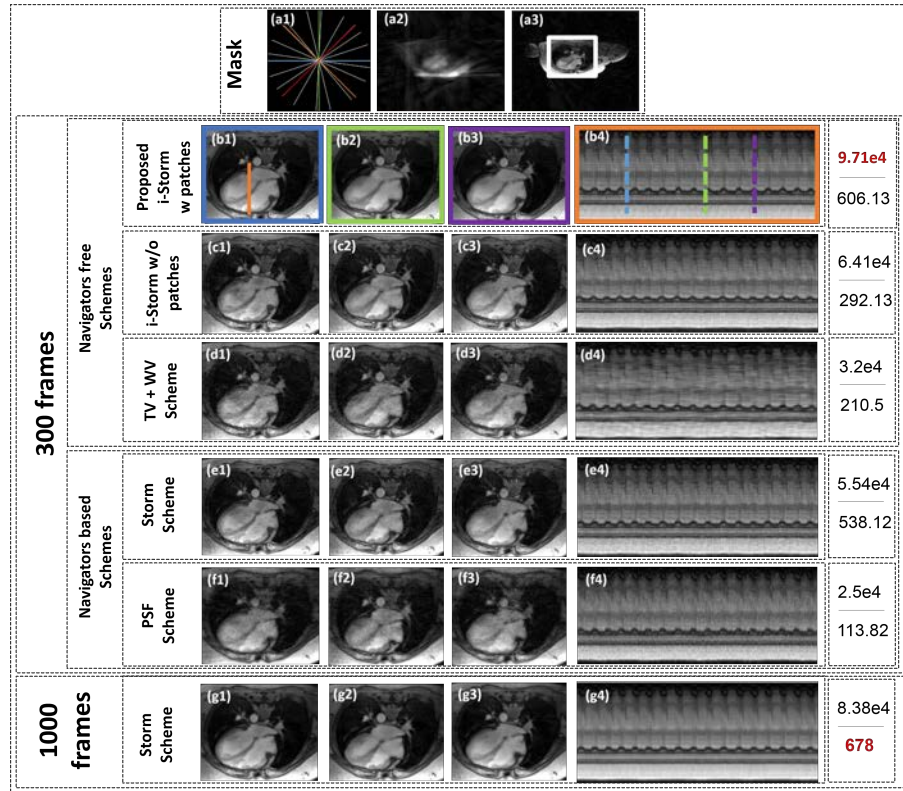


Figure 4.2: Comparison of SToRM, PSF, TV +Wavelet, i-SToRM without patches, and i-SToRM with patches: We study the performance of these methods on a free-breathing ungated cardiac CINE setting, acquired in the axial 4-chamber view. The dataset was acquired using the navigated acquisition scheme used in [5], which consists of 4 navigator lines and 6 golden angle spokes per frame. The sampling trajectory for one of the sampling patterns is shown in sub-figure (a1) with colored lines indicating the navigators that are the same for all frames. The time profiles in the fourth column are drawn for all of the recovered frames, along with the line passing through the cardiac region shown in (b1). The time instance of the specific frames are depicted in the time profiles with the color of their bounding boxes. Three frames of each recon dataset are shown. The images are zoomed versions around the square box shown in (a3) while (a2) is the initial guess. Subfigures (b1-b3), (c1-c3) and (d1-d3) show the recovery using navigators-free schemes, patch-based i-SToRM, i-SToRM with patches and TV + Wavelet respectively; while (e1-e3) and (f1-f2) show the recovery using navigators-based schemes SToRM and PSF. The top five rows are recovered using only a subset of 300 frames, while the bottom row shows the data recovered from 1000 frames. SToRM and PSF schemes, shown in the 5th - 7th rows, relied on navigators to estimate the global manifold Laplacian. The comparisons of the reconstructions from 300 frames show that the i-SToRM scheme can provide comparable image quality to the SToRM scheme, even though it did not rely on the navigators. This iterative approach enabled us to exploit the local manifold structure of the patches (i-SToRM with patches), which significantly improved the performance over the global approach. The improved performance of SToRM and iSToRM over PSF and TV +Wavelet methods, seen by a reduced blurring of image features and improved temporal profiles, can be attributed to the improved signal modeling offered by the non-linear manifold model compared to a subspace approach or sparsity regularization. Note that the image quality of the i-SToRM with patches obtained from 300 frames is comparable to that obtained from SToRM with 1000 frames. In the last column, we report the GPC indices for both the entire images, the top value, as well as around a small region of interest containing the heart shown in the bottom. The quantitative metric shows that the reconstruction of the proposed method using 300 frames are comparable to that 1000 dataset recovered using SToRM.

| | | Mask | | | | | |
|---------------------------|--------------------------|----------------------------|------|------|------|------|------------------|
| | | (a1) | (a2) | (a3) | (a4) | | |
| Calibration Based Dataset | Navigators free Schemes | Proposed i-Storm w patches | (b1) | (b2) | (b3) | (b4) | 5.68e4 487.84 |
| | | TV + WV Scheme | (c1) | (c2) | (c3) | (c4) | 1.6e4 298.15 |
| | Navigators based Schemes | Storm Scheme | (d1) | (d2) | (d3) | (d4) | 3.09e4 356.36 |
| | | PSF Scheme | (e1) | (e2) | (e3) | (e4) | 1.2e4 210.58 |
| Calibration Free Dataset | Navigators free Schemes | Proposed i-Storm w patches | (f1) | (f2) | (f3) | (f4) | 5.7e4 549.24 |
| | | TV + WV Scheme | (g1) | (g2) | (g3) | (g4) | 3.2e4 399.02 |

Figure 4.3: Evaluation of the proposed i-SToRM scheme with patches on free-breathing and ungated dataset with short axis views. The dataset was collected with two acquisition schemes: a navigated acquisition scheme, as well as a golden angle sequence. The sampling trajectories for navigated and golden-angle schemes for one of the frames are shown in (a1) and (a2), respectively where the colored lines indicating the fixed navigators that are the same for all frames. 300 frames of the time series (3000 spokes, which correspond to 14 seconds of acquisition) were considered for recovery. Subfigures (b1-b3) and (c1-c3) show the recovery using navigators-free i-SToRM without patches and TV + Wavelet while (d1-d3) and (e1-e3) show the recovery using navigators-based schemes SToRM and PSF respectively. The bottom two rows show the calibration-free dataset recovered using the proposed i-SToRM method with patches (f1-f3) and TV + Wavelet (g1-g3). Note that there is no one-to-one correspondence between the two acquisitions since they were acquired at two different time points, possibly with different respiratory patterns. (a3) is the initial guess, while (a4) is the corresponding frame recovered using patch-based i-SToRM. The zoomed versions of three frames, out of 300 frames, from different phases in the dataset are shown for the entire cases. The time profiles in the fourth column are drawn for all of the frames, along the line passing through the left ventricle and right ventricle as shown in (b1). While i-SToRM is compared against SToRM and PSF using the calibration-based dataset, the calibrated-free dataset is recovered using only the proposed scheme as well as TV + Wavelet since both SToRM & PSF cannot estimate the manifold structure without navigators. The results show the ability of the proposed i-SToRM scheme in recovering quality images comparable to SToRM without relying on navigator signals. Both TV + Wavelet and PSF exhibit considerable motion artifacts and temporal blurring. The last column shows the GPC indices for both the entire images, the top value, as well as around a small region of interest containing the myocardium shown in the bottom. The quantitative metric shows an improvement of the proposed method compared to other reconstructions.

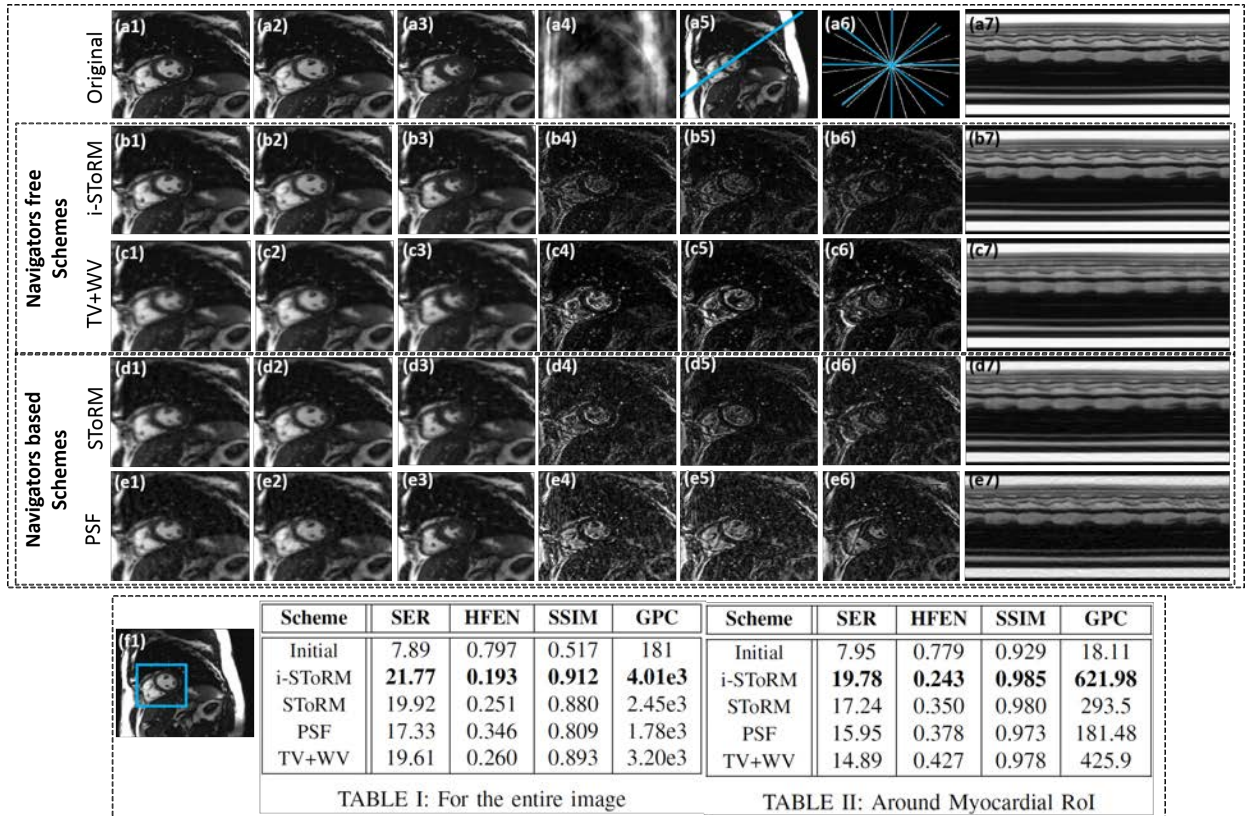


Figure 4.4: Recovery of the simulated CINE dataset using i-StoRM with patches (b1-b3), both calibration-based schemes SToRM (c1-c3) and PSF (d1-d3), and classical total variation with wavelet regularization (e1-e3). The simulated dynamic dataset is retrospectively undersampled using radial sampling pattern with 12 spokes, 4 navigator lines and 8 golden angle spokes per frame. One of the sampling masks is shown in (a6) with colored lines indicating the navigators. Three frames of each recon of the data corresponding to peak diastolic and systolic cardiac phases and one in transition phase are shown for each scheme. The images are cropped versions of the full frame shown in (a5) while (a4) is the initial guess. The reconstructed images are shown in the first three columns along with their error images scaled by a factor of 5 for better visualization. The time profiles in the last column are drawn for the entire recovered frames, along with the line passing through the left ventricle and right ventricle shown in (a5). We observe that i-StoRM provides reconstructions with lower spatial and temporal blurring, compared to other algorithms. While SToRM recon is quite comparable to the proposed scheme, PSF and TV + Wavelet reconstructions exhibit motion artifacts and temporal blurring respectively. The residual images show that the errors associated with i-StoRM and SToRM are more homogeneously distributed in the entire image, thus provide reduced edge blurring and better preservation of fine features, including papillary muscles. By contrast, the errors with TV + Wavelet and PSF are more concentrated in the edge regions and around the myocardial wall, indicating edge blurring. The tables at the bottom of the figure show a quantitative comparison of the entire methods using SER, HFEN, SSIM and GPC metrics computed for the entire times series on both global images as well as a square region of interest containing the heart as shown in (f1).

CHAPTER 5 SUMMARY & FUTURE DIRECTIONS

5.1 SUMMARY

In this thesis, we apply iterative algorithms of patch-smoothness regularization in medical imaging applications. These approaches are enabled by the reformulation of current non-local regularization schemes as an alternating algorithm to minimize a global criterion. We divide our research into three main chapters.

In Chapter 2, we developed a fast and novel iterative shrinkage algorithm for patch-smoothness regularization to recover static 2D MR imaging from undersampled and noisy measurements. This approach is enabled by the reformulation of current non-local regularization schemes as an alternating algorithm to minimize a global criterion. The proposed algorithm alternates between evaluating the denoised inter-patch differences by shrinkage and computing an image that is consistent with the denoised inter-patch differences and measured data. We derived analytical shrinkage rules for several penalties that are relevant to non-local regularization. The resulting algorithm is observed to be considerably faster than current alternating non-local algorithms. The proposed scheme is applicable to a large class of inverse problems including deblurring, denoising, and Fourier inversion. The comparisons of the proposed scheme with state-of-the-art regularization schemes in the context of recovering images from undersampled Fourier measurements demonstrate a considerable reduction in alias artifacts and preservation of edges.

In Chapter 3, we introduced an efficient patch smoothness regularization, we term it PRICE, which is a generalized version of the above 2D algorithm. PRICE, which implicitly compensates for interframe motion, is designed to recover dynamic MRI data from highly undersampled measurements. The regularization prior is a sum of distances between each rectangular patch in the dataset with other patches in the dataset using a saturating distance metric. Unlike current motion estimation and motion compensation (ME-MC) methods, the proposed scheme does not require reference frames or complex motion models. The proposed algorithm, which alternates between inter-patch shrinkage step and conjugate gradient algorithm, is considerably more computationally efficient than ME-MC counter-

parts. The reconstructions obtained using the proposed algorithm is compared against state-of-the-art methods applied to CINE and contrast changing perfusion datasets.

In Chapter 4, we introduced an implicit motion resolved reconstruction algorithm for real-time dynamic imaging, which didn't require specially designed sequences with navigators. We posed the image reconstruction as a regularized optimization problem, where the regularization term involves the sum of robust distances between image sub-patches in the dataset. Specifically, we used saturating distance functions that are insensitive to large image differences. A key benefit of this scheme is its ability to work with the golden angle and tiny golden angle radial sequences that are currently implemented on several scanners. The elimination of the navigators would translate to improved temporal resolution or improved image quality in practical applications.

5.2 FUTURE DIRECTIONS

Even though our research focused on cardiac and myocardial perfusion imaging, the proposed PRICE and iSTORM frameworks can be readily applied to a range of dynamic imaging problems (e.g imaging of vocal tract, liver imaging), where phase information is difficult to obtain. We will apply the designed schemes into those MR applications.

Our future endeavors will also be directed towards proposing a self-learning framework that can simultaneously estimate the manifold structure of the dynamic dataset and the signals contained on the manifold from highly under-sampled measurements. As mentioned in the previous chapters, PRICE and i-SToRM priors are quite complementary and can be combined for improved performance. Since PRICE is not suited for a large-scale dataset, our next research will be focused on even speeding up the performance of both frameworks by optimizing the schemes or using factorization for i-Storm. By combining PRICE and i-SToRM, the formulation of the motion compensation/resolution recovery as a single cost function will enable us to come up with an effective optimization algorithm that is more computationally efficient than current state-of-the-art methods. While the patch regularization term compensates for the motion, the motion-resolved term picks the respiratory phases that match each other, which are close on the manifold but may not be that close

on the real sequence. The redundancies between adjacent frames in the presence of motion can be exploited using patch smoothness regularization; while the redundancies between frames in the same cardiac and respiratory phases can be exploited using image manifold smoothness regularization, thus both provide implicit motion-compensated and implicit motion-resolved recovery.

We believe that using motion-compensated and motion-resolved blending will lower the spatiotemporal artifacts and thus provide a better and more accurate motion detection and image recovery. A combination of motion-compensated and motion-resolved priors have not been studied so far to the best of our knowledge. These implicit strategies with well-defined energy minimization formulations are more effective and computationally efficient than explicit motion compensation and other gating methods. The proposed manifold prior can extend the gains of motion-resolved and motion-compensated recovery to free-breathing applications with contrast variations, in addition to enabling the exploitation of redundancy between acquisitions with different contrasts. We will validate the proposed framework on free-breathing cardiac CINE imaging and myocardial perfusion datasets. This framework can also be easily extended to include other sequences (e.g. T2 mapping, stress perfusion), as well as non-cardiac applications (vocal tract imaging, liver imaging, and lung imaging). We will try to demonstrate the utility of the proposed schemes in the context of spiral acquired data in addition to the current golden angle radial sequences.

REFERENCES

- [1] Saiprasad Ravishankar and Yoram Bresler, “MR image reconstruction from highly undersampled k-space data by dictionary learning,” *Medical Imaging, IEEE Transactions on*, vol. 30, no. 5, pp. 1028–1041, 2011.
- [2] Yasir Mohsin, Gregory Ongie, and Mathews Jacob, “Iterative shrinkage algorithm for patch-smoothness regularized medical image recovery,” *IEEE Trans Med Imag*, DOI 10.1109, 2015.
- [3] R. Chartrand, “Exact reconstruction of sparse signals via nonconvex minimization,” *Signal Processing Letters, IEEE*, vol. 14, no. 10, pp. 707–710, 2007.
- [4] Zhili Yang and Mathews Jacob, “Nonlocal regularization of inverse problems: a unified variational framework,” *IEEE Transactions on Image Processing*, vol. 22, no. 8, pp. 3192–3203, 2013.
- [5] Sunrita Poddar and Mathews Jacob, “Dynamic mri using smoothness regularization on manifolds (storm),” *IEEE Trans Med Imag*, vol. 35, no. 4, pp. 1106–1115, 2016.
- [6] Michael Elad and Michal Aharon, “Image denoising via sparse and redundant representations over learned dictionaries,” *IEEE Transactions on Image processing*, vol. 15, no. 12, pp. 3736–3745, 2006.
- [7] Julien Mairal, Michael Elad, and Guillermo Sapiro, “Sparse representation for color image restoration,” *IEEE Transactions on image processing*, vol. 17, no. 1, pp. 53–69, 2008.
- [8] Matan Protter and Michael Elad, “Image sequence denoising via sparse and redundant representations,” *IEEE Trans Image Proc*, vol. 18, no. 1, pp. 27–35, 2009.
- [9] A. Buades, B. Coll, and J.M. Morel, “Denoising image sequences does not require motion estimation,” in *Advanced Video and Signal Based Surveillance, 2005. AVSS 2005. IEEE Conference on*. IEEE, 2006, pp. 70–74.
- [10] S.P. Awate and R.T. Whitaker, “Unsupervised, information-theoretic, adaptive image filtering for image restoration,” *IEEE Trans. Pattern Recognition*, vol. 28, pp. 364, 2006.
- [11] A. Buades, B. Coll, and J.M. Morel, “A review of image denoising algorithms, with a new one,” *Multiscale Modeling and Simulation*, vol. 4, no. 2, pp. 490–530, 2006.
- [12] L.D. Cohen, S. Bougleux, and G. Peyré, “Non-local regularization of inverse problems,” in *European Conference on Computer Vision (ECCV’08)*, 2008.

- [13] G. Gilboa, J. Darbon, S. Osher, and T. Chan, “Nonlocal convex functionals for image regularization,” *UCLA CAM Report*, pp. 06–57, 2006.
- [14] Y. Lou, X. Zhang, S. Osher, and A. Bertozzi, “Image recovery via nonlocal operators,” *Journal of Scientific Computing*, vol. 42, no. 2, pp. 185–197, 2010.
- [15] Gabriel Peyré, Sébastien Bougleux, and Laurent Cohen, “Non-local regularization of inverse problems,” in *Computer Vision–ECCV 2008*, pp. 57–68. Springer, 2008.
- [16] Z Yang and M Jacob, “A unified energy minimization framework for nonlocal regularization,” in *IEEE ISBI*, 2011.
- [17] Guobao Wang and Jinyi Qi, “Penalized likelihood pet image reconstruction using patch-based edge-preserving regularization,” *Medical Imaging, IEEE Transactions on*, vol. 31, no. 12, pp. 2194–2204, 2012.
- [18] D Geman and Chengda Yang, “Nonlinear image recovery with half-quadratic regularization,” *IEEE Transactions on Image Processing*, vol. 4, no. 7, pp. 932–946, 1995.
- [19] Pierre Charbonnier, Laure Blanc-Féraud, Gilles Aubert, and Michel Barlaud, “Deterministic edge-preserving regularization in computed imaging,” *Image Processing, IEEE Transactions on*, vol. 6, no. 2, pp. 298–311, 1997.
- [20] Alexander H Delaney and Yoram Bresler, “Globally convergent edge-preserving regularized reconstruction: an application to limited-angle tomography,” *Image Processing, IEEE Transactions on*, vol. 7, no. 2, pp. 204–221, 1998.
- [21] Mila Nikolova and Michael Ng, “Fast image reconstruction algorithms combining half-quadratic regularization and preconditioning,” in *Image Processing, 2001. Proceedings. 2001 International Conference on*. IEEE, 2001, vol. 1, pp. 277–280.
- [22] Dankmar Böhning and Bruce G Lindsay, “Monotonicity of quadratic-approximation algorithms,” *Annals of the Institute of Statistical Mathematics*, vol. 40, no. 4, pp. 641–663, 1988.
- [23] Hakan Erdogan and Jeffrey A Fessler, “Ordered subsets algorithms for transmission tomography,” *Physics in medicine and biology*, vol. 44, no. 11, pp. 2835, 1999.
- [24] Hakan Erdogan and Jeffrey A Fessler, “Monotonic algorithms for transmission tomography,” in *Biomedical Imaging, 2002. 5th IEEE EMBS International Summer School on*. IEEE, 2002, pp. 14–pp.
- [25] Peter J Huber, *Robust statistics*, Springer, 2011.

- [26] Leslie Ying and Zhi-Pei Liang, "Parallel mri using phased array coils," *Signal Processing Magazine, IEEE*, vol. 27, no. 4, pp. 90–98, 2010.
- [27] Mehmet Akçakaya, Seunghoon Nam, Peng Hu, Mehdi H Moghari, Long H Ngo, Vahid Tarokh, Warren J Manning, and Reza Nezafat, "Compressed sensing with wavelet domain dependencies for coronary mri: a retrospective study," *Medical Imaging, IEEE Transactions on*, vol. 30, no. 5, pp. 1090–1099, 2011.
- [28] Mehmet Akçakaya, Tamer A Basha, Beth Goddu, Lois A Goepfert, Kraig V Kissinger, Vahid Tarokh, Warren J Manning, and Reza Nezafat, "Low-dimensional-structure self-learning and thresholding: Regularization beyond compressed sensing for mri reconstruction," *Magnetic Resonance in Medicine*, vol. 66, no. 3, pp. 756–767, 2011.
- [29] Robert Marc Lebel, Jesse Jones, Jean-Christophe Ferre, Meng Law, and Krishna S Nayak, "Highly accelerated dynamic contrast enhanced imaging," *Magn Res Med*, vol. 71, no. 2, pp. 635–644, 2014.
- [30] Tao Zhang, Joseph Y Cheng, Aaron G Potnick, Richard A Barth, Marcus T Alley, Martin Uecker, Michael Lustig, John M Pauly, and Shreyas S Vasanawala, "Fast pediatric 3d free-breathing abdominal dynamic contrast enhanced mri with high spatiotemporal resolution," *J Magn Reson*, vol. 41, no. 2, pp. 460–473, 2015.
- [31] Li Feng, Monvadi B Srichai, Ruth P Lim, Alexis Harrison, Wilson King, Ganesh Adluru, Edward VR Dibella, Daniel K Sodickson, Ricardo Otazo, and Daniel Kim, "Highly accelerated real-time cardiac cine MRI using kt SPARSE-SENSE," *Magn Res Med*, vol. 70, no. 1, pp. 64–74, 2013.
- [32] Manish Motwani, Neil Maredia, Timothy A Fairbairn, Sebastian Kozerke, Aleksandra Radjenovic, John P Greenwood, and Sven Plein, "High-resolution versus standard-resolution cardiovascular MR myocardial perfusion imaging for the detection of coronary artery disease," *J Cardiovasc Magn Reson*, vol. 5, no. 3, pp. 306–313, 2012.
- [33] Ganesh Adluru, Chris McGann, Peter Speier, Eugene G Kholmovski, Akram Shaaban, and Edward VR DiBella, "Acquisition and reconstruction of undersampled radial data for myocardial perfusion magnetic resonance imaging," *J Magn Reson*, vol. 29, no. 2, pp. 466–473, 2009.
- [34] Devavrat Likhite, Ganesh Adluru, Nan Hu, Chris McGann, and Edward DiBella, "Quantification of myocardial perfusion with self-gated cardiovascular magnetic resonance," *J Cardiovasc Magn Reson*, vol. 17, no. 1, pp. 14, 2015.
- [35] Maojing Fu, Bo Zhao, Christopher Carignan, Ryan K Shosted, Jamie L Perry, David P Kuehn, Zhi-Pei Liang, and Bradley P Sutton, "High-resolution dynamic speech imaging with joint low-rank and sparsity constraints," *Magn Res Med*, vol. 73, no. 5, pp. 1820–1832, 2015.

- [36] Martin Uecker, Shuo Zhang, Dirk Voit, Alexander Karaus, Klaus-Dietmar Merboldt, and Jens Frahm, “Real-time MRI at a resolution of 20 ms,” *NMR in Biomedicine*, vol. 23, no. 8, pp. 986–994, 2010.
- [37] Hong Jung, Kyunghyun Sung, Krishna S Nayak, Eung Yeop Kim, and Jong Chul Ye, “k-t FOCUSS: A general compressed sensing framework for high resolution dynamic MRI,” *Magn Res Med*, vol. 61, no. 1, pp. 103–116, 2009.
- [38] Sajan Goud Lingala and Mathews Jacob, “Blind compressive sensing dynamic MRI,” *IEEE Trans Med Imag*, vol. 32, no. 6, pp. 1132, 2013.
- [39] Jose Caballero, Anthony N Price, Daniel Rueckert, and Joseph V Hajnal, “Dictionary learning and time sparsity for dynamic MR data reconstruction,” *IEEE Trans Med Imag*, vol. 33, no. 4, pp. 979–994, 2014.
- [40] Yanhua Wang and Leslie Ying, “Compressed sensing dynamic cardiac cine MRI using learned spatiotemporal dictionary,” *IEEE Trans Biomed Eng*, vol. 61, no. 4, pp. 1109–1120, 2014.
- [41] Zhi-Pei Liang, “Spatiotemporal imaging with partially separable functions,” in *IEEE I S Biomed Imaging: From Nano to Macro, Washington DC, USA*, 2007, pp. 988–991.
- [42] Henrik Pedersen, Sebastian Kozerke, Steffen Ringgaard, Kay Nehrke, and Won Yong Kim, “k-t PCA: Temporally constrained k-t BLAST reconstruction using principal component analysis,” *Magn Res Med*, vol. 62, no. 3, pp. 706–716, 2009.
- [43] Justin P Haldar and Zhi-Pei Liang, “Spatiotemporal imaging with partially separable functions: a matrix recovery approach,” in *IEEE I S Biomed Imaging: From Nano to Macro, Rotterdam, Netherlands*, 2010, pp. 716–719.
- [44] Sajan Goud Lingala, Yue Hu, Edward DiBella, and Mathews Jacob, “Accelerated dynamic MRI exploiting sparsity and low-rank structure: kt SLR,” *IEEE Trans Med Imag*, vol. 30, no. 5, pp. 1042–1054, 2011.
- [45] Viton Vitanis, Robert Manka, Daniel Giese, Henrik Pedersen, Sven Plein, Peter Boesiger, and Sebastian Kozerke, “High resolution three-dimensional cardiac perfusion imaging using compartment-based k-t principal component analysis,” *Magn Res Med*, vol. 65, no. 2, pp. 575–587, 2011.
- [46] Joshua D Trzasko, “Exploiting local low-rank structure in higher-dimensional MRI applications,” *International Society for Optics and Photonics*, pp. 885821–885821, 2013.

- [47] Joshua D Trzasko and Armando Manduca, “System and method for medical image reconstruction and image series denoising using local low rank promotion,” 2015, US Patent 8,989,465. 2015.
- [48] Anthony G Christodoulou, Haosen Zhang, Bo Zhao, T Kevin Hitchens, Chien Ho, and Zhi-Pei Liang, “High-resolution cardiovascular MRI by integrating parallel imaging with low-rank and sparse modeling,” *IEEE Trans Biomed Eng*, vol. 60, no. 11, pp. 3083–3092, 2013.
- [49] Bo Zhao, Justin P Haldar, Anthony G Christodoulou, and Zhi-Pei Liang, “Image reconstruction from highly undersampled-space data with joint partial separability and sparsity constraints,” *IEEE Trans Med Imag*, vol. 31, no. 9, pp. 1809–1820, 2012.
- [50] Hong Jung and Jong Chul Ye, “Motion estimated and compensated compressed sensing dynamic magnetic resonance imaging: What we can learn from video compression techniques,” *Int J Imag Syst Tech*, vol. 20, no. 2, pp. 81–98, 2010.
- [51] Xiao Chen, Michael Salerno, Yang Yang, and Frederick H Epstein, “Motion-compensated compressed sensing for dynamic contrast-enhanced MRI using regional spatiotemporal sparsity and region tracking: Block low-rank sparsity with motion-guidance (BLOSM),” *Magn Res Med*, vol. 72, no. 4, pp. 1028–1038, 2014.
- [52] Huisu Yoon, K Kim, Daniel Kim, Yoram Bresler, and J Ye, “Motion adaptive patch-based low-rank approach for compressed sensing cardiac cine mri,” *IEEE Transactions on Medical Imaging*, *in press*, 2014.
- [53] Muhammad Usman, David Atkinson, Freddy Odille, Christoph Kolbitsch, Ghislain Vaillant, Tobias Schaeffter, Philip G Batchelor, and Claudia Prieto, “Motion corrected compressed sensing for free-breathing dynamic cardiac MRI,” *Magn Res Med*, vol. 70, no. 2, pp. 504–516, 2013.
- [54] Javier Royuela-del Val, Lucilio Cordero-Grande, Federico Simmross-Wattenberg, Marcos Martin-Fernandez, and Carlos Alberola-Lopez, “Nonrigid groupwise registration for motion estimation and compensation in compressed sensing reconstruction of breath-hold cardiac cine MRI,” *Magn Res Med*, 2015, in process.
- [55] SG Lingala, E DiBella, and M Jacob, “Deformation corrected compressed sensing (DC-CS): A novel framework for accelerated dynamic MRI,” *IEEE Trans Med Imag*, vol. 34, no. 1, pp. 72–85, 2015.
- [56] Sajan G Lingala, Mariappan Nadar, Christophe Ched’Hotel, Li Zhang, and Mathews Jacob, “Unified reconstruction and motion estimation in cardiac perfusion MRI,” *IEEE I S Biomed Imaging: From Nano to Macro, Chicago, Illinois, USA*, pp. 65–68, 2011.

- [57] M Salman Asif, Lei Hamilton, Marijn Brummer, and Justin Romberg, “Motion-adaptive spatio-temporal regularization for accelerated dynamic mri,” *Magnetic Resonance in Medicine*, vol. 70, no. 3, pp. 800–812, 2013.
- [58] Christopher Gilliam and Thierry Blu, “Local all-pass filters for optical flow estimation,” *Proc. IEEE Int. Conf. Acoust Speech Signal Process. (ICASSP), Brisbane, Australia*, pp. 1533–1537, 5p.
- [59] Thomas Brox, Andrés Bruhn, Nils Papenberg, and Joachim Weickert, “High accuracy optical flow estimation based on a theory for warping,” *Computer Vision-ECCV*, pp. 25–36, 2004.
- [60] Zhili Yang and Mathews Jacob, “Robust non-local regularization framework for motion compensated dynamic imaging without explicit motion estimation,” *9th IEEE I S Biomed Imaging, Barcelona, Spain*, pp. 1056–1059, 2012.
- [61] Saiprasad Ravishankar and Yoram Bresler, “MR image reconstruction from highly undersampled k-space data by dictionary learning,” *IEEE Trans Med Imag*, vol. 30, no. 5, pp. 1028–1041, 2011.
- [62] Mitchell A Cooper, Thanh D Nguyen, Bo Xu, Martin R Prince, Michael Elad, Yi Wang, and Pascal Spincemaille, “Patch based reconstruction of undersampled data (PROUD) for high signal-to-noise ratio and high frame rate contrast enhanced liver imaging,” *Magn Res Med*, vol. 74, no. 6, pp. 1587–1597, 2015.
- [63] Ganesh Adluru, Liyong Chen, and Edward VR DiBella, “Undersampled free breathing cardiac perfusion mri reconstruction without motion estimation,” in *IEEE I S Biomed Imaging: From Nano to Macro, Chicago, Illinois, USA*, 2011, pp. 97–100.
- [64] Simone Coppo, Davide Piccini, Gabriele Bonanno, Jérôme Chaptinel, Gabriella Vincenti, Hélène Feliciano, Ruud B Van Heeswijk, Juerg Schwitter, and Matthias Stuber, “Free-running 4d whole-heart self-navigated golden angle mri: Initial results,” *Magn Res Med*, vol. 74, no. 5, pp. 1306–1316, 2015.
- [65] Muhammad Usman, David Atkinson, Christoph Kolbitsch, Tobias Schaeffter, and Claudia Prieto, “Manifold learning based ecg-free free-breathing cardiac cine mri,” *J Magn Reson*, vol. 41, no. 6, pp. 1521–1527, 2015.
- [66] Sajan Goud Lingala and Mathews Jacob, “Blind compressed sensing with sparse dictionaries for accelerated dynamic MRI,” pp. 5–8, 2013.
- [67] Li Feng, Leon Axel, Hersh Chandarana, Kai Tobias Block, Daniel K Sodickson, and Ricardo Otazo, “Xd-grasp: Golden-angle radial mri with reconstruction of extra motion-state dimensions using compressed sensing,” *Magn Res Med*, vol. 75, no. 2, pp. 775–788, 2016.

- [68] U. Nakarmi, Y. Wang, J. Lyu, D. Liang, and L. Ying, “A kernel-based low-rank (klr) model for low-dimensional manifold recovery in highly accelerated dynamic mri,” *IEEE Transactions on Medical Imaging*, vol. PP, no. 99, pp. 1–1, 2017.
- [69] Stanley Osher, Andrés Solé, and Luminita Vese, “Image decomposition and restoration using total variation minimization and the H^{-1} norm,” *Multiscale Modeling & Simulation*, vol. 1, no. 3, pp. 349–370, 2003.
- [70] Mila Nikolova and Michael Ng, “Analysis of half-quadratic minimization methods for signal and image recovery,” in *Journal on Scientific Computing*. SIAM, 2005, pp. 937–966.
- [71] Adrian S Lewis, “The convex analysis of unitarily invariant matrix functions,” *Journal of Convex Analysis*, vol. 2, no. 1, pp. 173–183, 1995.
- [72] Yilun Wang, Junfeng Yang, Wotao Yin, and Yin Zhang, “A new alternating minimization algorithm for total variation image reconstruction,” *SIAM Journal on Imaging Sciences*, vol. 1, no. 3, pp. 248–272, 2008.
- [73] Laurent Condat, “A simple trick to speed up and improve the non-local means,” Tech. Rep. 00512801, HAL, 2010.
- [74] M. Lustig, D. Donoho, and J.M. Pauly, “Sparse MRI: The application of compressed sensing for rapid mr imaging,” *Magnetic Resonance in Medicine*, vol. 58, no. 6, pp. 1182–1195, 2007.
- [75] Zhili Yang and Mathews Jacob, “Mean square optimal nufft approximation for efficient non-cartesian mri reconstruction,” *Journal of Magnetic Resonance*, vol. 242, pp. 126–135, 2014.
- [76] Mathews Jacob, “Optimized least-square nonuniform fast fourier transform,” *Signal Processing, IEEE Transactions on*, vol. 57, no. 6, pp. 2165–2177, 2009.
- [77] G. Peyré, S. Bougleux, and L.D. Cohen, “Non-local regularization of inverse problems,” *Inverse Problems and Imaging*, pp. 511–530, 2011.
- [78] Yifei Lou, Xiaoqun Zhang, Stanley Osher, and Andrea Bertozzi, “Image recovery via nonlocal operators,” *Journal of Scientific Computing*, vol. 42, no. 2, pp. 185–197, 2010.
- [79] D. Geman and G. Reynolds, “Constrained restoration and the recovery of discontinuities,” *Pattern Analysis, IEEE Transactions*, vol. 14, no. 3, pp. 367–383, 1992.

- [80] Li Feng, Ricardo Otazo, M Srichai, P Lim, Daniel K Sodickson, and Daniel Kim, “Highly-accelerated real-time cine MRI using compressed sensing and parallel imaging,” in *Proc. of the 14th Annual Meeting of ISMRM, Stockholm, Sweden*, p. 3602, 2010.
- [81] Alexis Harrison, Ganesh Adluru, Kavitha Damal, Akram M Shaaban, Brent Wilson, Daniel Kim, Chris McGann, Nassir F Marrouche, and EV DiBella, “Rapid ungated myocardial perfusion cardiovascular magnetic resonance: preliminary diagnostic accuracy,” *J Cardiovasc Magn Reson*, vol. 15, no. 1, pp. 26, 2013.
- [82] Edward VR DiBella, Jacob U Fluckiger, Liyong Chen, Tae Ho Kim, Nathan A Pack, Brian Matthews, Ganesh Adluru, Tiffany Priester, Suman Kuppahally, Ronny Jiji, et al., “The effect of obesity on regadenoson-induced myocardial hyperemia: a quantitative magnetic resonance imaging study,” *Int J Cardiovasc Imag*, vol. 28, no. 6, pp. 1435–1444, 2012.
- [83] Zhou Wang, Alan Conrad Bovik, Hamid Rahim Sheikh, and Eero P Simoncelli, “Image quality assessment: from error visibility to structural similarity,” *IEEE Trans Image Process*, vol. 13, no. 4, pp. 600–612, 2004.
- [84] Zhili Yang and Mathews Jacob, “Nonlocal regularization of inverse problems: a unified variational framework,” *IEEE Trans Image Process*, vol. 22, no. 8, pp. 3192–3203, 2013.
- [85] Joshua Trzasko and Armando Manduca, “Highly undersampled magnetic resonance image reconstruction via homotopic-minimization,” *Medical imaging, IEEE Transactions on*, vol. 28, no. 1, pp. 106–121, 2009.
- [86] Bo Zhao, Justin P Haldar, and Zhi-Pei Liang, “Psf model-based reconstruction with sparsity constraint: Algorithm and application to real-time cardiac mri,” in *Engineering in Medicine and Biology Society (EMBC), 2010 Annual International Conference of the IEEE*. IEEE, 2010, pp. 3390–3393.
- [87] G. Blanchet, L. Moisan, and B. Rougé, “Measuring the global phase coherence of an image,” in *Proc. Int. Conf. on Image Processing*, 2008, pp. 1176–1179.
- [88] David O Walsh, Arthur F Gmitro, and Michael W Marcellin, “Adaptive reconstruction of phased array MR imagery,” *Magn Reson Med*, vol. 43, no. 5, pp. 682–690, 2000.
- [89] Martin Uecker, Frank Ong, Jonathan I Tamir, Dara Bahri, Patrick Virtue, Joseph Y Cheng, Tao Zhang, and Michael Lustig, “Berkeley advanced reconstruction toolbox,” in *Proc. Intl. Soc. Mag. Reson. Med*, 2015, vol. 23, p. 2486.